Ultrafast, high repetition rate, high-power Yb-doped fiber laser systems

DISSERTATION

Zur Erlangung des Doktorgrades
an der Fakultät für Mathematik, Informatik und Naturwissenschaften
Fachbereich Physik
der Universität Hamburg

vorgelegt von

Sedigheh Malekmohamadi

Hamburg

2023

Gutachter der Dissertation:	Prof. Dr. Franz X. Kärtner Dr. Mikhail Pergament
Zusammensetzung der Prüfungskommission:	Prof. Dr. Franz X. Kärtner Prof. Dr. Daniela Pfannkuche Prof. Dr. Kai Roßnagel Dr. Mikhail Pergament Dr. Christoph Heyl
Vorsitzende der Prüfungskommission:	Prof. Dr. Daniela Pfannkuche
Datum der Disputation:	31.07.2023
Vorsitzender Fach-Promotionsausschusses PHYSIK:	Prof. Dr. Günter H. W. Sigl
Leiter des Fachbereichs PHYSIK:	Prof. Dr. Wolfgang J. Parak
Dekan der Fakultät MIN:	Prof. Dr.-Ing. Norbert Ritter

STATEMENT OF ORIGINAL AUTHORSHIP

Hiermit versichere ich an Eides statt, dass ich die vorliegende Dissertation selbst verfasst und keine anderen als die angegebenen Quellen und Hilfsmittel benutzt habe. | I hereby declare upon oath that I have written the present dissertation independently and have not used further resources and aids than those stated in the dissertation.

Ort, den | City, date	Unterschrift | Signature
Hamburg, 2023	Sedigheh Malekmohamadi (Anna)

Abstract

Fiber lasers were proposed shortly after the invention of the first laser [1,2] and identified as potential candidates for numerous industrial and scientific applications [3,4]. There are a number of unique features that differ fiber lasers from other laser technologies and lead to superior overall performance, such as better thermal management due to the large surface-to-volume ratio, excellent beam quality, higher wall-plug efficiencies, lower cost, and a smaller footprint compared to solid state lasers. Diode-pumped Yb-doped gain fibers with low quantum defect and broad gain bandwidth enable sub-ps pulse amplification, making them attractive for fabricating compact laser sources with a high repetition rate and high average power at 1 µm for a broad range of applications.

In this work, we demonstrate two ultrafast Yb-doped front-end laser systems with high average power and high repetition rate as seed sources for (i) High Harmonic Generation (HHG) and (ii) cryogenically cooled Yb:YLF amplifiers. Accordingly, the first part of the thesis reports on the development of a 44 fs, 68 W fiber laser at 1030 nm with a repetition rate of 1 MHz. The laser is developed based on the chirped pulse amplification (CPA) technique and consists of a nonlinear polarization evolution (NPE) mode-locked Yb-doped fiber oscillator as a seeder, a chirped fiber Bragg grating (CFBG) stretcher, a wave shaper for signal spectrum and phase manipulation, a fiber preamplifier chain, a rod-type large pitch Yb-doped fiber (YDF) amplifier, and finally two compression units. We use a wave shaper (Finisar) to manipulate the spectrum of the stretched signal to smooth out the spectral amplitude modulations and shape it into a near parabolic spectrum. The result is a pedestal-free nearly transform-limited pulse with a measured duration of 158 fs from a linear compressor. We shorten the duration of the output pulse to 44 fs, which is required for high harmonic generation (HHG), by using a multi-pass, multi-plate Herriott-type nonlinear compressor.

In the second part, we present an ultrafast fiber laser seed source at 1016 nm for Yb:YLF amplifiers. We develop a hybrid mode-locked fiber oscillator based on a nonlinear interferometer as a fast-saturable absorber in combination with a semiconductor saturable absorber mirror (SESAM) as a slow-saturable absorber in the laser cavity for reliable starting of the mode-locking. It operates in the single-pulse regime (at low pump powers) as a self-starting mode-locked oscillator with high stability and low intensity noise. Then, the output signal is spectrally broadened by self-phase modulation (SPM) in the following preamplifier made of Yb-doped aluminosilicate gain fiber. Filtering with a bandpass-filter results in a signal with a full width half maximum (FWHM) of 12 nm at 1015 nm. Amplification of the signal by commercially available Yb-doped aluminosilicate fibers is challenging due to their gain profile (with a maximum gain at 1027 nm). It results in an undesirable power shift of the central wavelength from 1016 nm to longer wavelengths. This is mitigated by using a Yb-doped phosphosilicate fiber with an appropriate length, which has a smoother gain profile with a maximum at shorter wavelengths (around 1007 nm). As a result, we achieve nearly 10 nJ pulses at 40 MHz with a central wavelength

of 1016 nm and an FWHM of 12 nm, making it an ideal seed source for Yb:YLF amplifiers with the widest bandwidth at 1016 nm known to our knowledge to date.

Zusammenfassung

Faserlaser wurden kurz nach der Erfindung des ersten Lasers [1,2] vorgeschlagen und als potenzielle Kandidaten für zahlreiche industrielle und wissenschaftliche Anwendungen identifiziert [3,4]. Es gibt eine Reihe einzigartiger Merkmale, die Faserlaser von anderen Lasertechnologien unterscheiden und zu einer überlegenen Gesamtleistung führen, wie z. B. ein besseres Wärmemanagement aufgrund des großen Verhältnisses von Oberfläche zu Volumen, eine hervorragende Strahlqualität, höheren Gesamtwirkungsgrad, geringere Kosten und eine kleinere Grundfläche im Vergleich zu Festkörperlasern. Diodengepumpte Yb-dotierte Verstärkungsfasern mit geringem Quantendefekt und breiter Verstärkungsbandbreite ermöglichen eine Pulsverstärkung im sub-ps-Bereich, was sie für die Herstellung kompakter Laserquellen mit hoher Repetitionsrate und hoher mittlerer Leistung bei 1 µm für ein breites Spektrum von Anwendungen attraktiv macht.

In dieser Arbeit demonstrieren wir zwei ultraschnelle Yb-dotierte Front-End-Lasersysteme mit hoher mittlerer Leistung und hoher Repetitionsrate als Seed-Quellen für (i) High Harmonic Generation (HHG) und (ii) kryogen gekühlte Yb:YLF-Verstärker. Dementsprechend befasst sich der erste Teil der Arbeit mit der Entwicklung eines Faserlasersystems bei 1030 nm der Pulse mit 44 fs Pulsedauer und einer mittleren Leistung von 68 W bei einer Repetitionsrate von 1 MHz erzeugt. Der Laser benützt die Chirped Pulse Amplification (CPA)-Technik und besteht aus einem polarization evolution (NPE) modengekoppelten Yb-dotierten Faseroszillator als Seeder, einem Chirped Fiber Bragg Grating (CFBG) Stretcher, einem Wave Shaper zur Manipulation des Signalspektrums und der Phase, einer Faservorverstärkerkette, einem stabförmigen Yb-dotierten Faserverstärker (YDF) mit großem Pitch und schließlich zwei Kompressionseinheiten. Wir verwenden einen Wave Shaper (Finisar), um das Spektrum des gestreckten Signals zu manipulieren, um die spektralen Amplitudenmodulationen zu glätten und es in ein nahezu parabolisches Spektrum zu bringen. Das Ergebnis ist ein annähernd transformationsbegrenzter, Untergrund freier Puls mit einer gemessenen Dauer von 158 fs aus einem linearen Kompressor. Wir verkürzen die Dauer des Ausgangspulses auf 44 fs, die für die Erzeugung von High Harmonic Generation (HHG) erforderlich ist, indem wir einen nichtlinearen Kompressor vom Herriott-Typ mit mehreren Durchgängen und mehreren Platten verwenden.

Im zweiten Teil stellen wir eine ultraschnelle Faserlaser-Seed-Quelle bei 1016 nm für Yb:YLF-Verstärker vor. Wir entwickeln einen hybriden modengekoppelten Faseroszillator, der auf einem nichtlinearen Interferometer als schnell sättigbarem Absorber in Kombination mit einem Halbleiter-Sättigungsabsorberspiegel (SESAM) als langsam sättigbarem Absorber in der Laserkavität basiert, um die Modenkopplung zuverlässig zu starten. Der Faserlaser arbeitet im Einzelpulsbereich (bei niedrigen Pumpleistungen) als selbststartender modengekoppelter Oszillator mit hoher Stabilität und geringem Intensitätsrauschen. Im nächsten Schritt wird das Ausgangssignal durch Selbstphasenmodulation (SPM) im nachfolgenden Vorverstärker in einer Yb-dotierten Aluminosilikat-Verstärker-Faser spektral verbreitert. Die Filterung mit einem

Bandpass-Filter führt zu einem Signal mit einer Halbwertsbreite (FWHM) von 12 nm bei 1015 nm zentraler Wellenlänge. Die Verstärkung des Signals durch handelsübliche Yb-dotierte Aluminosilikatfasern ist aufgrund ihres Verstärkungsprofils (mit einer maximalen Verstärkung bei 1027 nm) schwierig. Dies führt zu einer unerwünschten Leistungsverschiebung der zentralen Wellenlänge von 1016 nm zu längeren Wellenlängen. Dieser Wellenlängenverschiebung wird durch die Verwendung einer Yb-dotierten Phosphorsilikatfaser mit geeigneter Länge abgeschwächt, die ein glatteres Verstärkungsprofil mit einem Maximum bei kürzeren Wellenlängen (etwa 1007 nm) aufweist. Als Ergebnis erreichen wir fast 10 nJ Pulse bei 40 MHz mit einer zentralen Wellenlänge von 1016 nm und einer FWHM von 12 nm, was den Laser zu einer idealen Seed-Quelle für Yb:YLF-Verstärker macht, die eine hohe Bandbreite bei 1016 nm haben.

PUBLICATION LIST

Publications in refereed journals

1. M. M. Sedigheh, M. Pergament, G. Kulcsar, M. Seidel, Y. Liu, M. Edelmann, M. Kellert, C. M. Heyl, And F. X. Kärtner, “A 44fs, 1MHz, 70µJ Yb-doped fiber laser system for high harmonic generation”, in preparation for Optics Express (2023).
2. M. M. Sedigheh, M. Edelmann, M. Pergament, And F. X. Kärtner,”1uJ, 1016nm ultrafast Yb-fiber laser seeder for cryogenic Yb:YLF amplifier system”, in preparation for Optics Express (2023).
3. N. H. Matlis, Z. Zhang, Ü. Demirbas, C. Rentschler, K. Ravi, M. Youssef, G. Cirmi, M. Pergament, M. Edelmann, S. M. Mohamadi, S. Reuter, and F. X. Kärtner, “Precise parameter control of multicycle terahertz generation in PPLN using flexible pump pulse trains”, in preparation (2023).
4. Marvin Edelmann, Mikhail Pergament, Yi Hua, Malek M. Sedigheh, and Franz X. Kärtner, “Fiber-Interferometric Second Harmonic Generator with Dual-Color Standard Quantum-limited Noise Performance”, in preparation for Optics Express (2023).
5. M. Edelmann, M. M. Sedigheh, Y. Hua, E. C. Vargas, M. Pergament, and F. X. Kärtner, "Large-mode-area soliton fiber oscillator mode-locked using NPE in an all-PM self-stabilized interferometer," Appl. Opt., AO **62**(7), 1672–1676 (2023).
6. Y. Liu, Y. Hua, S. Malek. M., M. Pergament, and F. Kärtner, "10-Hz, 636-ps, 1064-nm, all polarization-maintaining fiber front-end based on ultrafast optical fiber pulse chopping," Optics Express **29**, (2021).

Publications in refereed conferences

1. M. M. Sedigheh, M. Pergament, Y. Liu, M. Seidel, M. Edelmann, M. Kellert, C. M. Heyl, And F. X. Kärtner, "70W, 1MHz, sub-50fs Yb-doped fiber laser system for high harmonic generation," accepted in *Conference on Lasers and Electro-Optics Europe (2023).*
2. Y. Liu, Y. Hua, S. M. Mohamadi, M. Pergament, and F. X. Kärtner, "10-Hz, 636-ps, 1064-nm, All Polarization-Maintaining Fiber Front-End Based on Ultrafast Optical Fiber Pulse Chopping," in *Conference on Lasers and Electro-Optics (2021), Paper SM3P.6* (Optica Publishing Group, 2021), p. SM3P.6.

Contents

List of Figures

List of Tables

1. Introduction

Ultrafast lasers delivering high energy per pulse enable various applications such as light-matter interactions [5], advanced material processing capabilities [6], industrial micromachining, surface ablation and texturing of metals [7], laser-particle acceleration [8], nonlinear and attosecond science [9], high harmonic generation (HHG) [10,11], advancements in femtosecond and attosecond spectroscopy to enhance the detection sensitivity [12] and time-resolved coincidence spectroscopy [13]. The technology to generate high-power amplified ultrafast pulses has advanced rapidly with the invention of the chirped pulse amplification technique in 1985 [14–19]. Intense ultrashort pulses can be used as a powerful tool for observing physical phenomena. In particular, pulses in the extreme ultraviolet (EUV or XUV) and X-ray regions enable unique and higher resolution measurements than are possible with longer wavelengths [20]. The technique of higher-order harmonic generation (HHG) allows scientists to generate light in these spectral regions by starting with lasers operating at more accessible wavelengths. There are other alternative approaches for generating laser-like EUV and X-ray beams, such as synchrotrons and free-electron lasers (FELs). Synchrotrons and FELs are facility-scale sources that can produce very bright beams in the EUV and X-ray range with tunable wavelength and improved coherence and temporal duration. Despite the many advantages of these large-scale sources, their cost and accessibility can be preventive in some cases. Fortunately, HHG is a supplementary technology that offers more opportunities for experimentation, but at the expense of the brightness and spectral range of available sources.

HHG describes a frequency conversion technique in which an intense driving laser is focused into a medium, such as a noble gas, and harmonic frequencies of the driving laser are emitted as a result of extreme laser-matter interaction [21–23]. HHG radiation is used for a wide range of applications, including high-resolution microscopy, spectroscopy, and measurements of magnetism, heat transport, and molecular structure [24–27]. In the last decade, HHG sources with different parameters such as peak power or repetition rate have been generated [28]. The rapid

development in laser technology leads to an increased variety of laser drivers for HHG. High-energy titanium–sapphire lasers at low repetition rate and high-average-power lasers based on optical parametric amplification are examples of such lasers [29–32]. In addition, compact high-power HHG sources based on post-compressed ytterbium-doped femtosecond lasers are of increasing interest for different applications [33,34]. The use of lasers in the mid-infrared range enables the generation of high-energy photons in the soft X-ray range [35–37]. Moreover, high-power ultrafast Yb-doped sources can drive HHG with a higher repetition rate. A high repetition rate EUV light source is beneficial for reducing data acquisition time in applications such as angle-resolved photoemission spectroscopy (ARPES) [38]. ARPES is a method for studying the electronic structure of solids. Direct access to the electronic band structure of the medium is possible by extracting the kinetic energy and angular distribution of photoelectrons. ARPES can be extended to the time domain by applying a pump-probe scheme. In a time-resolved ARPES experiment (tr-ARPES), a small fraction of the electrons of the material is excited by a femtosecond laser pulse in the visible or infrared region. The excited state and its evolution over time can be monitored by photoemission, with another femtosecond pulse in the XUV region at a precisely-defined time after the initial pulse. The entire first Brillouin zone (BZ) of most materials can be covered by combining the advantages of a high signal-to-noise ratio at high repetition rate with large probe photon energies that extend the parallel moments accessible in a time-resolved ARPES experiment [39]. In the first part of this dissertation (including chapters 1 to 4), we report the development of an ultra-fast, high repetition rate, high-power fiber laser system at 1 µm for HHG to be deployed in a Tr-ARPES setup, that is currently served by a lower repetition rate Ti:Sapphire system. In the following section, we explain different approaches for generating ultrashort high-energy pulses, as well as the reasons for fabricating a Yb-doped fiber laser system for this particular application.

1.1 High peak and average power laser systems

Development of high-power ultrashort pulses initiated by the step from the dye laser technology to solid-state lasers [19]. The solid-state lasers using rods as gain media e.g. titanium-doped sapphire as the most widely used [40] have the potential to produce significantly higher powers, higher pulse energies and shorter pulse durations with higher reliability than dye lasers. However, scaling these systems in terms of average power is difficult due to high thermal effects, the lack of direct diode pumping possibilities and low optical-to-optical efficiencies [19]. In addition, the

complexity of high-power Ti:sapphire short pulse lasers limits the use of ultrashort pulse laser technology in the industry. Recently, the development of diode-pumped solid-state lasers such as Yb:YAG has brought great progress in terms of efficiency. In order to overcome thermo-optical effects, which limit the power scaling capability of these systems, several novel gain-media designs have been introduced such as thin disks or slabs [41]. However, due to the low single-pass gain of these materials, complicated schemes such as regenerative amplifiers are required to gain a reasonable output power [42,43]. Therefore, long-term stability, robustness, and compactness are challenges in the design of ultra-short pulsed solid-state laser systems. Alternatively, the gain medium can be shaped to be long and thin, resulting not only in excellent thermo-optical properties but also in very high single-pass gain. Fiber-based laser systems have a reputation for being more immune to thermo-optic problems due to their special geometry. Their excellent heat dissipation due to their significant surface-to-active fiber volume ratio provides the engineering leverage to achieve high average capacities. The beam quality of the guided mode is determined by the design of the fiber core and is therefore independent of the output power [44,45]. Furthermore, the complete integration of the lasing into a waveguide enables the inherent compactness and long-term stability of fiber lasers.

Most notably, Ytterbium-doped glass fibers with the inherent low quantum defect can provide about 80% of optical-to-optical efficiencies and, therefore, low thermal load [46]. These fiber laser systems are of particular interest for the generation and amplification of ultrashort high-power pulses due to several unique properties [47]. In ytterbium-doped glass fibers, the amplification bandwidth of approximately 40 nm supports, in principle, pulses of durations as short as ∼30 fs. Therefore, a broad emission spectrum enables ultrashort pulse amplification in this gain medium. Furthermore, the absorption spectrum covers a wavelength range in which powerful diode lasers are commercially available. Besides, the long fluorescence lifetime (∼1 ms) of the upper laser level leads to a high-energy storage capability. Only two energy level manifolds are relevant for all optical wavelengths in ytterbium. As a result, excited-state absorption of pump or signal radiation, or concentration quenching by ion-ion energy transfer processes, does not occur within this amplifier [19].

The development of high-power fiber lasers became possible through the invention of the double-clad fiber concept by Snitzer in 1988 [48]. In this fiber, the active core is surrounded by a second waveguide which is highly multimodal. Diode laser radiation with low brightness and high power can be coupled into this second waveguide, also called inner cladding or pump core. This pump light is gradually absorbed along the entire fiber length and converted into bright, powerful laser radiation. Thus, double-clad rare-earth doped fibers can provide a highly efficient brightness improvement by pump-to-laser radiation conversion by the laser process itself.

The output average power of fiber lasers has increased significantly by an average factor of 1.7 each year, corresponding to about 2 orders of magnitude over the past decade (Fig. 1) [12]. These increased power levels lead to a rapid penetration in applications that were previously dominated by other lasers. The privilege of fiber lasers, however, goes beyond their ability to produce high

optical power, as they own other physical characteristics that distinguish them from other classes of lasers in terms of functionality and performance. These include the following features:

- Robust single-mode (transverse) operation in single-mode fibers, which in particular provides a significant degree of freedom from thermally induced mode distortions common to solid-state lasers [49].

- Relatively wide gain bandwidths (up to 20 THz), enabling ultra-short pulse operation and broad wavelength tunability [50].

- Accessibility of high gains, offering the possibility of master oscillator power amplifiers (MOPA) [51].

- Low quantum defect and ultra-high optical conversion efficiencies [52].

- Ability for fabricating all-fiber cavities and pre-amplifiers without the need for careful alignment of free space components, resulting in robust and compact system designs [53].

Mentioned properties have played an important role in driving the commercial interest and relatively rapid development and practical use of fiber lasers.

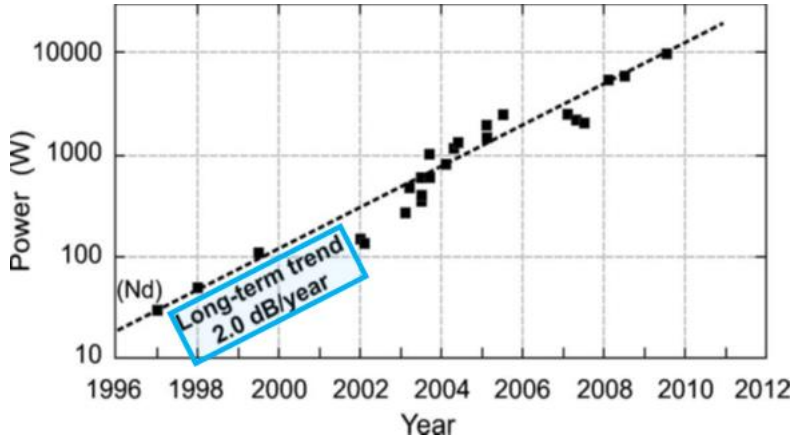

Fig. 1.1 Progress in output power from diffraction-limited and near-diffraction-limited fiber lasers. Since 1999, all results are with Yb-doped fibers. Reprinted with permission from [12]

However, the confinement of the laser radiation and the long interaction length make fibers attractive, but nonlinear effects impose fundamental limitations on these systems that can lead to severe pulse distortion and even damage to the fiber. The lowest-order nonlinear effect in optical fibers originates from the third-order susceptibility $\chi^{(3)}$ which is responsible for an intensity-dependent refractive index in the form of $n = n_0 + n_2 I$.

Accordingly, an optical field propagating through a fiber undergoes a self-induced phase shift, a phenomenon called self-phase modulation (SPM). A second important class of nonlinear effects arises from stimulated inelastic scattering, in which the radiation transfers part of its energy to the glass host in the form of excited vibrational modes [54]. A large wavelength shift (~46 nm) is observed by the excitation of optical phonons in a nonlinear process called stimulated Raman scattering (SRS), while the excitation of acoustic phonons leads to a much smaller shift (~60 pm), called stimulated Brillouin scattering (SBS) [55]. Both nonlinear processes are known as significant power loss mechanisms in fiber-based laser systems. The effect of SBS in the context of ultrashort pulse amplification in fibers can be neglected because the spectra are significantly broader than the Brillouin gain bandwidth [56].

Both the nonlinear index n_2 and the gain coefficients of SRS and SBS are at least two orders of magnitude smaller than in other common nonlinear media [57]. However, the nonlinear coefficient is inherently smaller, but due to the small core size and long interaction length within the fiber, nonlinear effects are observed at very low powers and limit the performance of pulsed rare-earth doped fiber systems. To circumvent this limit, some approaches have been developed such as fiber designs with intrinsically reduced nonlinearity i.e. an increased mode-field diameter and a reduced fiber length which will be discussed in the next section.

1.2 Large mode area fibers (LMA)

As discussed, the nonlinear effects are proportional to the fiber length, nonlinear index and peak power in the fiber core, and inversely proportional to the wavelength and the mode-field area of the guided radiation in the fiber. Thus, one technique to decrease the nonlinear effects at high powers can be an enlargement of the mode-field diameter and a reduction of fiber length. The mode field area of single transverse mode fibers has significantly increased employing special techniques and fiber designs in recent years. The modal properties can be investigated by a parameter called V number:

$$V = \frac{2\pi}{\lambda}\, a_{eff}.NA = \frac{2\pi}{\lambda}\, a_{eff}.\sqrt{n_{core}^2 - n_{clad}^2}$$

n_{Core}, n_{Clad}; the effective refractive indices of the core and cladding of the fiber with a core radius of a_{eff} and numerical aperture of NA. It can be shown that a fiber becomes single-mode for $V < 2.405$ [58]. Therefore, one approach to fabricate single-mode fibers with a large mode area is to reduce the numerical aperture, which has become the most commonly used fiber

concept with low nonlinearity in recent years. The reduction of the refractive index difference between the core and the cladding leads to a lower numerical aperture and v-number in step-index fibers. However, the guidance then becomes weak, and considerable losses may occur in response to small imperfections of the fiber or bending. Accordingly, the numerical aperture should not usually be less than about 0.06%. Some LMA fibers have V-parameters in the range of 5-10, capable of guiding several higher-order transverse modes. In this case, bending the fiber with a suitable bend curvature helps to achieve stable fundamental mode operation of a fiber laser or amplifier [59].

For higher performance, robust and environmentally compatible fundamental mode operation in even larger cores is required. Micro-structuring the fiber by inserting air-holes generates several attractive properties. These fibers, known as photonic crystal fibers (PCF), have been one of the hot research topics in the past decade [60]. Solid core photonic crystal fibers consist of a regular array of air-filled holes characterized by the hole diameter d and the pitch (distance between two adjacent holes) Λ. The effective cladding index is strongly dependent on λ/Λ in a PCF fiber. Moreover, in the limiting case $\lambda/\Lambda \rightarrow 0$, the effective cladding index tends to the value of the core index, resulting in a very small numerical aperture [61].

Another advantage of micro-structuring a fiber is the ability to form an air-clad region to create double-clad fibers [62]. A double cladding PCF can be formed by creating a network of silica bridges surrounding the inner cladding. The result is a very high numerical aperture of the inner cladding up to 0.8. This leads to a reduction in the diameter of the inner cladding. A higher core-to-inner clad overlap ratio results in a shorter absorption length and thus less nonlinearity [63,64]. Jens Limpert and others developed a fiber design in 2005 that exhibits extremely reduced nonlinearity. This type is called a rod-type photonic crystal fiber (RTF) [65]. The fiber has the external dimensions of a rod laser, i.e. a diameter in the range of a few millimeters and a length of a few tens of centimeters. The pump light is confined by an air cladding and the laser light is guided in an array of air holes. Such a fiber has extremely low nonlinearity and therefore allows significant power and energy scaling.

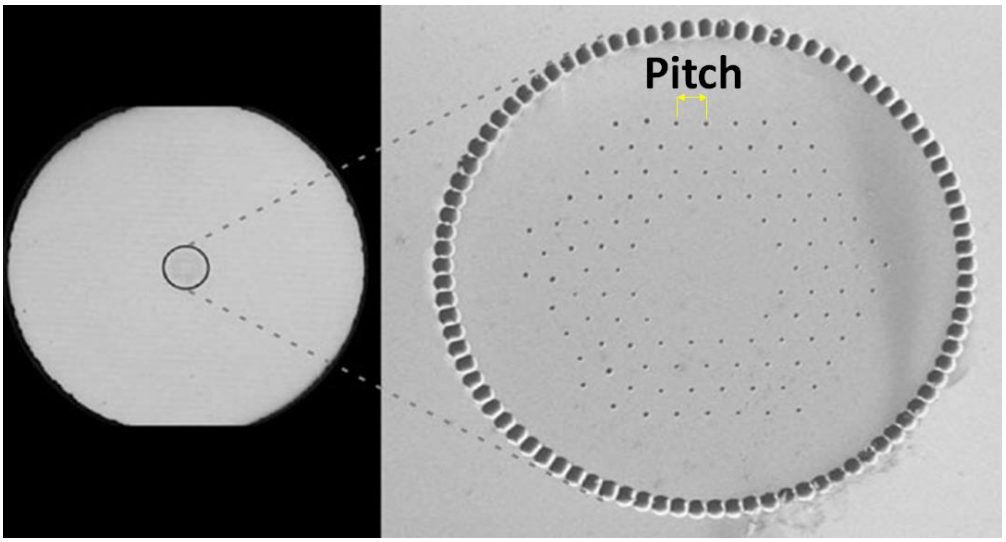

Fig. 1.2 Microscope image of rod-type photonic crystal fiber. Reprinted with permission from [66].

The cross-section of this fiber is shown in Fig. 1.2. The pump cladding has a diameter of ~260 µm. The numerical aperture is up to 0.5. The ytterbium-doped core has a diameter of 85 µm. This fiber exhibits a pump light absorption of ~15 dB/m at 976 nm. Normally, obtaining a high output power from short fibers is limited by thermo-optical problems.

Power scaling in high-power fiber lasers is also limited by polymer coating damage, which occurs at fiber surface temperatures between 100 ˚C and 200 ˚C [67]. These temperatures are easily reached when power is taken up to the 100 W range. The coating in a conventional double-clad fiber must have a lower refractive index than quartz glass and therefore forms the waveguide for the pump radiation. In a micro-structured air-clad fiber, on the other hand, it serves only to protect the fiber from mechanical damage and chemical exposure. Therefore, the easiest way to avoid damaging the coating in this fiber is to remove it.

This is possible if the fiber itself is thick enough to ensure sufficient mechanical stability. The fiber shown in Fig. 1.2 has a cladding outer diameter of up to 2 mm and has no coating. Moreover, the larger outer diameter improves the heat dissipation of this fiber [67]. This fiber design shows a reduction in nonlinearity by a factor of about 2000 in the rod-type PCF compared to conventional single-mode fibers. Therefore, this fiber has significant potential in power and energy scaling due to the lowest nonlinearity and was used as the main fiber amplifier in our system.

1.3 Ultra-short pulse amplification methods in fiber laser systems

There are basically two approaches to amplify ultrashort laser pulses in fibers. The first, which exploits nonlinearity, is parabolic pulse amplification; the second, which is based on avoiding nonlinearity, is chirped pulse amplification (CPA). In parabolic amplification, the interplay of normal dispersion, nonlinearity (self-phase modulation), and gain produces a parabolic-shaped pulse called similariton with a linear chirp that can be efficiently removed by a grating-pair compressor [68,69]. Characteristics of the similariton are not influenced by the shape or width of the input pulse. Only the initial pulse energy determines the final pulse amplitude and width [70]. This method is used to generate parabolic-shaped pulses from oscillators and pre-amplifiers.

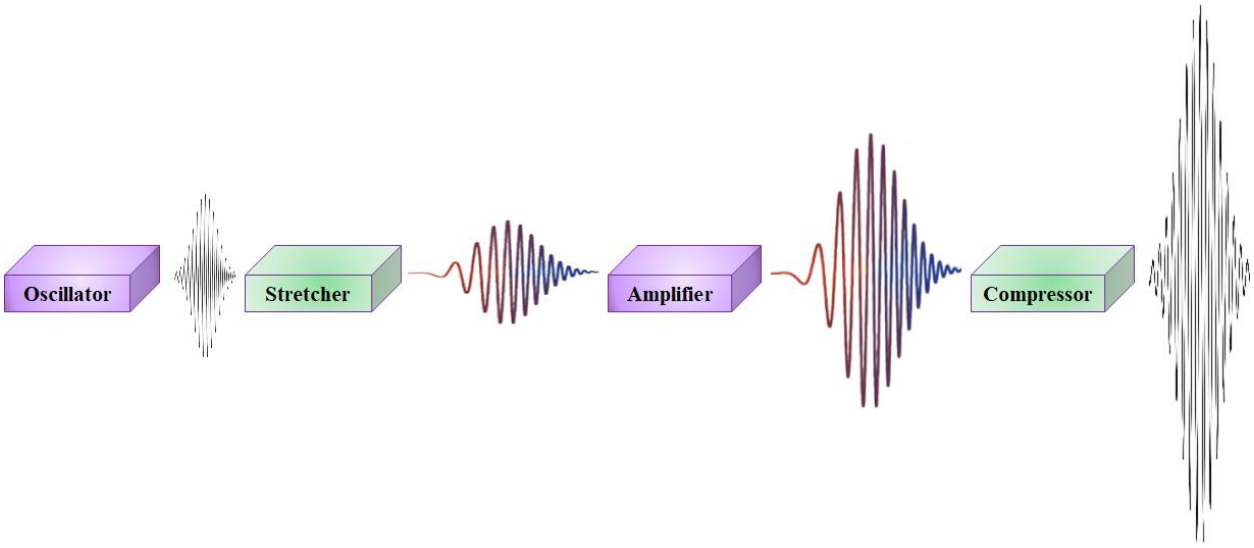

Fig. 1.3 Chirped pulse amplification (CPA) technique.

To significantly increase the average power or pulse energy of fiber laser systems, the CPA technique must be used to avoid very high nonlinearities. A basic schematic of this technique is shown in Fig. 1.3. By stretching the pulses in the time domain, the peak pulse power is reduced so that nonlinear pulse distortions can be avoided to some extent. In a fiber-based CPA system, sufficient pulse stretching and increasing the mode field diameter of the fiber to reduce nonlinear effects such as SRS and SPM, are key points to boost the output parameters. However, output power higher than 1 kW has been reported from a continuous-wave fiber laser with a high beam quality using this technique [19], but generating high-energy pulses from a fiber-based laser system still remains the biggest challenge. Even significant stretching of pulses cannot avoid the formation of enormous peak power levels in the fiber amplification stages. Therefore, a higher pulse energy requires a larger stretch factor and the use of an acousto-optic modulator to reduce the pulse repetition rate. Consequently, the pulse energy is increased when the average power is boosted up in the following amplifiers.

Another nonlinear-avoiding amplification is divided-pulse amplification (DPA) in which each pulse is divided into a sequence of several pulses by a divider before amplification. These pulses are amplified and again recombined in the combiner to generate the high-power output pulse. This technique has some limitations. For pulses shorter than 1 ps, the effect of pulse broadening via chromatic dispersion of the birefringent crystals as pulse dividers/combiners can become problematic with DPA. As a consequence, chirped pulse amplification is generally better suited for pulse durations well below 1 ps, as is the case in our system, while split pulse amplification offers advantages for longer input pulses.

Our fiber laser system, based on chirped pulse amplification (CPA), generates an average power of up to 70 W at a repetition rate of 1 MHz and a pulse duration of 44 fs. The output parameters perfectly match the requirements of HHG with reasonable time resolution and data acquisition time. In the next chapters, the design, experimental setup, and results are discussed in detail.

2. Design and simulation of sub-50-fs, 1MHz Yb-doped fiber laser system

2.1 Numerical analysis for Yb-doped fiber amplifier

Rate equations can be set up to model the two Stark-split manifolds of the Yb ions in fiber (with the different host glass compositions) as two effective energy levels [47], with electron population densities N_1 and N_2 for the effective ground and excitation level, respectively (see Fig. 2.1). These equations describe the evolution of the frequency-depended optical signal/pump power, and the population of two effective electronic energy levels along the fiber.

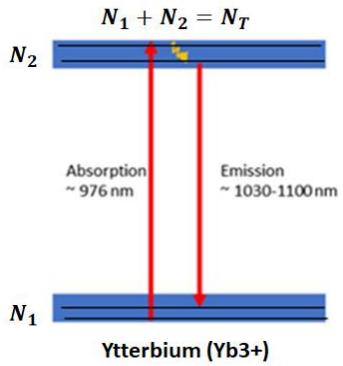

Fig. 2.1 Energy levels of Yb3+ ions in aluminosilicate fiber, and the typical pump and laser transition.

The optical signal power evolution depends on the amount of light absorbed by the lower level and emitted by the upper level, as well as fiber losses:

$$\frac{\partial P_\lambda}{\partial z} + \frac{1}{v_p(\lambda)}\frac{\partial P_\lambda}{\partial t} = \Gamma(\sigma_e(\lambda)N_2 - \sigma_a(\lambda)N_1)P_\lambda - \eta P_\lambda \qquad (2.1)$$

Where P_λ denotes the optical power at a given wavelength λ, $\sigma_e(\lambda)$ is the emission cross section at that wavelength, $\sigma_a(\lambda)$ is the absorption cross-section, η is the fiber losses, $v_p(\lambda)$ is the phase velocity, and Γ is the overlap factor and indicates the overlap between the guided light and the doped rare earth ions in the core. The time-dependent change of the upper-level population depends on the lifetime of electrons on the N_2, the number of electrons transferred to the upper level due to photon absorption, and depopulated due to stimulated emission:

$$\frac{\partial N_2}{\partial t} = \frac{\Gamma}{hcA_c}\sum_{m=1}^{M}\lambda_{\mathrm{m}}(\sigma_a(\lambda_m)N_1 - \sigma_e(\lambda_m)N_2)P(\lambda_m) - \frac{N_2}{\tau} \qquad (2.2)$$

where τ is the upper-level lifetime, h is Planck's constant, and A_c denotes the core area. Considering the evolution of both pump and signal power along the fiber and applying the wavelength-dependent cross sections, the rate equations for a negligible amplified stimulated emission (ASE) can be expressed as:

$$\frac{\partial N_2}{\partial t} = \frac{\Gamma_{\mathrm{p}}}{hcA_c}\sum_{j=1}^{J}\lambda_j^{\mathrm{p}}\left[\sigma_a\left(\lambda_j^{\mathrm{p}}\right)N_1 - \sigma_e\left(\lambda_j^{\mathrm{p}}\right)N_2\right]P_p\left(\lambda_j^{\mathrm{p}}\right)$$

$$+\frac{\Gamma_{\mathrm{s}}}{hcA_c}\sum_{k=1}^{K}\lambda_k^{\mathrm{s}}\left[\sigma_a(\lambda_k^{\mathrm{s}})N_1 - \sigma_e(\lambda_k^{\mathrm{s}})N_2\right]P_s^{\pm}(\lambda_k^{\mathrm{s}}) - \frac{N_2}{\tau} \qquad (2.3)$$

$$N_1 = N_T - N_2 \qquad (2.4)$$

$$\frac{\partial P_p^{\pm}(\lambda_j^p)}{\partial z} \pm \frac{1}{v_p(\lambda_j^p)}\frac{\partial P_p^{\pm}(\lambda_j^p)}{\partial t} = \pm[\Gamma_{\mathrm{p}}\left(\sigma_e\left(\lambda_j^p\right)N_2 - \sigma_a\left(\lambda_j^p\right)N_1\right)P_p^{\pm}(\lambda_j^p) - \eta_p P_p^{\pm}(\lambda_j^p)] \qquad (2.5)$$

$$\frac{\partial P_s^{\pm}(\lambda_k^s)}{\partial z} \pm \frac{1}{v_p(\lambda_k^s)}\frac{\partial P_s^{\pm}(\lambda_k^s)}{\partial t} = \pm[\Gamma_{\mathrm{s}}(\sigma_e(\lambda_k^s)N_2 - \sigma_a(\lambda_k^s)N_1)P_s^{\pm}(\lambda_k^s) - \eta_s P_s^{\pm}(\lambda_k^s)] \qquad (2.6)$$

where η_p and η_s are the pump and signal losses, N_T is the doping concentration which is assumed to be constant throughout the fiber, $P_p^{\pm}$ and $P_s^{\pm}$ are the pump and signal power of the forward, $+$, and backward, $-$, propagating beams. The steady state is reached when the time derivatives in the above equations are zero. Therefore, the steady-state equations contain only z-derivatives and can be solved by the fourth-order Runge-Kutta (RK4) method [71–73]. Consequently, the wavelength-dependent gain parameter for each small step size of Δz in the fiber can be solved as:

$$Gain(\lambda, z + \Delta z) = \frac{1}{2\Delta z} log\left(\frac{P_s(\lambda, z+\Delta z)}{P_s(\lambda, z)}\right) \qquad (2.7)$$

The generalized nonlinear Schrödinger equation (GNLSE) is solved also using the RK4 method [74], which alternates between the Fourier domain to evaluate dispersive effects and the time domain to evaluate nonlinear effects. With this method, the GNLSE is expressed by the following dispersive and nonlinear operators, respectively [75]:

$$\widehat{D} = -\frac{1}{2}\left(\alpha(\omega_0) + \sum_{l=1}^{\infty} \alpha_l \frac{i^l}{l!}\frac{\partial^l}{\partial T^l}\right) - \left(\sum_{n\geq 2} \beta_n \frac{i^{n-1}}{n!}\frac{\partial^n}{\partial T^n}\right) \quad (2.8)$$

$$\widehat{N} = i\gamma(\omega_0)\frac{1}{A}\left(1 + \frac{i}{\omega_0}\frac{\partial}{\partial T}\right) A \int_{-\infty}^{\infty} R(\tau)|A(z, t-\tau)|^2 d\tau \quad (2.9)$$

where A represents the complex electric field envelope, ω_0 is the central angular frequency, z is the position along the fiber, T is the time in the frame moving at the pulse's group velocity and is equal to $(t - \beta_1 z)$, α is the absorption (gain) coefficient, β_n are the Taylor expansion coefficients for the mode-propagation constant $\beta(\omega) = \frac{n_{eff}(\omega)\omega}{c}$ (and describes the dispersion coefficients), where $n_{eff}\ (\omega)$ is the effective refractive index at the angular frequency ω. The nonlinear response function, $R(\tau)$, is expressed as:

$$R(\tau) = (1 - f_R)\delta(\tau) + f_R \frac{\tau_1^2 + \tau_2^2}{\tau_1 \tau_2^2}\theta(\tau) e^{\frac{-\tau}{\tau_2}} sin\left(\frac{\tau}{\tau_1}\right) \quad (2.10)$$

where f_R denotes the fractional contribution of the Raman response, $\theta(\tau)$ is the Heaviside step function, τ_1 and τ_2 are parameters to adjust the function to the Raman gain spectrum. The nonlinear parameter is defined as $\gamma(\omega_0) = 3\omega_0\, Re\,(\chi^{(3)})/(4\epsilon_0 c^2 n^2(\omega_0) A_{eff})$, where A_{eff} denotes the effective mode area, ϵ_0 the dielectric permittivity of free space and $\chi^{(3)}$the third-order electronic susceptibility.

Using equations (2.8) and (2.9), the GNLSE can be expressed in the following form:

$$\frac{\partial A}{\partial z} = \left(\widehat{D} + \widehat{N}\right)A \quad (2.11)$$

The linear part ($\widehat{D}$) represents the effects of dispersion and gain dispersion while the nonlinear part ($\widehat{N}$) represents SPM, self-steepening, and the Raman effect. In the split-step Fourier method, the solution to (2.11) over a step Δz is approximated by:

$$A(t, \Delta z) = e^{(\widehat{D}+\widehat{N})\Delta z} A(t, 0) = e^{\frac{1}{2}\widehat{D}\Delta z} e^{\widehat{N}\Delta z} e^{\frac{1}{2}\widehat{D}\Delta z} A(t, 0) \quad (2.12)$$

where the exponential dispersion operator is simply evaluated in the Fourier domain with the FFT. The dispersion and nonlinear operators do not commute, in general, and the solution (2.12) is only an approximation to the exact solution, with an error proportional to the second-order of the step size (Δz^2) [75]. However, for computational efficiency, the RK4 scheme is usually used. This method then gives an accuracy proportional to the fourth order of the used step size [74,75]. The numerical procedure to solve the GNLSE in the presence of optical amplification is described in the following. At first, the rate equations 2.3 to 2.6 are simplified with the steady-state approximation by setting the time derivatives equal to zero. Then, the z-dependent equations 2.5 and 2.6 are solved numerically using the RK4 technique for a small step of Δz. Calculating the

wavelength-dependent signal power ($P_s(\lambda)$) after each step yields the wavelength-dependent gain profile given by equation (2.7). Then the GNLSE (2.11) is calculated numerically again with RK4 method, knowing the gain and using the split-step Fourier method. With a MATLAB code written based on the described calculation technique, one can numerically determine the wavelength-dependent energy/power evolution of the pulse as it propagates along the fibers as well as its temporal and spectral evolution via linear and nonlinear effects.

This code can calculate the output parameters of a common single-clad fiber amplifier (such as Yb-401-PM from Coractive) as well as the behavior of the Double-Clad fibers (25/250 µm Nufern and photonic crystal large-core area RTA fibers) by applying the accurate overlap factor and gain parameters for each fiber type.

2.2 Simulation results

We design and simulate our all linearly-amplifying fiber laser system using the computational method explained in the last section to study the effect of gain narrowing and the output parameters after each fiber amplifier. Fig. 2.2 displays a schematic layout of the system consisting of a nonlinear polarization evolution (NPE) mode-locked Yb-doped fiber oscillator as a seeder, a chirped fiber Bragg grating (CFBG) stretcher, a wave-shaper for the signal spectrum and phase manipulation, a fiber pre-amplifier chain, a Rod-type large pitch Yb-doped fiber (YDF) amplifier and eventually two compression units. Simulation of the effect of the gain narrowing on the signal passing through the various amplification stages provides important information about the influence of the spectral shape of the input pulse on the final output spectrum. We find that for the smoother shape of the seeding spectrum, which is also closer to a parabola, the effect of gain narrowing is smaller, and a wider output spectrum is maintained after several stages of amplification. Since the output spectrum of the seeder is modulated, after each amplifier these fluctuations are amplified more and significantly affect the final output spectrum shape and bandwidth. In addition, suppression of the pedestal of the compressed pulse caused by the residual nonlinearity in the amplifier chain is easier when the spectrum has a parabolic shape [76–78]. Therefore, a wave shaper with arbitrary filter shapes can solve this problem and help to increase the final output bandwidth with a smoother spectral shape.

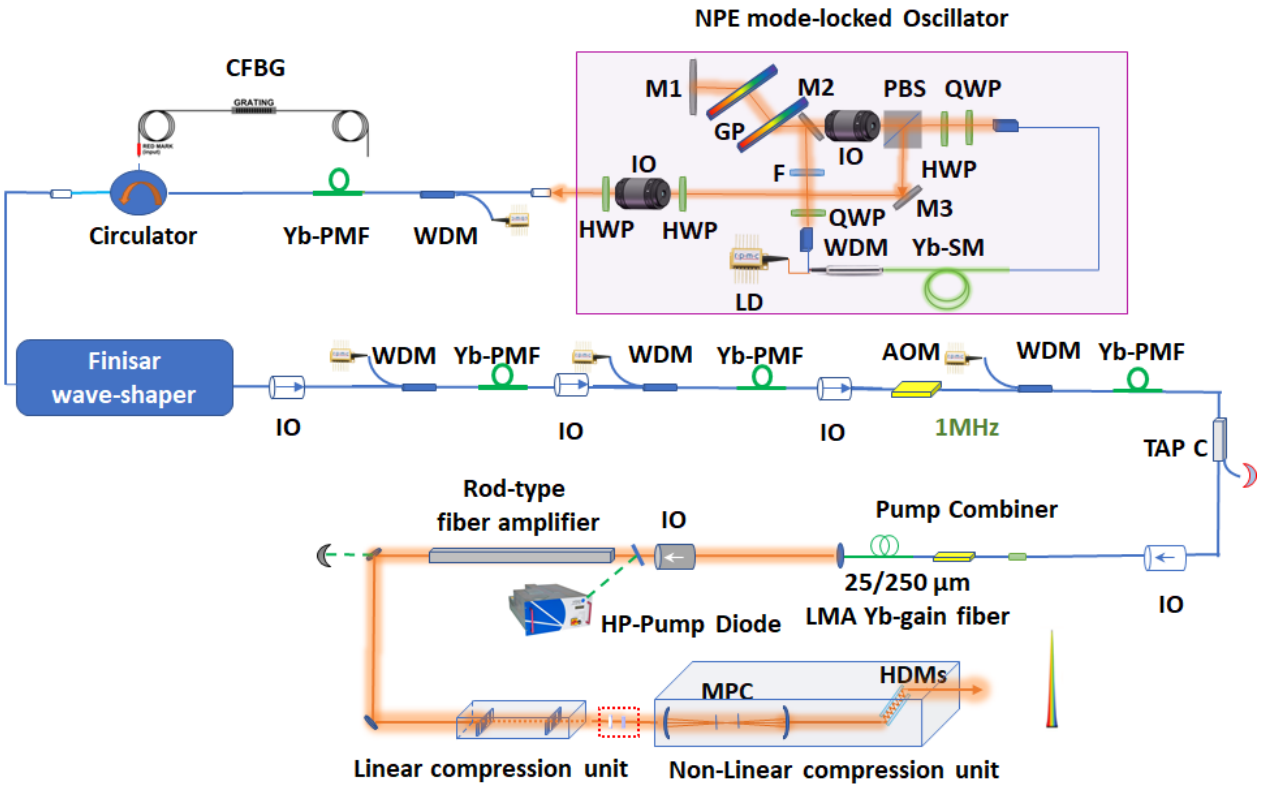

Fig. 2.2 Schematic layout of laser system. WDM, wavelength division multiplexer; Yb-SMF, Yb-doped single mode fiber; M, mirror; PMF, polarization maintaining fiber; QWP, quarter-wave plate; HWP, half-wave plate; F, bandpass filter; PBS, polarization beam splitter; GP, grating pair; LD, laser diode; CFBG, chirped fiber Bragg grating; IO, isolator; AOM, acousto-optic modulator; LMA, large mode area fiber; HP, high-power; MPC, multi-pass cell; HDM, highly-dispersive mirror.

Studying the gain narrowing effect after each stage also helps to understand the behavior of the temporal shape and duration of the signal and therefore the peak power through the system. Accordingly, we calculate the best stretch factor by investigating the nonlinearities within the fibers and controlling the B integral over the entire system to less than 10 rad by modeling the pulse characteristics along the fibers.

The stretcher must provide an adequate stretch factor to mitigate nonlinearities such as SPM, SRS, and self-steepening throughout the system (in all preamplifiers and high-power fiber amplifiers). According to our calculations, these effects can be mitigated in our system if the pulse is stretched to 1 ns. For this reason, a chirped fiber Bragg grating (CFBG) with a GDD of 30.1 ps^2 is required. Then, a Treacy compressor is designed to fully compensate for the dispersion parameters of the CFBG and other optical components in the laser. Depending on the total GDD of the system, a compressor (see section (2.3)) can be designed with appropriate parameters that yield a specific TOD and FOD and can be used to calculate the required amounts of these parameters in the CFBG. Finally, a CFBG with a GDD of 30.1 ps^2, a TOD of -0.4 ps^3 and a FOD of

0.00875 ps^4 can provide a suitable stretch factor to mitigate the nonlinearities in the system and be fully compressible with the linear compressor we develop. With this CFBG, the pulse duration is stretched to about 1 ns. In our system, the AOM reduces the repetition rate to 1MHz. Therefore, with a suitable stretching factor, pulses with higher energy are achievable using Double-Clad (DC) fiber amplifiers with inherently lower nonlinearities due to the larger core diameters. The calculated saturation power of the RTA is around 2-3 W, and 5 W seed then ensures that the RTA is fully saturated. Therefore, a 25/250-µm double-cladding preamplifier is required upstream of the main amplifier (RTA) to ensure sufficient seed power for full saturation of the RTA in conjunction with reduced nonlinearities.

The seeder in this design is a nonlinear polarization evolution mode-locked fiber laser, which consists of a transmission grating pair as a dispersion management device within the oscillator, discussed in our experimental results in the next chapter (24 MHz, 10 mW, 4.9 ps up-chirped pulses). The typical output spectrum of the seeder is shown in green in Fig. 2.3. As mentioned earlier, we use a parabolic filter with the help of a wave shaper to manipulate the spectrum of the stretched signal to attenuate the modulations and form it into a near parabolic spectrum. Therefore, we apply a parabolic filter as:

$$F(\upsilon)= 1 - \left(\frac{\sqrt{2}(\nu-\nu_0)}{\Delta\nu_{FWHM}}\right)^2 \qquad (2.13)$$

That ν_0 denotes the central frequency and $\Delta\nu_{FWHM}$ is the bandwidth at the full width of half maximum (FWHM). In practice, $\Delta\nu_{FWHM}$ is chosen large enough to alleviate the gain narrowing effect on the spectrum in the next amplifier chain and preserve wider FWHM for the output signal. Fig. 2.3 also shows the spectrum after filtering (the purple line) for $\Delta\nu_{FWHM} = 9\ GHz$, and the central wavelength of 1030 nm.

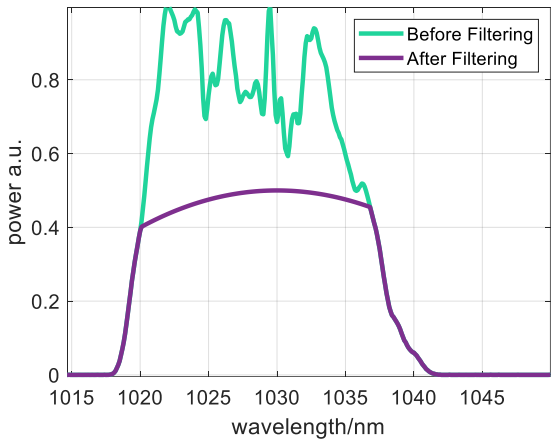

Fig. 2.3 The output spectrum before (green) and after (purple) filtering by a parabolic filter.

Starting from the filtered spectrum, we simulate the evolution of the spectral amplitude of the signal as it propagates through the different amplifiers, as shown in Fig. 2.4. In each figure, the

input (red) and the output spectra (blue) are plotted to observe the effects of the gain narrowing on the spectrum.

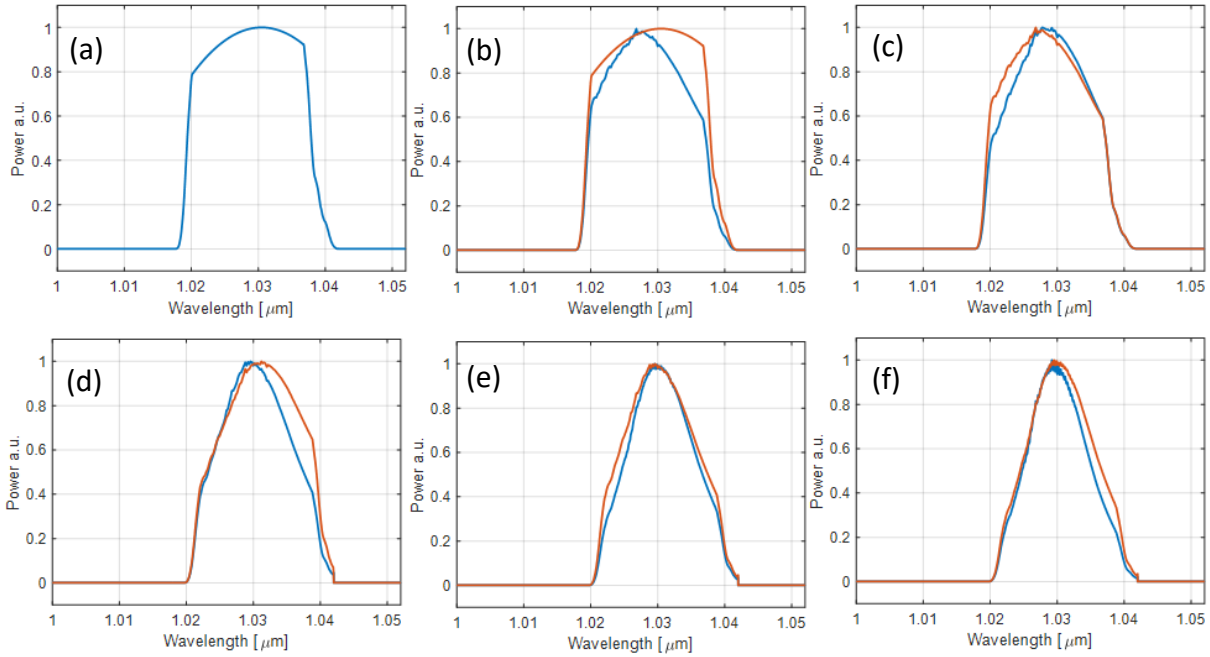

Fig. 2.4 Simulation results of power spectrum evolution in different amplifiers (each amplifier input is shown in red and output is shown in Blue): (a) The filtered optical spectrum of the seeder by the wave-shaper, (b) the first pre-amplifier (Yb-401-PM), (c) the second pre-amplifier (Yb-401-PM), (d) after the AOM and the third pre-amplifier (Yb-401-PM), (e) the double-clad fiber amplifier (25/250 Nufern) and (f) the rod type fiber amplifier

To observe the influence of the spectral shape on the transform-limited pulse, we plot the corresponding temporal pulses after each amplification stage in Fig. 2.5. It can be seen as the spectral amplitude evolves and transforms into a near-parabola due to the gain narrowing, the pedestal in the temporal pulse becomes progressively weaker. Thus, our parabolic filter mentioned above helps to achieve a pedestal-free temporal pulse shape after the compression, which is also observed in our experimental result and will be demonstrated in the next chapter.

Fig. 2.6 (a) depicts the calculated output spectrum and a parabolic fit for comparison after RTA, represented by the blue solid and the red dashed lines, respectively. The stretched pulse in the time domain before the compression is also displayed in Fig 2.6 (b) which has an FWHM of about 600 ps. The effect of gain narrowing across the amplifier chain results in a shortening of the stretched pulse, starting from the CFBG by 1ns to 600 ps at the output of the last amplifier. Fig. 2.6 (c) presents the calculated transform-limited pulse (FWHM of 157 fs) corresponding to this spectrum (with an FWHM of around 10 nm).

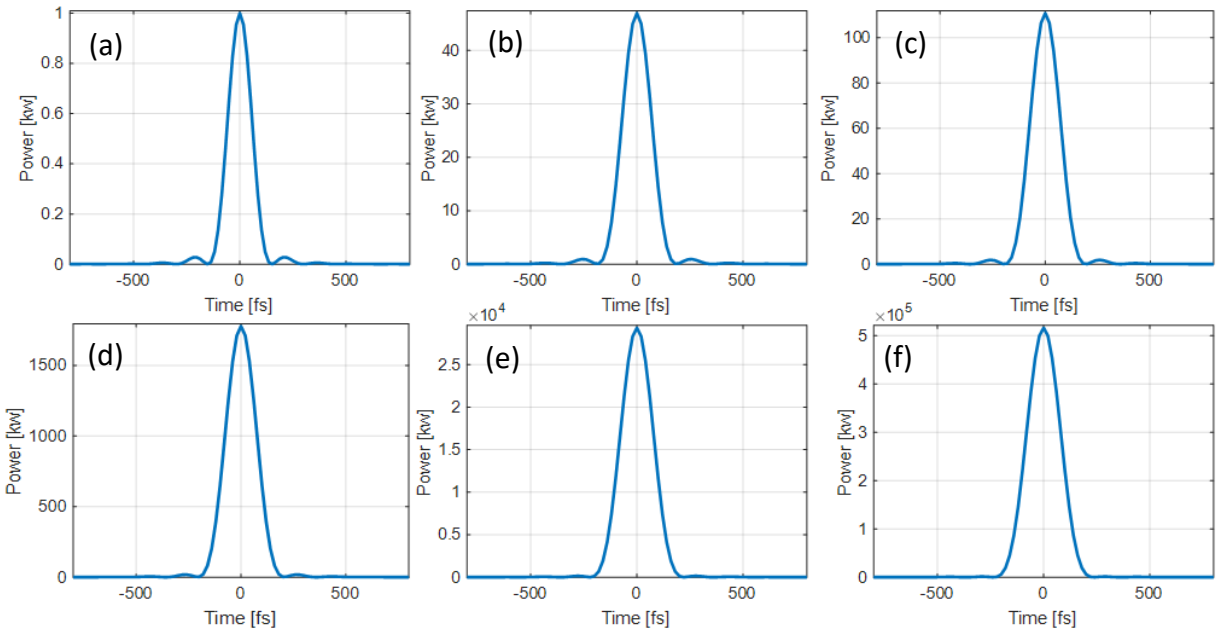

Fig. 2.5 Simulation results: The calculated transform-limited pulse corresponds to the spectral amplitude after (a) the filtering by the wave-shaper, (b) the first pre-amplifier after the wave-shaper (Yb-401-PM), (c) the second pre-amplifier (Yb-401-PM), (d) the AOM plus the third pre-amplifier (Yb-401-PM), (e) the double-clad fiber amplifier (25/250 µm Nufern) and (f) the rod type fiber amplifier

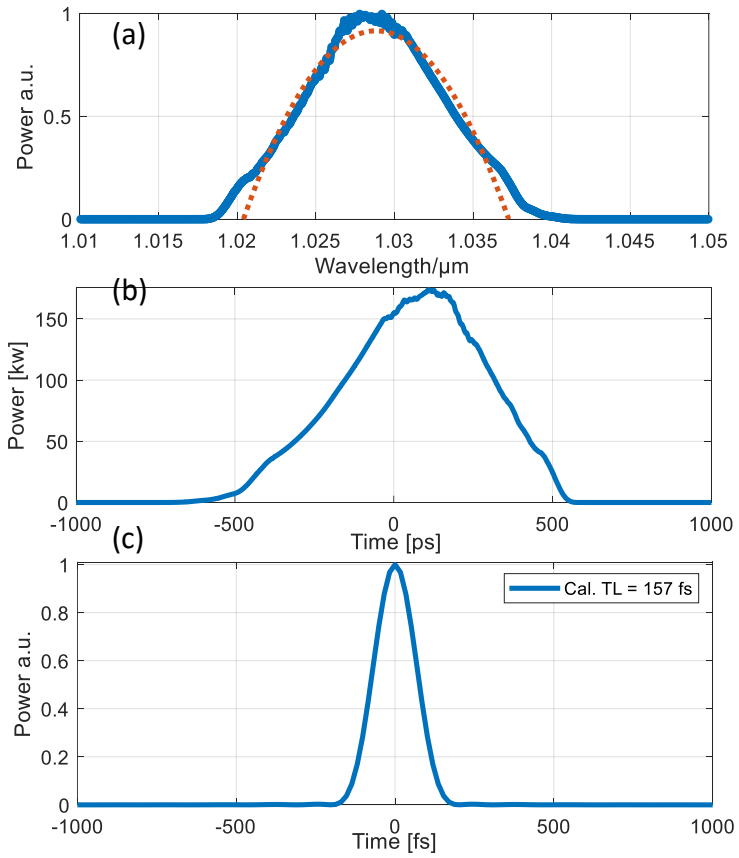

Fig. 2.6 (a) The simulated RTA output spectrum (blue solid line) and the parabolic filter (red dashed line), (b) The uncompressed temporal pulse after the RTA, (c) The calculated transform-limited pulse

2.3 Pulse compression

According to our calculations, the RTA output signal can be amplified to an average power of 100 W and compressed to about 157 fs transform-limited pulses with a Treacy-type compressor we designed with reflection grating pairs. Because there is no pulse compression due to the nonlinear spectral broadening in this compressor, we call it a linear compressor. Fig 2.7 (a) represents our linear compressor. The groove density of the grating is 1760 l/mm, and the Littrow angle at 1030nm is then 65.01°. Fig. 2.7 (b) shows the simulated compressed pulse considering the total dispersion of the system such as the pre-chirp of the oscillator, the dispersion of the fibers and the stretcher, with an incident angle of 69° and a normal grating distance of 273.6 mm. Finally, a pedestal-free pulse with an FWHM of 157 fs is attainable with the mentioned spectral filter in our design.

At the final stage of our system shown in Fig 2.2, using a Herriott cell cavity [6,79] with a controlled number of internal beam reflections, the beam can be propagated and focused in several thin fused silica plates to generate new frequency components by SPM. We call it a nonlinear compressor unit in our system. The final pulses with an FWHM less than 50 fs can be achieved by a combination of chirped mirrors with a certain dispersion in this unit, which is discussed in

chapter 4. The detailed construction of the fiber laser system based on the described design will be explained in the next chapter and the experimental results will be discussed in detail.

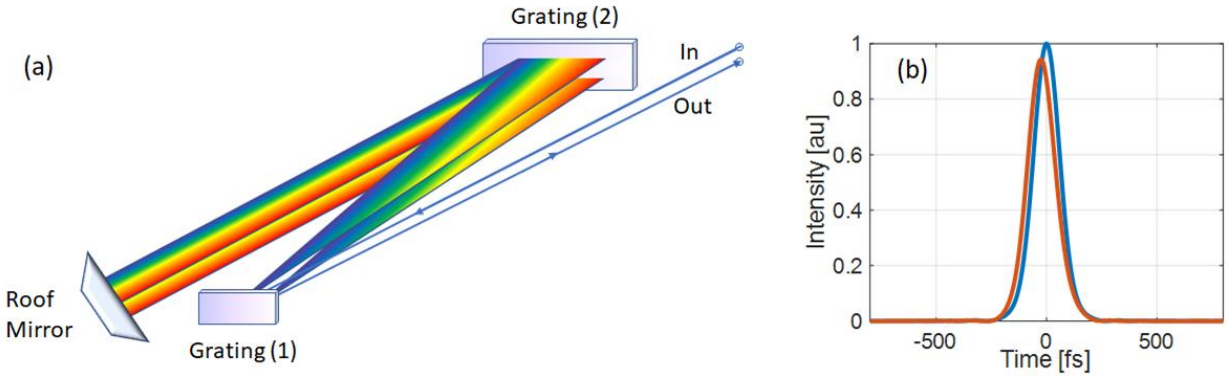

Fig. 2.7 (a) A schematic layout of the Treacy-type compressor, b) The simulated transform-limited pulse (blue) and the best-compressed signal with finding the best parameters for the compressor.

3. Experimental setup and results

In chapter two, we numerically analyzed the temporal and spectral evolution of the pulse propagating through the ultrashort, high repletion rate, and high-power fiber laser front end. In this chapter, we discuss the experimental setup and results for the design shown in Fig. 2.2 in chapter 2. We first describe the construction of a mode-locked fiber oscillator. This is followed by a discussion of pulse stretching with a chirped fiber Bragg grating (CFBG) and spectral amplitude and phase shaping with a Finisar wave shaper. Thereafter, reducing the pulse repetition rate with an AOM and amplifying the signal with preamplifiers to saturate the main amplifier (i.e., the RTA) are explained. The mode matching to the RTA, and the amplified output signal in the time and frequency domains are also discussed. Finally, we evaluate the result of linear pulse compression with reflective gratings and present a pedestal-free pulse with an FWHM of 158 fs as the result of the spectral filtering introduced in chapter two. Nonlinear pulse compression for further pulse shortening is analyzed in detail in the next chapter.

3.1 Construction of an oscillator as the seeder

According to the simulation discussed in chapter two, we need a broad spectrum (at least with an FWHM of 20 nm) for the seed pulse. We thereupon investigate two different configurations of fiber oscillators to find a perfect match with the required seed signal for the system. The first approach is a nonlinear interferometer (NLI) mode-locked fiber oscillator [80,81], followed by a nonlinear amplifier to generate a broad spectrum due to SPM. Fig. 3.1 shows the schematic

diagram and experimental setup of a 40 MHz NLI oscillator we set up for this reason. It consists of PM fibers, which make the intensity of the output pulses less sensitive to ambient temperature and mechanical variations. Accordingly, the output pulses in this configuration have low relative intensity noise [81]. The mode-locking mechanism of the oscillator is based on the accumulation of a differential nonlinear phase shift between the orthogonal polarization modes in the PM fiber segment [81,82]. Two different optical energy ratios are coupled in the fast and slow axes of the PM fiber by a set of wave plates. The polarization mode with higher energy accumulates a larger nonlinear phase shift due to SPM. In parallel, two modes with perpendicular polarization drift-off ($\sim$1 ps/m in the PM980-XP fiber at 1030 nm) in the highly birefringent PM fiber segment of the NLI resonator. A 90-degree rotation of the polarization state of the individual modes helps to compensate for this delay as they are reflected back along the fiber section. The rotation is created using a combination of a 45-degree Faraday rotator and a mirror. The time delay between the two modes is then compensated when they change the propagation axis on their way back through the fiber section. Consequently, two output modes in the opposite direction, interfere at the polarized beam splitter (PBS) with a certain amount of nonlinear phase difference. Since the Kerr effect is very fast, the whole procedure acts like an artificial fast-saturable absorber which is characterized by the transfer function T($\Delta\varphi_{NL}$), and is adjustable by the rotation angles of HWP and QWP1 (Fig 3.1 (a)). An internal compressor helps to control the net dispersion in the oscillator. With a small negative net dispersion, a soliton can be produced under certain conditions of pulse energy and duration, with a small down-chirped pulse which is desirable for nonlinear amplification in an amplifier installed subsequent to the oscillator. A seed pulse with a small negative chirp becomes shorter as it passes through the nonlinear fiber amplifier with positive dispersion. This results in a higher pulse intensity propagating through the fiber, leading to a higher nonlinear spectral broadening.

Port 1 and port 2 in Fig. 3.1 are the reflection and transmission outputs of the loop, respectively. In this oscillator, mode-locking is initially achieved at high pump currents (typically greater than 900 mA, which corresponds to a pump power of 600 mW). Once the laser is mode-locked, the pump current is slowly decreased to achieve single-pulse operation. The 40 MHz NLI oscillator operates in this range with a pump current of 187 mA and an average output power of 5.5 mw for port 2. Figure 3.2 (a) shows the output spectrum of port P2 (transmission) with an FWHM of about 7 nm. Then, the output signal is spectrally broadened due to the SPM in the following amplifier, which is built with a 3.5 m long Ytterbium doped gain fiber with low doping concentration. Fig. 3.2 (b) shows the broadened spectrum with an FWHM of about 20 nm at a pump power of the amplifier of 400 mW. The RF spectrum and the autocorrelation measurements confirm the single pulse operation of this seeder at this pump power level (see Fig. 3.2 (c) and (d)). The output is slightly chirped with a measured pulse duration FWHM of 2.5 ps.

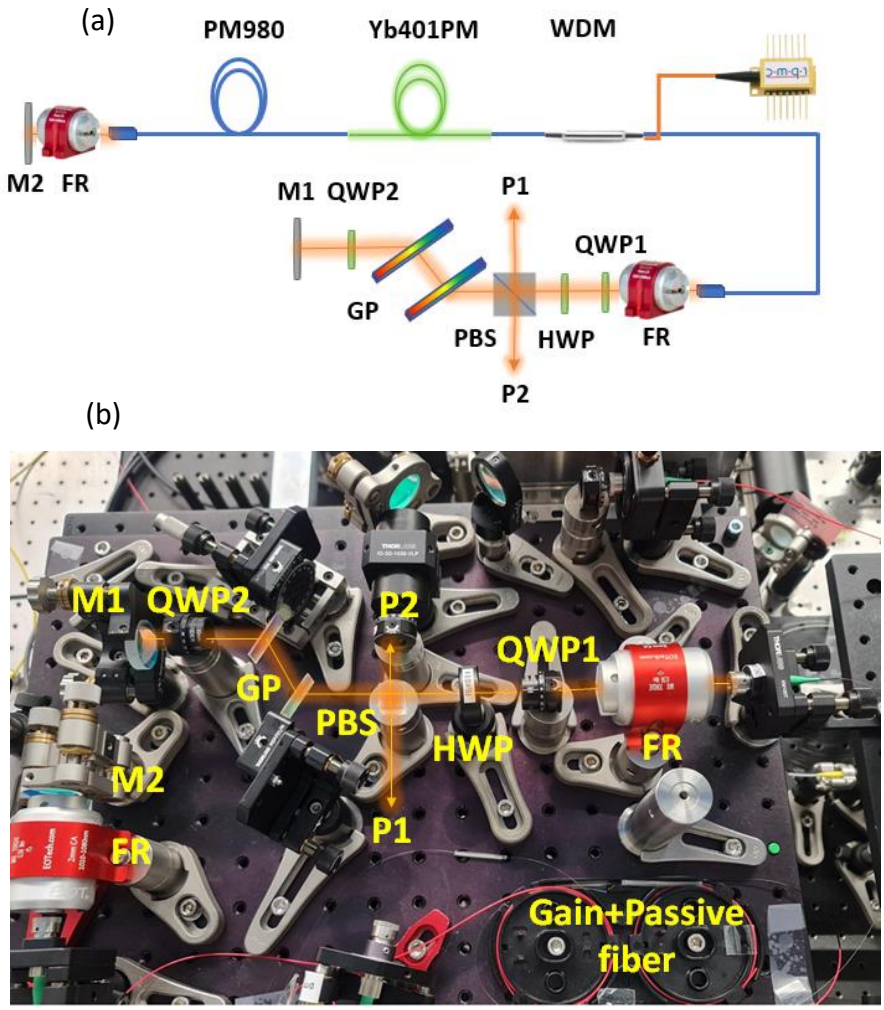

Fig. 3.1 The schematic layout (a) and experimental setup (b) of the NLI oscillator;, wavelength division multiplexer (WDM); M, mirror; PM, polarization maintaining; Yb-401-PM, highly doped PM Yb fiber manufactured by CorActive; QWP, quarter-wave plate; HWP, half-wave plate; FR, Faraday rotator ; PBS, polarization beam splitter; GP, grating pair;

In this linear resonator, mode locking is more sensitive to reflections from various surfaces inside the resonator due to the lack of a reliable isolator (as required in a ring resonator). The threshold for self-start mode-locking occurs at high pump powers in multi-pulse operation. Therefore, if mode locking is lost in the single pulse regime (at low pump power levels) due to environmental fluctuations, it cannot be restored by itself.

The oscillator operates in the soliton regime, then single pulse operation requires a specific pulse energy at a specific net negative dispersion. Constructing this oscillator at a lower repetition rate (longer fiber length) results in a lower output pulse energy and average power (typically 2.5 mW output from the T-port at 20 MHz repetition rate). Because the nonlinearity of a longer fiber segment is higher, and therefore the balance between a given net dispersion and SPM results in

lower intracavity pulse energy at the single-pulse operation. Finally, a seed signal with a very low average power is not able to fully-saturate the consecutive nonlinear preamplifier and suppress the amplified spontaneous emissions (ASE).

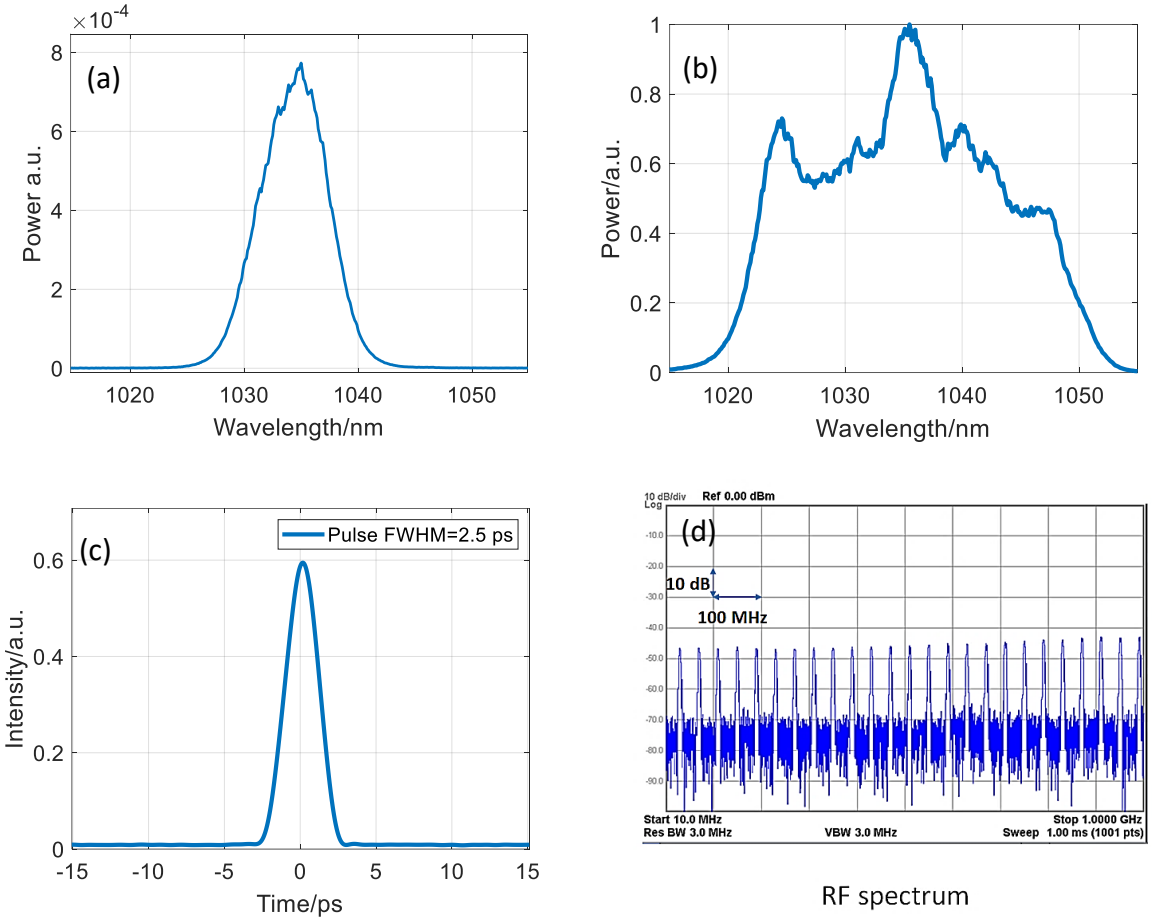

Fig. 3.2 (a) The output spectrum of the transmission port P2, (b) The broadened spectrum due to the SPM in the following amplifier, (c) The pulse duration measured by Pulse-Check autocorrelator, (d) The RF spectrum.

The second approach for constructing a seeder with suitable output parameters for our system is a nonlinear polarization evolution (NPE) mode-locked fiber laser. Figure 3.3 (a) shows the schematic layout of the NPE laser with a mode-locking mechanism based on the intensity-dependent nonlinear change in the polarization state of the pulse inside the non-PM single-mode fibers. We adjust a set of waveplates such that the maximum transmission or the lowest loss occurs for the peak intensity. Therefore, after each roundtrip, the pulse wings get suppressed and

the highest optical intensity is amplified which leads to shortening the pulse duration. It is a ring cavity with an internal isolator that prevents back reflections in the resonator. It can directly generate a broad spectrum of about 20 nm from an output just after the fiber section due to the SPM, so no external nonlinear amplification is required for spectrum broadening. A small positive net dispersion is generated inside the cavity by adjusting an intracavity compressor. It means the pulse gets longer after each roundtrip. On the one hand, the SPM in the passive and active fibers generates new frequency components in the pulse. On the other hand, the positive net group delay dispersion (GDD) spreads the different frequency components under the pulse (lower frequencies come at the beginning and higher frequencies at the end of the pulse) and leads to a prolongation of the pulse after many roundtrips. Incorporating a bandpass filter (10 nm bandwidth with a center wavelength of 1030 nm) into the oscillator cuts off the frequency components in the pulse tails and prevents pulse lengthening after many roundtrips. This configuration generates up-chirped output pulses with a wide output spectrum and reasonable stability. The oscillator is self-mode locked at low pumping levels (around 150 mA corresponds to 70 mW), and single pulse operation is achieved immediately after mode locking by fine-tuning the waveplates. The output pulse duration and spectrum are shown in Fig. 3.3 (c) and (d). The measured pulse width is about 4.9 ps with a positive chirp and the bandwidth at FWHM is 19 nm. The output power is approximately 10mW at a repetition rate of 24MHz. The RF spectrum shown in Fig. 3.3 (b) confirms the single pulse operation of the laser.

A comparison of the two approaches mentioned above shows that the NPE oscillator is more suitable for our system for the following reasons:

- It is a self-mode-locking oscillator, even at low pumping levels, so that mode-locking can be maintained in the presence of ambient noise,

- It has a lower repetition rate, resulting in higher pulse energy for a given average power. This requires a simpler design of the system to achieve a certain output energy,

- And it provides a wide output spectrum without the need for nonlinear spectrum broadening.

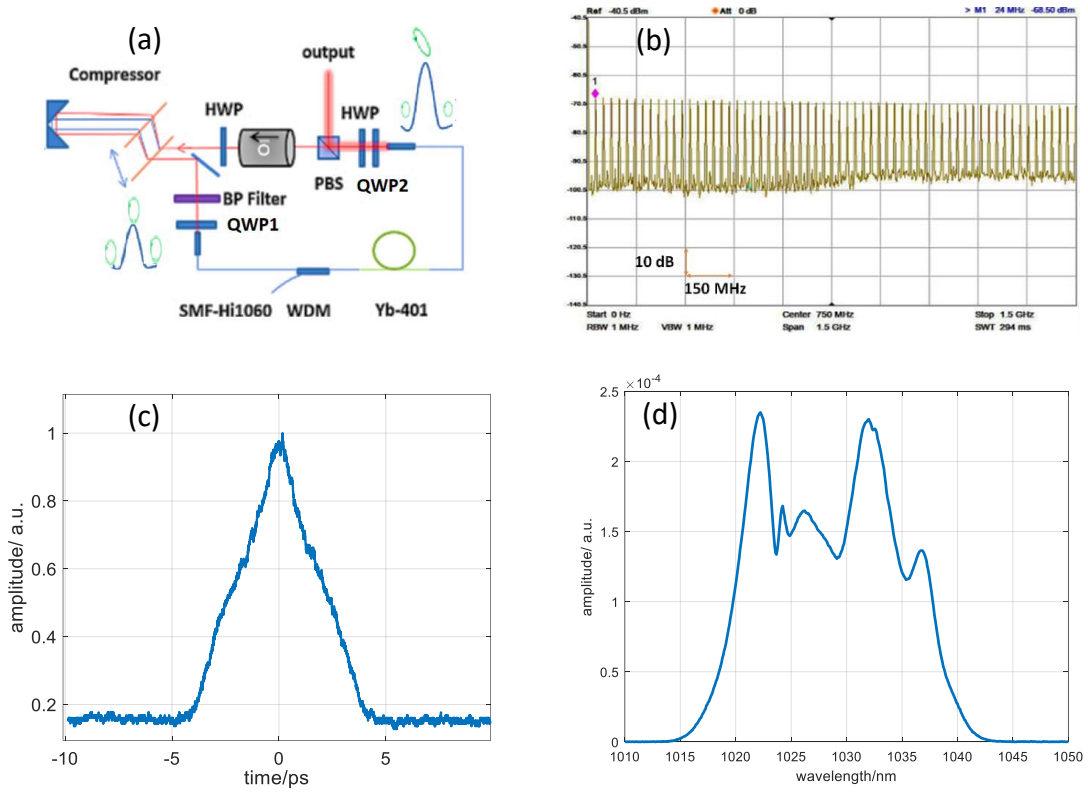

Fig. 3.3 (a) NPE-mode-locked oscillator with a mode-locking mechanism based on the intensity-dependent nonlinear change in the polarization state of the pulse inside the oscillator; For better understanding, a pulse with a hypothetical polarization state before and after propagation through the fibers is shown. The peak of the pulse undergoes a different nonlinear polarization rotation than the tails. (b) The RF spectrum of the single pulse operation of the laser, (c) The measured pulse duration, (d) The output optical spectrum.

3.2 The spectral amplitude and phase shaping

The output of the NPE oscillator described above is boosted by preamplifier 1 (see Fig. 3.4), which consists of a WDM and a highly doped Ytterbium gain fiber (CorActive, Yb-401-PM) to overcome the 40% loss of the stretcher and circulator. An optical isolator should be installed before each amplifier to block backward amplified spontaneous emissions (ASE) and any back reflection to the system. As explained in Chapter 2, the stretcher is a chirped fiber Bragg grating (CFBG) (manufactured by Teraxion) that provides a 22 nm gate for the input spectrum with the specifications given in Table 3.1. The output pulses are stretched to about 1 ns, and have an average power of about 135 mW after the stretcher.

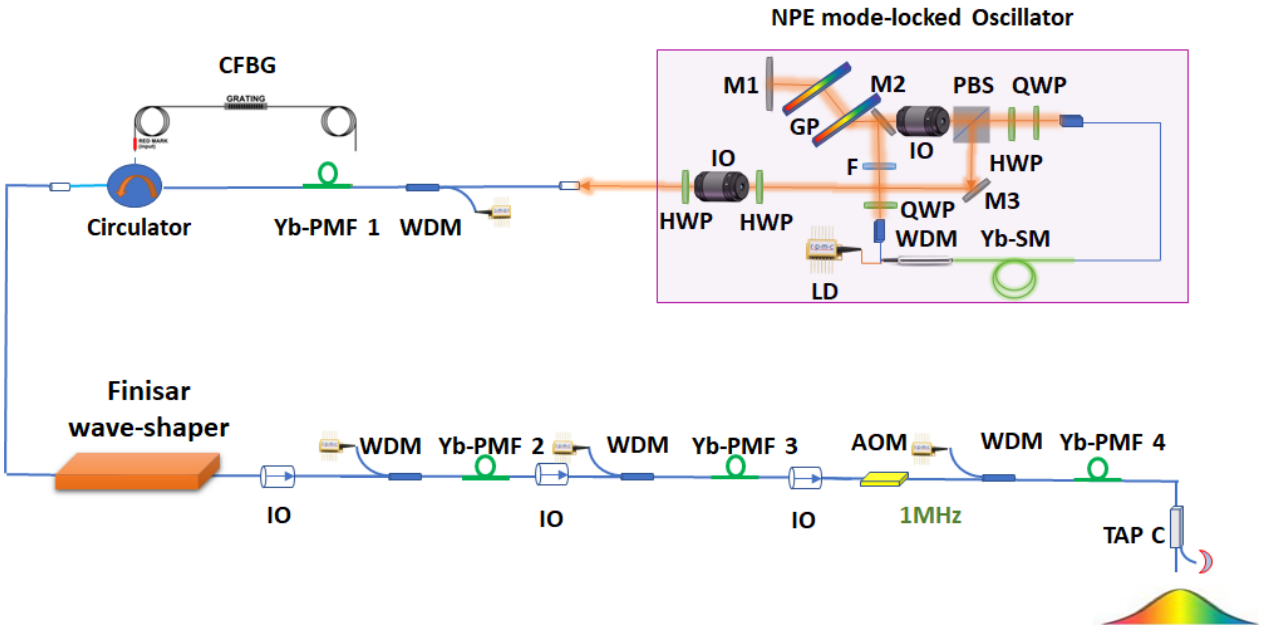

Fig. 3.4 A portion of our design shown in chapter two (Fig. 2.2).

Table 3.1. Specifications of Teraxion's CFBG

Description	Specification	Unit
FBG nominal B2 (GDD)	30.129	ps^2
FBG nominal B3 (TOD)	-0.4	ps^3
FBG nominal B4 (FOD)	0.00875	ps^4
Maximum $\Delta\nu$(nm)*D(ps/nm)	1155	ps
$\Delta\nu$	22	nm
FBG Spectral Shape	Flat top	
Minimum reflectivity over operation bandwidth	>70	%

The spectral amplitude of the signal is manipulated with a wave shaper (Finisar) to remove the modulations and shape the spectrum as described in chapter two. The schematic diagram in Fig. 3.5 shows the principle of the Finisar wave shaper (WS-1000A Programmable Optical Filter, 1µm). It operates on the basis of advanced liquid crystal on silicon (LCoS) technology. The input signal is scattered by a reflection grating and a cylindrical mirror and incidents on the LCoS processor, which consists of a matrix of reflective liquid crystal elements. By applying controlled voltages to these matrix elements, they can add individual phase shifts to the reflected signals and thus manually manipulate the signal components. Since the frequency components are separated on

the LCoS chip, control of a small frequency interval (depending on the resolution of the device) is independent of all others and can be switched or filtered without affecting the other frequency intervals. Consequently, the structure allows arbitrary spectral shaping, attenuation, dispersion, and phase change [78]. The specifications of the device are given in Table 3.2. This device was customized for our wavelength range i.e. for 1020 to 1040 nm. The filter center can be adjusted with a resolution of 0.02 nm, allowing fine control of the spectrum.

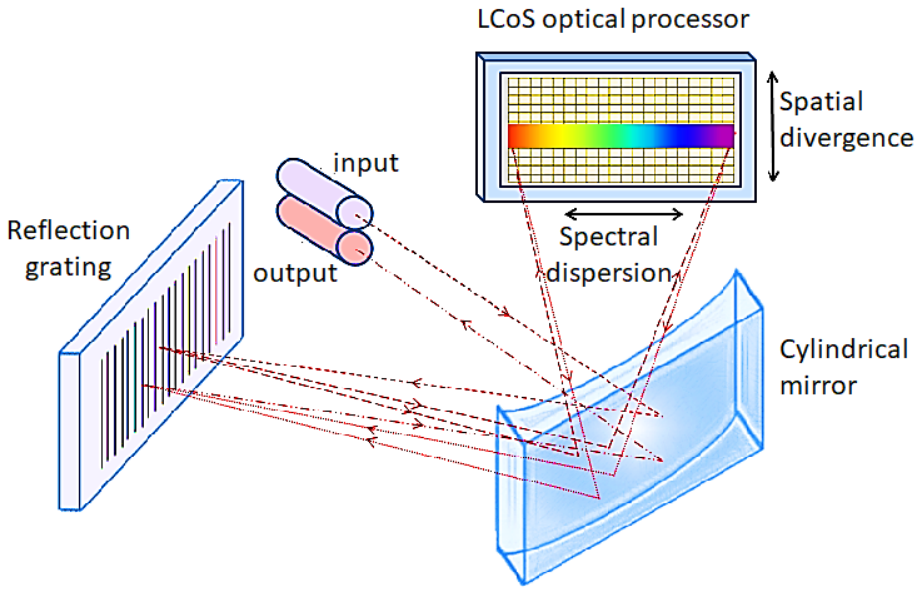

Fig. 3.5 The principle of the Finisar wave shaper family A (www.ii-vi.com) [83].

We create a user-configurable filter (UCF) profile of the parabolic function presented in Equation 2.13 using MATLAB. The file format (*.ucf) is then generated via this code and applied to the waveshaper. The filter profiles are represented in terms of attenuation and phase. Equations 3.1 and 3.2 can be used to convert a filter function ($F(\nu)$) into attenuation ($A(\nu)$) and phase ($\phi(\nu)$):

$$A(\nu) = -20\log_{10}|F(\nu)| \quad (3.1)$$

$$\phi(\nu) = \arg(F(\nu)) \quad (3.2)$$

The factor 20 instead of 10 results from squaring F to convert amplitude coefficients to intensity coefficients. The negative sign results from the fact that attenuation is a measure of loss, not gain, i.e. positive attenuation means a reduction in optical intensity.

Table 3.2 Specifications of the wave shaper 1000A (WS-01000A-Y-S-1-AA-01).

Operating Range	1020 to 1040
Insertion Loss	< 6.5 dB (typ. 5 dB)
Filter Shape	Arbitrary (Attenuation and Phase)
Filter bandwidth	0.05 to 20 nm
Filter Center Setting Resolution	0.02 nm
Filter Center Setting Accuracy	±0.1 nm
Bandwidth Setting Resolution	0.02 nm
Bandwidth Setting Accuracy	±0.1 nm
Group Delay Control Range	- 20 ps to + 20 ps
Settling Time	500 ms
Maximum Total Input Optical Power	500 mW

Figure 3.6 presents the spectrum before and after filtering for $\Delta\nu_{FWHM} = 9\ GHz$, and the central wavelength of 1030 nm. After filtering, there are small amplitude fluctuations related to the slight change of the seed signal resulting from environmental instabilities. This can be suppressed by sealing the seeder and controlling the ambient temperature in this system.

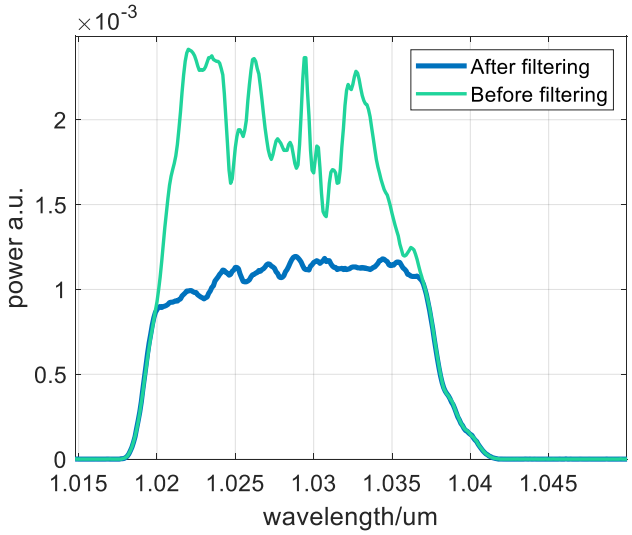

Fig. 3.6 The spectrum before and after filtering by the wave-shaper.

The filtered signal is amplified up to 450 mW by two preamplifier stages to mitigate loss during the pulse-picking process. Then, the pulse repetition rate is reduced from 24 MHz to 1 MHz using a fiber-coupled acoustic-optic modulator (AOM). An AOM is a device that utilizes the acousto-

optical effect (an interaction of light and sound waves) to deflect a light beam as illustrated in Fig. 3.7. [84,85].

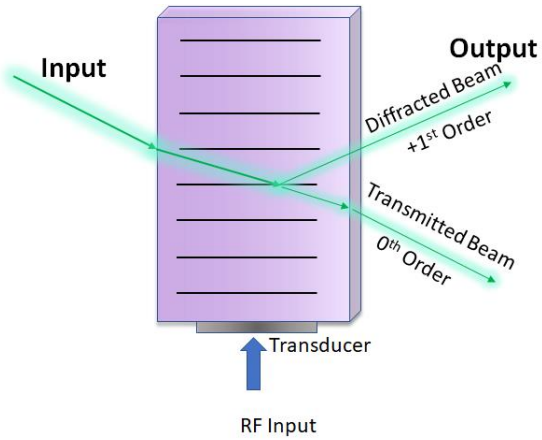

Fig. 3.7 Acousto-optic effect applied in an AOM for pulse picking.

An RF wave is applied to the transducer, resulting in an ultrasonic acoustic wave that travels through the AOM. The acoustic wave modulates the refractive index of the AOM crystal, creating a running optical grating. When an optical beam is coupled into the AOM at the Bragg angle, it can be diffracted into the $+1^{st}$ order very efficiently. The $+1^{st}$ order is used as the AOM output because a very high contrast ratio (i.e. ratio between light transmission in the ON and OFF-state), can be achieved. The diffraction power is zero when the RF wave is completely off. This outweighs the disadvantage that less than 100% (around 50% for the employed AOM manufactured by G&H) of light is diffracted into the $+1^{st}$ order in the ON state. By synchronizing the modulated RF amplitude with the pulse arrival times, laser pulses can be transmitted with a specific pattern and repetition rate.

After reducing the repetition rate to 1 MHz, the average signal power is enhanced to 300 mW by installing the fourth preamplifier (gain fiber: Yb-401-PM), ensuring full saturation of the downstream LMA amplifier (25/250µm large mode area (LMA) Yb-doped fiber). A tap coupler with a 99:1 split ratio is spliced upstream of the LMA preamplifier to monitor signal specifications through the 1% output coupler. The pulse spectrum of the branch output is shown in Fig. 3.8. For comparison, we also show the simulated spectrum presented in the last chapter. As can be seen in this figure, there is a good agreement between the experiment and the simulation result.

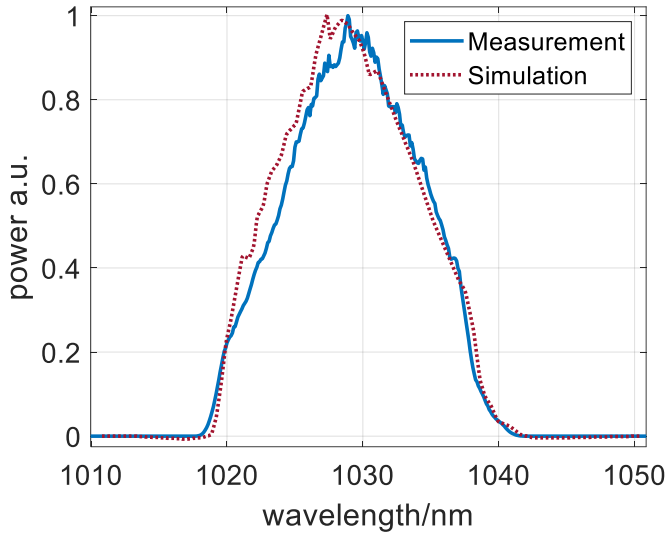

Fig. 3.8 The experimental and simulated output spectrum of the signal after preamplifier 4 (tap output).

3.3 The large mode area (LMA) and rod-type fiber amplifier

The output signal introduced in the previous section is coupled into the LMA preamplifier after passing through an isolator (Fig. 3.9). The output fiber of the isolator is a small core single-mode PM-fiber with a core diameter of 5.5 µm, which has to be spliced to a passive LMA fiber with a core diameter of 25 µm as the input of the pump combiner. To avoid the induction of higher order modes (HOM) at the splice junction between two fibers with different cores, we need to taper the LMA fiber and then splice it to the one with the small core. The tapered fiber changes the beam geometry (such as the beam diameter and the output angle) as the numerical aperture of the LMA fiber is gradually converted to that of the small core fiber over the tapered length. The higher-order modes in a moderately tapered fiber region are guided quite weakly or disappear completely so that almost only light in the fundamental mode of the fiber survives [86,87]. We use a Fujikura FSM-100 series splicing machine to taper the LMA fiber. Furthermore, to suppress

HOM in beam propagation along the LMA fiber, we wrap it to a diameter of 60 mm. Figure 3.10 shows a typical output spectrum after the LMA amplifier. Up to 6 W output power can be achieved from this amplifier using a high-power multi-mode (MM) pump diode (Oclaro, BMU25A ,25 W), which can fully saturate the main amplifier i.e. the rod-type amplifier (RTA). LMA-amplifier is forwardly pumped and the residual pump is reflected into a beam blocker using a dichroic mirror.

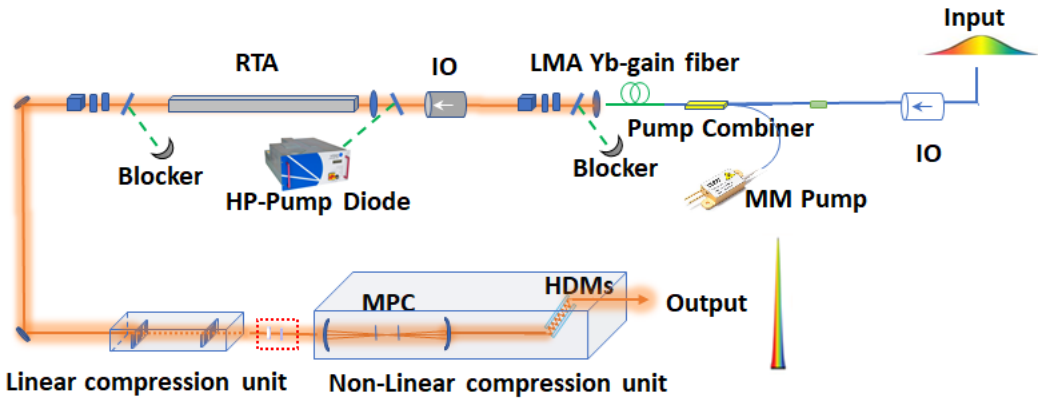

Fig. 3.9 The second part of the schematic layout of the setup.

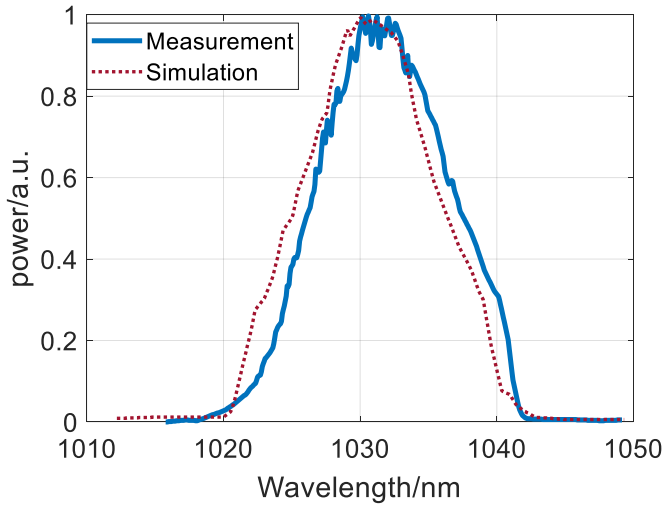

Fig. 3.10 The experimental and simulated power spectrum of the LMA amplifier.

A free space high-power optical isolator is installed before RTA to block the backward ASE and any back reflections. Then the signal is coupled into the RTA utilizing two adjusting mirrors and a coupling lens. P-polarization is selected for the input by a half-wave plate (HWP) and a polarized beam splitter (PBS) as recommended by RTA's manufacturer (The typical polarization extinction ratio (PER) of the RTA is 15 dB). The beam profile at an optimal mode coupling is shown in Fig. 3.11.

RTA is pumped forwardly i.e. the signal and the pump co-propagate into the amplifier. An industrial high-power (HP) diode laser (LaserLine LDM-500) is used for pumping the amplifier. The temperature of the HP laser diode must be appropriately adjusted to shift the central wavelength to the absorption peak of the gain i.e. at 976nm. For this reason, the temperature of the external cooling is set at 19 degrees. Then the temperature of the laser diode is gradually increased depending on the pump power. Finally, an optimal setting is made when the center wavelength of the pump is set to 976 nm at a laser power of 100 W.

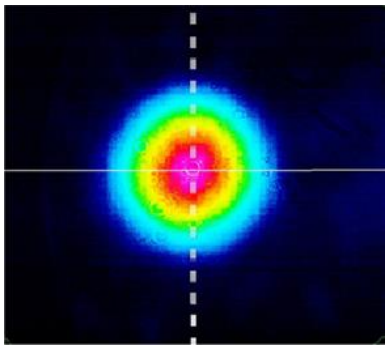

Fig. 3.11 The output beam profile after the mode coupling into the RTA.

Figure 3.12 shows the laser output power versus pump current at the signal power of 5 W. Based on the manufacturer's recommendations for the safe operation of the RTA, we do not increase the output power beyond 100 W. The spectrum and pulse duration of the amplified signal are presented in Figures 3.12 (a) and (b). As one can see, the shape of the spectrum is close to a parabolic fit, resulting in an effective suppression of the pedestal in the temporal signal after the linear compressor, as will be shown in the next section. The bandwidth of the RTA output signal is measured to be about 10 nm, and the pulse duration is approximately 620 ps, which agrees with the values of the simulation (i.e. 10 nm and 600 ps.).

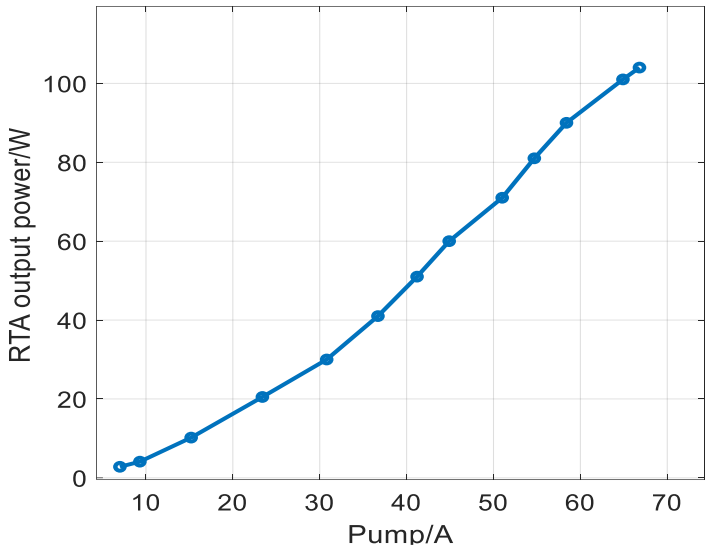

Fig. 3.12 The average output power of the RTA (The repetition rate=1 MHz; The signal power=5 W).

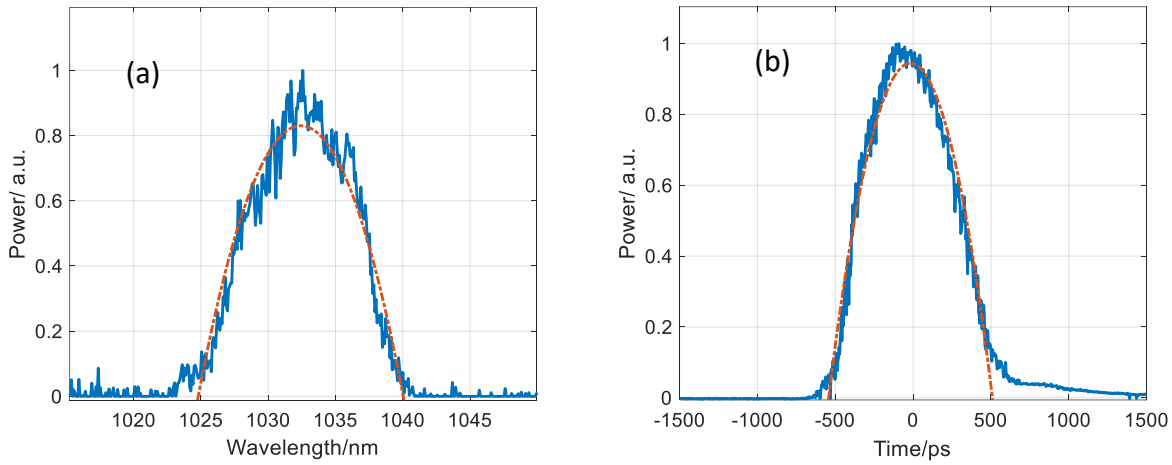

Fig. 3.13 (a) The output power spectrum and (b) the pulse duration after RTA, red dashed curves are parabolic fitting curves.

3.4 Linear pulse compression by a Treacy-type compressor

The compressor parameters calculated for compensation of accumulated dispersion in the system are shown in Fig. 3.14. We used a pair of Plymouth reflection gratings with a groove density of 1760 l/mm and a Littrow angle of 65.01° at 1030 nm. The entrance angle of incidence (AOI) and normal spacing (NS) of the grating are shown in Fig. 3.14 (AOI:69˚ and NS:273.6 mm). These gratings are optimized for the S-polarized input beam. Therefore, the polarization of the RTA output is first corrected to S-polarization by a combination of a quarter-wave plate (QWP), a half-wave plate (HWP), a PBS, and a second HWP.

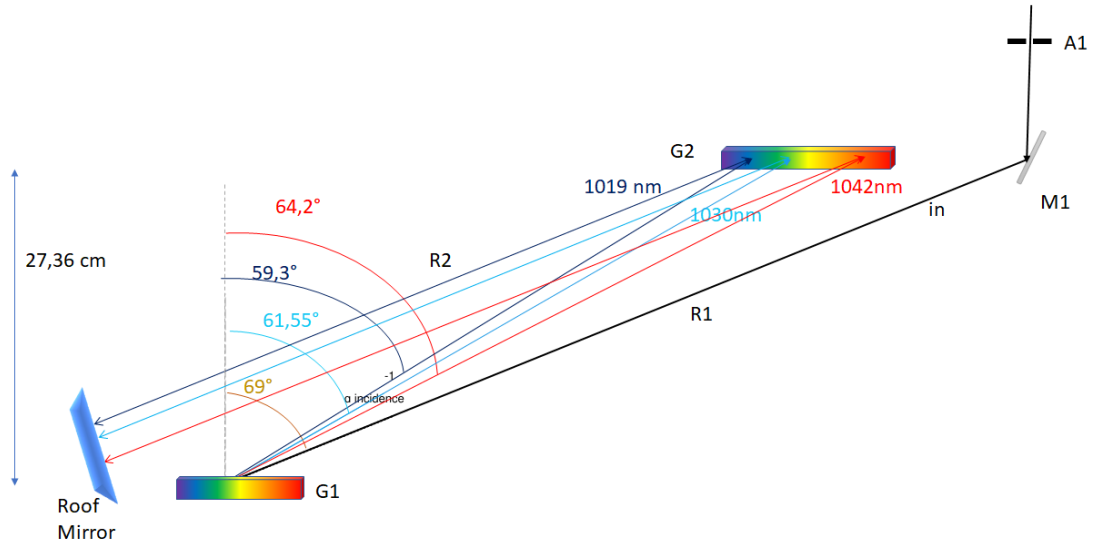

Fig. 3.14 A schematics of the Treacy compressor.

Figure 3.15 (a) shows an optimally compressed signal when no spectral shaping is performed. A strong pedestal can be seen in the pulse, which is due to the uncompensated third and fourth-order dispersion (TOD and FOD) in addition to the nonlinear phase shift. We perfectly suppress this pedestal by using our previously discussed near-parabolic spectral filter. A pedestal-free near transform-limited pulse is achieved which is shown in Fig. 3.15 (b). The measured pulse duration is about 158 fs. It is close to the calculated transformation-limited pulse duration of the output spectrum, which is about 152 fs, as well as to the simulated result of 157 fs (section 2.2 Fig. 2.6). Thus, we can manually control the spectral amplitude and phase of the pulse with the Wave Shaper and investigate interesting effects on the output parameters. The linear compression unit produces a 13% loss in the system. The average output power is 78 W and is fed to the nonlinear pulse compression unit explained in the next chapter.

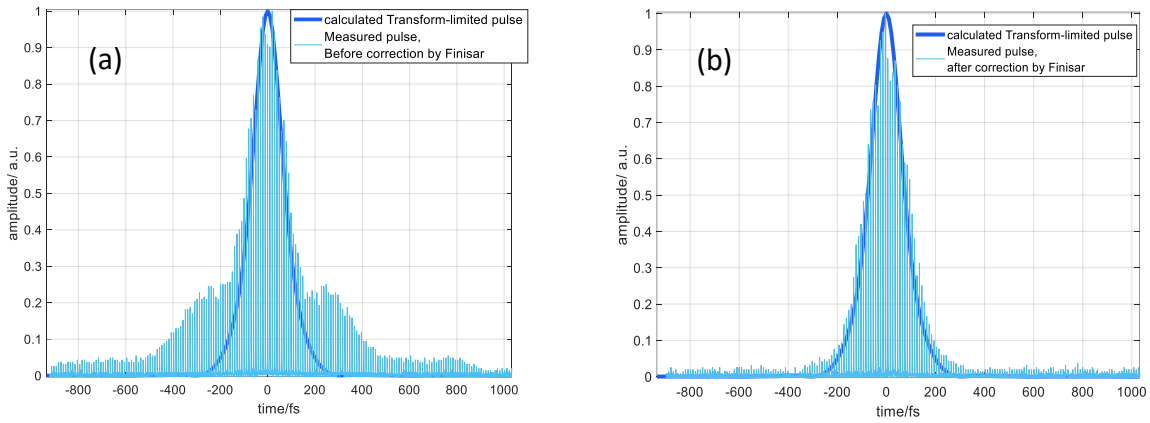

Fig. 3.15 The Treacy compressor's output: (a) with no spectrum and phase manipulation, (b) with the introduced parabolic spectrum filter and a small additional phase using the Finisar wave-shaper.

4. Nonlinear post compression

4.1 Introduction

In chapter three, we demonstrated a nearly transform-limited output pulse with FWHM of 158 fs as a result of the controlled spectral phase and amplitude and precisely aligned Treacy compressor in our system. However, a shorter pulse duration is required to increase peak power for an efficient high harmonic generation and improved temporal resolution in pump-probe experiments. Direct achievement of a pulse duration of lower than 100 fs is limited in Yb-doped fiber amplifier systems due to the gain bandwidths of the laser media and the gain narrowing effect in amplifiers [88]. One way to achieve shorter pulse durations is nonlinear pulse compression, which can be applied to high-power laser systems. As mentioned earlier, a laser pulse is spectrally broadened due to SPM when it propagates through a $\chi^{(3)}$ nonlinear medium. A temporally compressed pulse can be obtained after removing the chirp of the spectrally broadened pulse with a compressor made by grating pairs or dispersive mirrors. The spatial effect of the Kerr effect results in self-focusing, which can lead to the degradation of beam quality. In addition, devastating self-focusing can occur if the peak power exceeds a damage threshold of the material. Therefore, the nonlinear medium for spectral broadening should be selected appropriately for different pulse peak powers.

Various techniques have been used for the nonlinear spectral broadening, such as propagation of ultrashort pulses through solid core fibers [89], hollow-core photonic crystal fibers [90], gas-filled capillaries [91], bulk media, and multi-pass cells [88]. Solid core fibers, most prominently made of fused silica, are limited by the critical self-focusing threshold that occurs at peak powers of ~4 MW for linearly polarized light at 1 μm wavelength. The highest average power reported to date for spectrally broadened pulses with a dielectric nonlinear medium is 250 W [89]. Noble gases with nearly three orders of magnitude higher self-focusing thresholds are a suitable solution for pulses with higher pulse energies. Therefore, for input pulse energies greater than 100 μJ, gas-filled hollow core capillaries are generally used because they have practical dimensions and much lower nonlinearities [34,92,93].

However, for a long time, a gap remained for the medium energies from 10 to 100 µJ, where a standard glass fiber is damaged and the necessary small diameters of the capillaries lead to unacceptably high losses. The invention of Kagome photonic crystal fibers with significantly lower propagation losses resolved this problem [94–96]. They are now routinely used for nonlinear compression experiments with pulse energies in the mentioned range [94,97–99].

As an alternative, nonlinear spectral broadening in a single bulk dielectric has been proposed instead of waveguides for pulse compression with peak powers above the threshold for critical self-focusing [100]. In this case, the diameter and divergence of the input beam as well as the length of the nonlinear medium must be precisely tuned to avoid critical self-focusing. However, beam quality degradation and spatially inhomogeneous spectral broadening cannot be avoided with this method due to the spatial Kerr effect. This approach requires spatial filtering, resulting in limited compression efficiency (∼60%), which decreases even further as peak power increases [101,102].

Jan Schulte and others reported in 2016 on a bulk dielectric-based method for nonlinear pulse compression in the 10-100 μJ pulse energy range that mitigates the disadvantages of spectral broadening in a single bulk medium and offers unprecedented robustness and scalability of average power [88]. Laser pulses are repeatedly propagated through a bulk nonlinear medium using a multi-pass cell (MPC). Pulses accumulate a B integral $\ll \pi$ each time they pass through the nonlinear medium. In this procedure, pulses with peak powers above the critical self-focusing threshold can be spectrally broadened and the degradation of beam quality due to the thin thickness of the medium is alleviated. A considerable spectral broadening can be achieved with this technique [103,104]. This approach is limited only by laser-induced damage of the nonlinear medium, the MPC optics, and their coatings. By employing anti-reflective (AR) coated fused silica as nonlinear plates and dielectric coated mirrors as optics, this system can be used in ultrafast laser systems with average power up to the kW range. These advantageous properties make MPCs very attractive not only for scientific applications but also for commercial laser systems and devices where reliability is of the greatest importance [104].

4.2 Hybrid multi-pass multi-plate spectral broadening

The inventions of MPC spectral broadening [6,88,105] and multi-plate continuum generation [106] result in much better spatial homogeneity of the broadband spectra. Just recently, Marcus Seidel and others have presented a combination of both approaches in a single, compact spectral broadening stage [79] with compression factors of more than 30. This compact compression technique is an attractive method for generating sub-50 fs pulses from a high-power laser. We have incorporated this compact, low-cost scheme in our system as a nonlinear pulse compression unit which does not require gas-filled chambers. Figure 4.1 presents a general layout of this scheme consisting of a telescope (a), a multiplate MPC (b) and a post compressor (c).

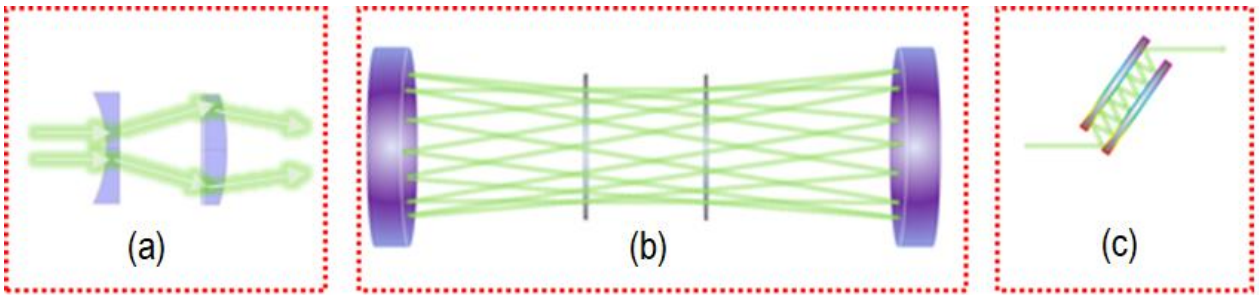

Fig. 4.1 A layout of the implementation of the multi-pass multi-plate cell for spectral broadening and the post-compression. (a) mode-matching; (b) spectral broadening in a nonlinear medium inside the MPC; (c) temporal compression using chirped mirrors or transmission gratings.

The Herriott-type MPC consists of two identical concave mirrors aligned as an optical cavity to form transverse eigenmodes and preserve the q-parameter of a Gaussian beam matched to the MPC eigenmode with the help of a telescope [107,108]. The beam is then coupled off-axis into the MPC via a small pick-off mirror or a holey MPC mirror [6,109]. After a certain number of round trips, the spectrally broadened output beam is decoupled out of the cell [110]. The beam must then be collimated and compressed using a grating pair or a chirped mirror compressor. Several propagations through regions of nonlinearity, combined with appropriate refocusing via the cell mirrors, result in a redistribution of the spatial beam content from focus to focus and allow for both large broadening factors and high spatial-spectral homogeneity [111].

The B integral is a measure of spectral broadening [111,112] for the propagation of a Gaussian beam in a symmetric MPC with a negligible loss and dispersion, and for one pass is given by:

$$B = 4\pi \frac{n_2 P}{\lambda^2 z_R} \int_{d_K}^{d_K + l_K} \left(1 + \frac{z^2}{z_R^2}\right)^{-1} dz \qquad (1)$$

Where d_K is the distance from the cell center to the Kerr medium, l_K is the length of the Kerr medium, z_R is the Rayleigh length, P is the peak power and n_2 is the medium non-linear refractive

index. The spectral broadening factor (b) for N round trips ($2N$ passes) through the MPC is equal to the root mean square (rms) bandwidth ratio $\frac{\Delta w_{out}}{\Delta w_{in}}$ and can be calculated as [112,113]:

$$b = \frac{\Delta w_{out}}{\Delta w_{in}} = (1 + (0.44B)^2)^{1/2}, \quad (2)$$

Two important quantities which typically limit the maximum pulse energy for an MPC are the laser-induced damage threshold (LIDT) of the MPC mirrors (expressed by the fluence F_m) and the focus peak intensity I_0 to avoid the electrical breakdown in the air or gas-filled MPC [111]:

$$F_m = \frac{2E}{R\lambda}\sqrt{\frac{2-C}{C}}, \quad (3)$$

$$I_0 = \frac{4P}{R\lambda}\frac{1}{\sqrt{C(2-C)}}, \quad (4)$$

$$C = \frac{L}{R} = 1 - \cos\left(\frac{\xi}{2}\right), \quad (5)$$

With E and P stand for energy and peak power of the pulse, L and R are the MPC mirror spacing and the radius of curvature (RoC), respectively. If the pulse is coupled in and out of the cell at the same position after N round trips i.e., the re-entrant condition is satisfied, then the angle advance ξ is defined as [111]:

$$\xi = \frac{2\pi K}{N}, \quad \text{where } K = 1, \dots, N-1 \quad (7)$$

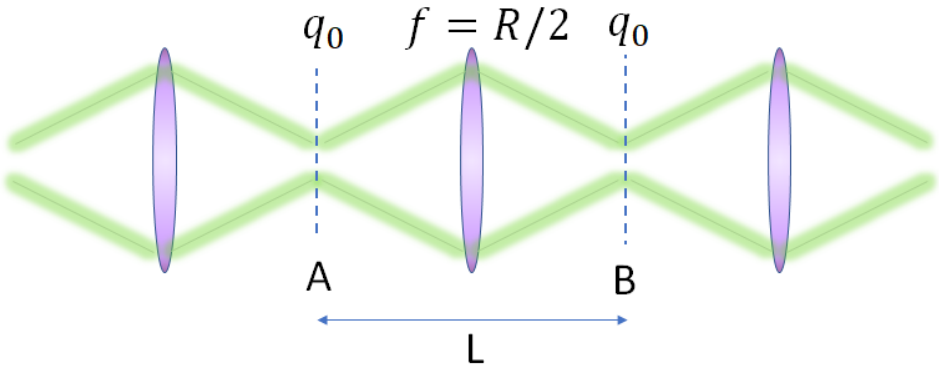

Fig. 4.2 An equivalent resonator for a Herriott-type cell with a periodic sequence of lenses. L, the length of the mode-matched cell; f= R/2, The lenses' focal length; R, The radius of curvature.

As mentioned earlier, MPCs for spectral broadening are usually operated in a q-preserving configuration by matching the laser beam to the spatial resonator mode, thus satisfying the same stability criteria as for an optical resonator. Therefore, an equivalent resonator with a periodic sequence of lenses can be define for the mode-matched MPC as Fig. 4.2. The q-parameter has to

be identical at the boundaries (i.e. $q = q_0$ at A, B). The relation for the q-parameter of a Gaussian beam after a single pass in MPC can be explained as [79]:

$$q = \frac{\widetilde{M}_{MPC(1,1)}\, q + \widetilde{M}_{MPC(1,2)}}{\widetilde{M}_{MPC(2,1)} q + \widetilde{M}_{MPC(2,2)}} \qquad (8)$$

Where $\widetilde{M}_{MPC}^{lin} = \tilde{L}(f)\tilde{P}(d)$ (9)

$\tilde{L}$ is the ABCD matrix of the thin lens, f, the focal length of the MPC mirror, $\tilde{P}$, the ABCD matrix of the propagation, and d, the cell length. The beam radius of curvature (RoC) at MPC mirror planes has to be $2f$ to preserve the q-parameter after each round trip into the MPC [79,107,111,114]. Equation (9) explains an empty MPC with no nonlinear medium, so it is referred as linear mode-matching [79]. For nonlinear mode-matching, the Kerr lenses must be considered. Thus, the ABCD matrix changes to [79]:

$$\widetilde{M}_{MPC}^{nl} = \tilde{L}(f)\tilde{P}(d_{MK})\left[\widetilde{K}(n,l,\gamma)\tilde{P}(d_K)\right]^{i-1} \widetilde{K}(n,l,\gamma)\tilde{P}(d_{MK}), \qquad (10)$$

where d_{MK} denotes the distance from the MPC mirror to the Kerr medium, $\widetilde{K}$ is the Kerr lens ABCD matrix [115] depending on the refractive index n, the nonlinear plate length l, and the parameter γ, d_K is the plate spacing and i the number of Kerr media. Using the above equations, one can simulate the cell length, and the position of the plates based on their thicknesses and also beam waist and the position of the focal plane in MPC to obtain a certain amount of B-integral. We simulate our dual-plate MPC using a code written by Marcus Seidel and others based on the equations discussed [79] to find appropriate parameters for the nonlinear compression of our near-transform-limited 158 fs pulse, which is explained in the next section.

4.3 Simulation for a dual-plate MPC for nonlinear compression

A dual-plate multi-pass cell is designed through two curved mirrors with a curvature radius of 200 mm and two internal fused silica plates with a thickness of 1 mm. We measured the M^2 factor of the input beam via an M^2-measurement device (Spiricon-M^2-200s). As is shown in figure 4.3 it has a near-diffraction-limited profile with the beam quality of $M_x^2 \times M_y^2 : 1.10 \times 1.06$.

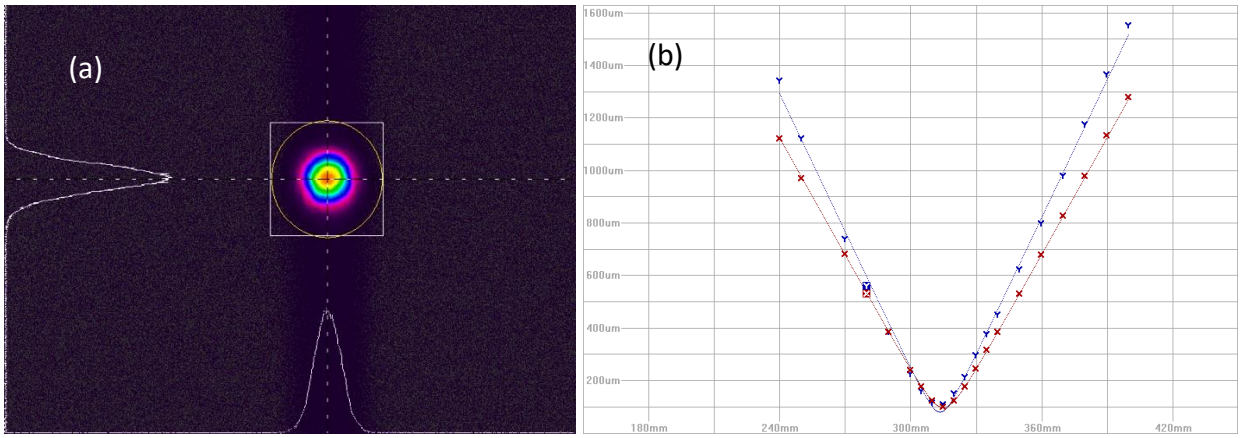

Fig. 4.3 The MPC input beam profile (a) and the M^2 measurement result (b).

Using the equations mentioned in the last section, we calculate the beam radius and the inverse RoC for an MPC with N=16 (16 round trips), which yields optimal parameters for maximum spectral broadening without damaging the surfaces. Figure 4.4 demonstrates the possible K solutions for N=16 and the B integral in a single pass. The higher B-integral results for K=13, which corresponds to a cell length of 366 mm. Calculations show that the beam radius and thereby the beam intensity on the curved mirrors is lower for K=13 compared to the other solutions. As can be seen, K=3 also gives a higher B integral similar to K=13, but in this case, the intensity on the mirrors is almost 10 times higher, which increases the risks of damage, besides it is practically impossible. The distance between the mirrors is too small (33.7 mm) and there is not enough space to mount plates and measure the size of the beam waist with a camera.

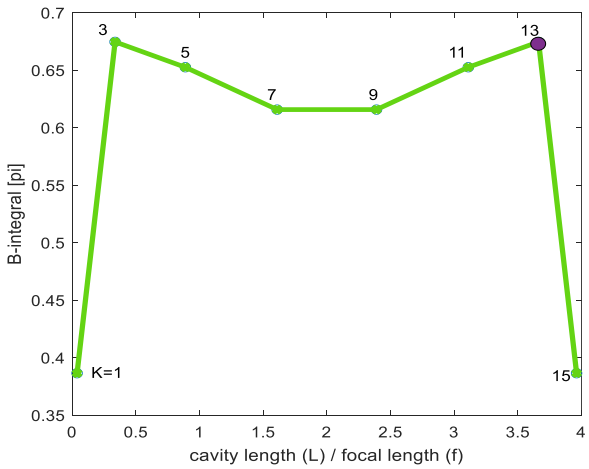

Fig. 4.4 The calculated B-integral for N=16 round trips in a cell consisting of mirrors with RoC=200 mm and two inner plates with a thickness of 1 mm. The indicated point corresponds to K=13.

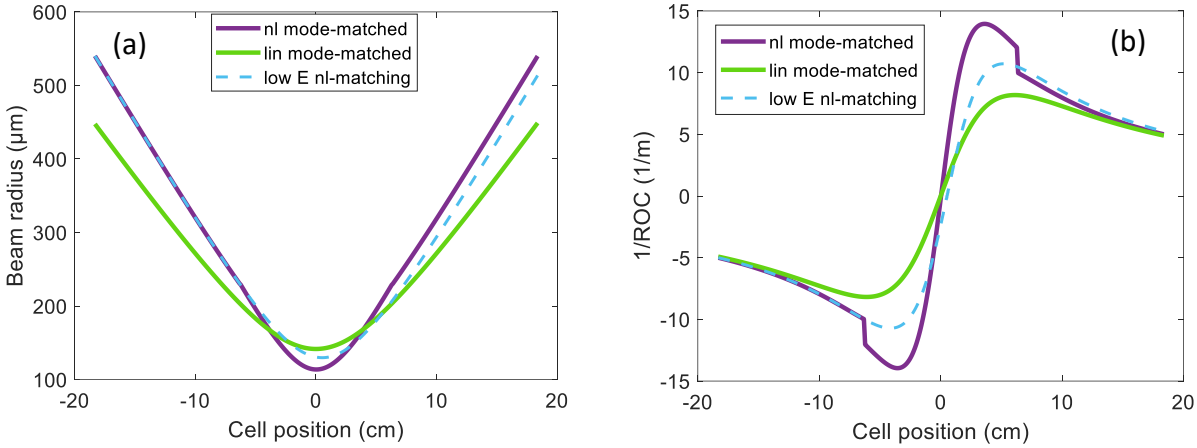

Fig. 4.5 (a) Beam radius and (b) inverse radius of curvature (1/RoC) for a mode-matched MPC without nonlinear (nl) media (green solid lines) and with two Kerr lenses (purple solid lines). The blue dashed lines show the result for nonlinear mode matching at weak power (negligible Kerr-lensing), and is used for MPC alignment.

Fig. 4.5 shows the beam parameters in an MPC considering an ABCD matrix calculation in one pass, with linear mode matching for an empty cell (green solid lines) and nonlinear mode matching (purple solid lines) considering the lensing of two Kerr media. In both cases, the radii of curvature at the mirrors are identical and coincide with the RoC of the mirrors. Apart from these points, the q parameters vary greatly within the MPC. The Kerr plates are symmetrically placed in the center of the cell and are separated by 12.5 cm. The linear mode-matched beam is smaller than the nonlinear beam at the mirrors. However, the focal spot size of the linear mode-matched cell is larger than that of the nonlinear one. Figure 4.5 (b) shows a significant change in the slope of RoC at the Kerr medium positions. The nonlinear mode matching at low input powers is also shown by blue dashed lines, which help us to align the MPC. Figures 4.6 and 4.7 show a schematic picture of the designed MPC and the beam pattern at the MPC mirrors for the cases K=13 and 15, respectively. The angles ξ between consecutive reflections are shown at the first mirror in both cases.

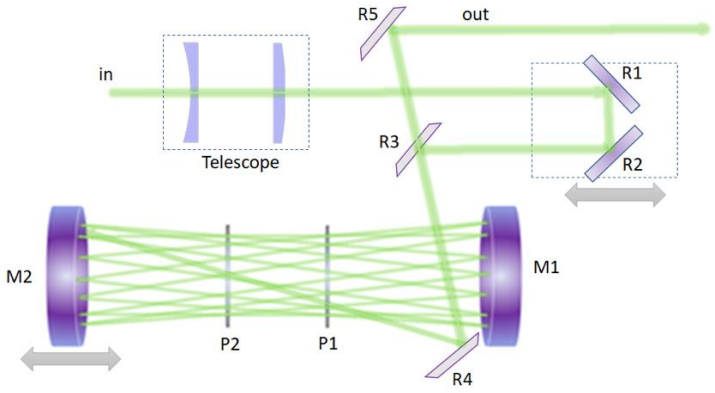

Fig. 4.6 Spectral broadening with a dual-plate MPC, M, MPC curved mirror; R, flat reflection mirror; P, plate.

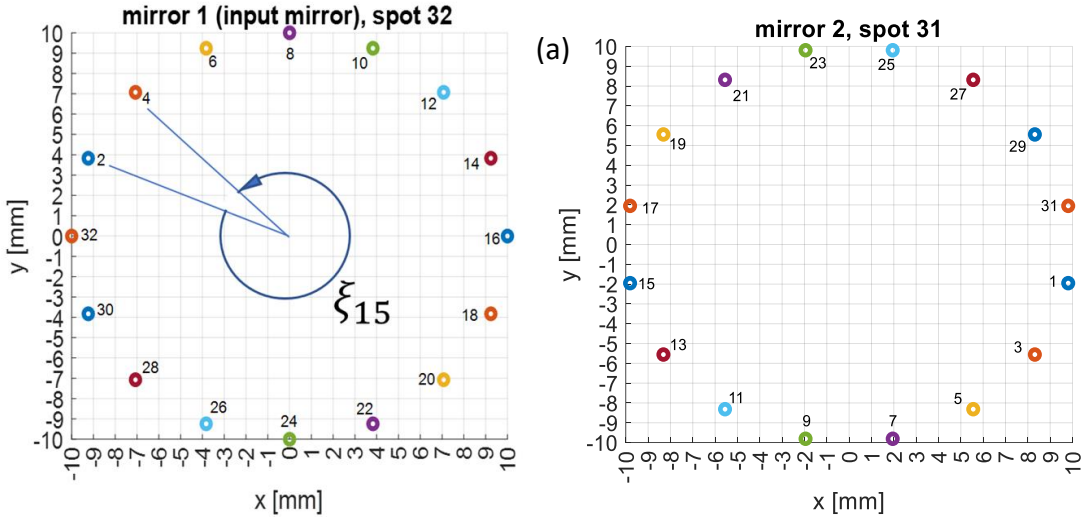

N=16, K=15

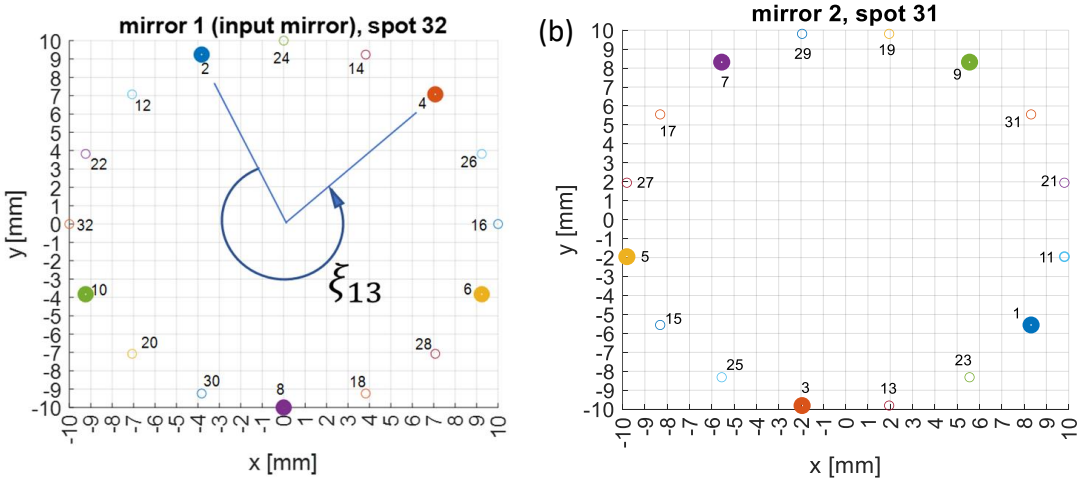

N=16, K=13

Fig. 4.7 Beam pattern evolution for (a)K=13 and (b) K=15 (N=16).

4.4 Experimental results

We employ two curved mirrors with an RoC of 200 mm with the high reflection coating (HR) , p(0–10°,1030–1042nm)>99.99% and group delay dispersion |GDD-Rs, p(0–10°,1030–1042nm)|<20fs²) and two inner fused silica plates with a thickness of 1 mm with an anti-reflection coating (AR(0°,950-1050nm)<0.2%) to construct the MPC for the spectral broadening. We use the designed beam parameters for low energy nonlinear mode-matching, shown as blue dashed lines in Fig. 4.5 for the cell alignment which is performed at low input powers. By placing a camera in the expected focal plane and varying the distance between the telescope lenses (see Fig. 4.6), as well as the position of the translation stage including mirrors R1 and R2, the measured beam waist matches our calculations. We then insert the fused silica plates and increase the energy to 78 µJ without making any further changes to the mode-matching optics. Figure 4.8 represents the experimental setup of the MPC, the nonlinearly broadened spectrum and the calculated transform-limited (TL) pulse in the time domain.

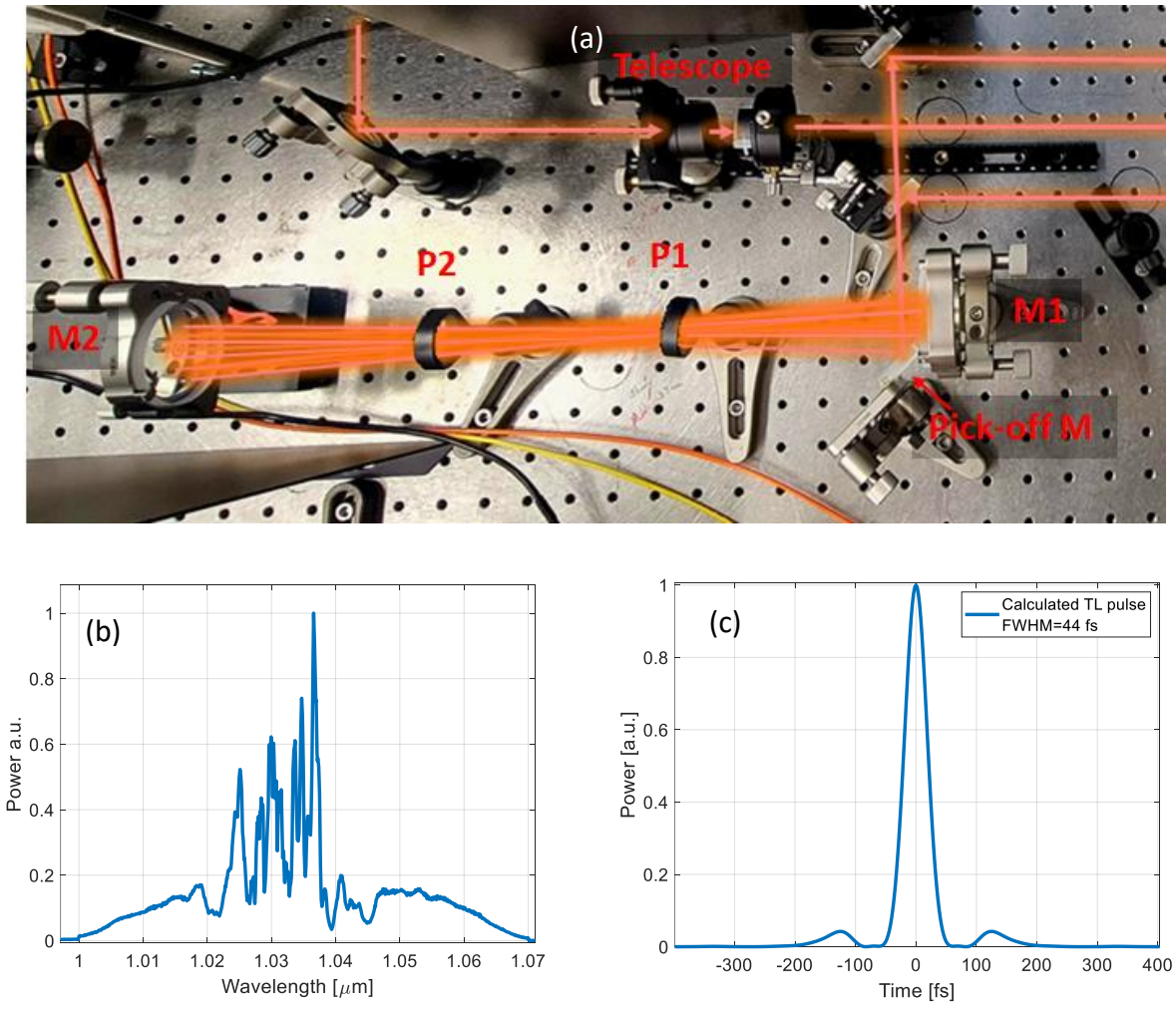

Fig. 4.8 (a) Experimental setup for spectral broadening, (b) nonlinearly broadened spectrum, and (c) the calculated transformation limited (TL) pulse shape in the time domain.

The hybrid MPC has a measured efficiency of 87%. The cell includes 64 passes through AR-coated plate surfaces with a reflectivity of less than 0.2%. Therefore, MPC losses are dominated by linear losses due to the coatings on the MPC optics. A faint blue florescent is observed on a piece of paper located behind the curved MPC mirrors, which is due to the four-wave mixing excitations also reported in references [79,116]. The mixed frequencies are outside the reflection band of our dielectric optics and can therefore be transmitted out of the cell through the optics.

To compress the spectrally broadened pulses, we set up a chirped-mirror compressor inducing a group delay dispersion (GDD) of -200 fs^2 per reflection. Figure 4.9 shows the result of the best-retrieved signal from a second harmonic FROG when the number of bounces is optimized. we could attain an FWHM duration of 44 fs with a small pedestal after the post compression.

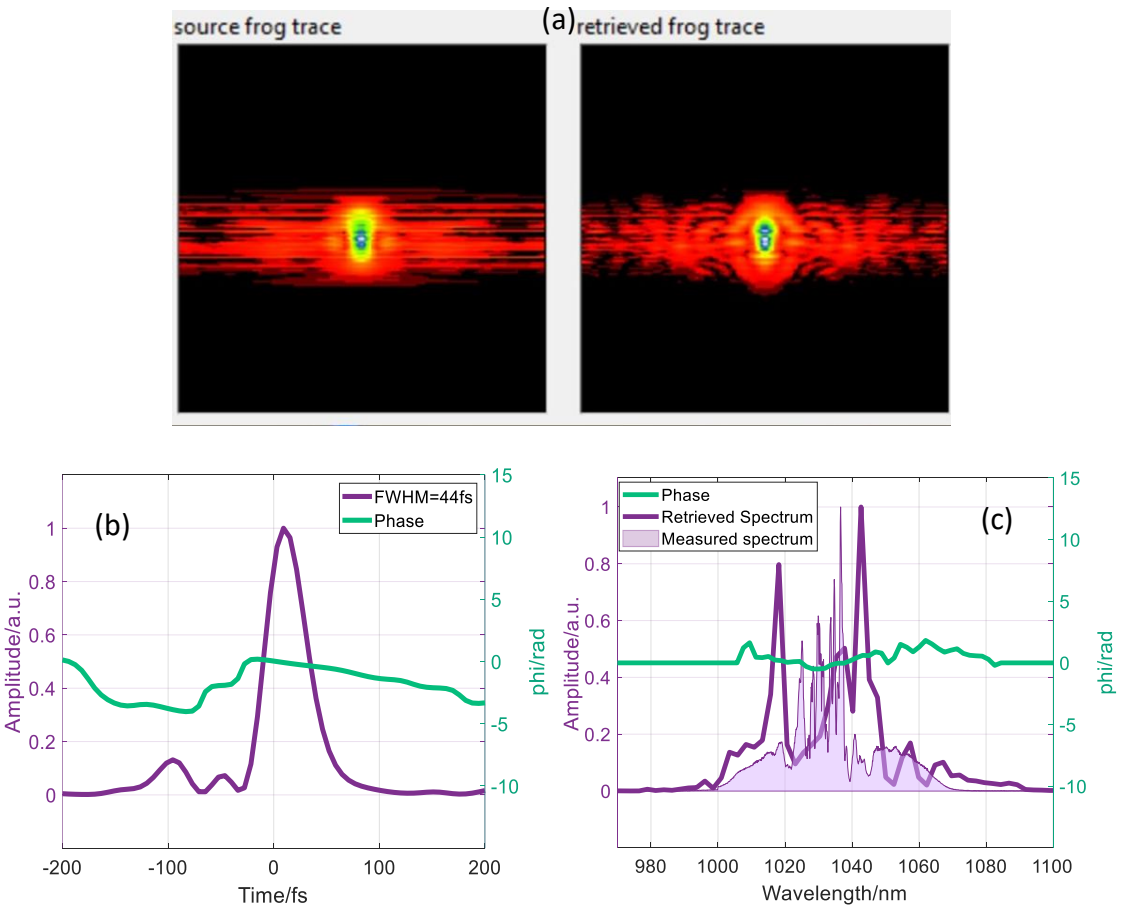

Fig. 4.9 (a) The measured and retrieved FROG traces, (b) The measured pulse duration and the phase by a FROG, (c) The measured and retrieved power spectrum and phase in the frequency domain.

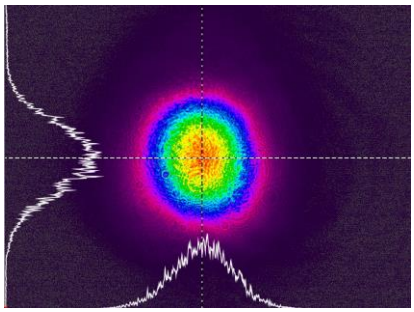

Fig. 4.10 The beam profile after the nonlinear compression unit

For the output beam profile displayed in Fig. 4.10, we measured an M2 value of about 1.2. This nearly Gaussian result underlines the advantages of this approach for spectral broadening compared to single-pass propagation of the pulse in the critical self-focusing regime, which leads to detrimental spatial effects on the beam profile [88]. Eventually, our high-power 1 MHz Yb-doped fiber laser system (shown in Fig. 4.11) delivers 68-µJ, 44-fs pulses with a peak power of up to 1.55 GW desired for the high-harmonic generation with reasonable time resolution and data acquisition time.

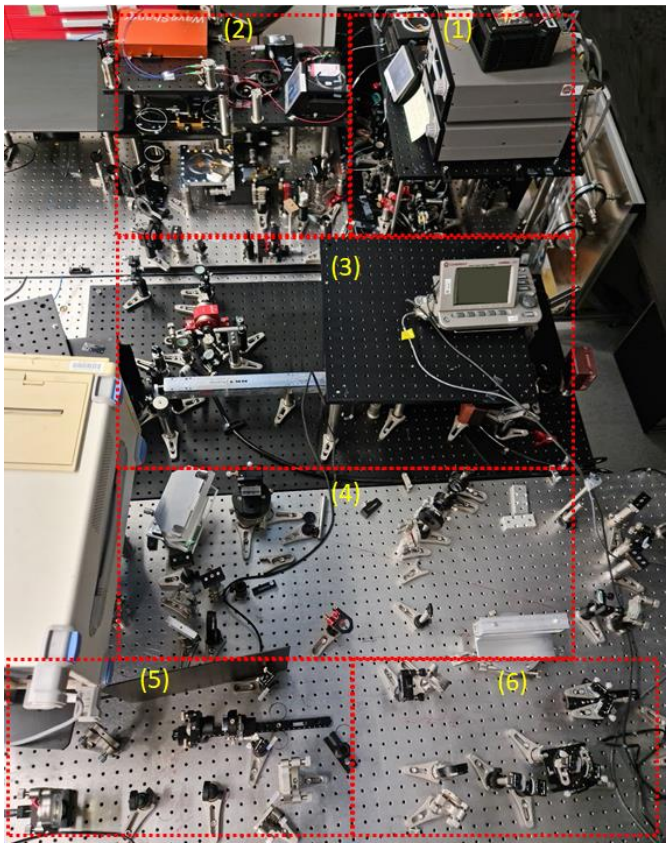

Fig. 4.11 An image of sub-50-fs, 1MHz Yb-doped fiber laser system: (1) The oscillator, (2) The CFBG, wave-shaper and pre-amplifier-chain, (3) The free space isolator, mode-coupling optics and the rod-type amplifier, (4) The linear compressor, (5) The multi-plate multi-pass cell, (6) The post compressor with dispersive mirrors.

5. A fiber front end seed laser for cryogenically cooled Yb:YLF amplifier system

5.1 Introduction

As discussed in Chapter 1, high energy, high average power laser pulses with sub-picosecond pulse duration have numerous applications, such as optical parametric chirped pulse amplification (OPCPA) [117], soft x-ray generation [118], high harmonic generation (HHG) [119], and THz generation [120,121]. The development of lasers with an average power in the kilowatt range is challenging due to the crucial thermal effects. We discussed before, increasing the surface-to-volume ratio of the gain medium for cooling, using Yb^{3+} as the active laser dopant due to its low quantum defect, and the availability of high brilliance laser diode pumps help to scale up the average power into the kW range [109,122].

Yb:YAG with a long fluorescence lifetime and large emission cross section is an attractive laser gain material for high average power laser oscillators and amplifiers. It is thermo-mechanically strong and therefore enables various laser gain geometries such as rod [123–125], thin disk [41,126–128], and crystalline fiber [129]. The thermo-opto-mechanical properties of Yb:YAG are further improved by cooling to cryogenic temperatures ($\sim 80\ K$) [130–133]. At these temperatures, Yb:YAG becomes a four-level laser gain medium enabling efficient amplification with improved thermo-mechanical properties [134].

Unfortunately, the major drawback of Yb:YAG media is its narrow and steep gain profile, as shown in Fig. 5.1 [135]. The gain bandwidth of Yb:YAG narrows from an FWHM of 8 nm at room temperature to 1.5 nm at cryogenic temperatures. As a result, gain narrowing is difficult to compensate for, and the achievable pulse width after amplification is typically limited to 0.5ps-1ps at room temperature and a few picoseconds at cryogenic temperatures [130].

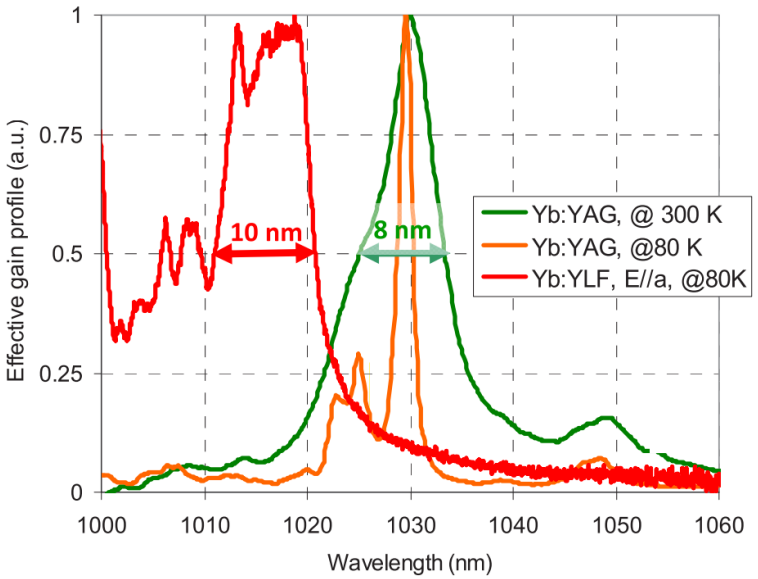

Fig. 5.1 Comparison of the effective cross-section of Yb:YLF (E//a, 80 K) with room temperature (300 K) and cryogenic (80 K) Yb:YAG. A 25% inversion ratio is assumed for Yb:YAG, and all curves are shown in normalized units [135].

The Yb:YLF gain medium, as an alternative, has a wider emission bandwidth even at cryogenic temperatures [136–139]. The uniaxial Yb:YLF material has a gain bandwidth of 10 nm for the E//a axis at 80 K [135]. Moreover, the emission profile is fairly smooth, which minimizes the gain narrowing effects, potentially enabling the amplification of pulses below 300 fs. Also, the parameters of cryogenically cooled Yb:YLF such as thermal conductivity, thermal expansion coefficient and thermo-optical coefficient (dn/dT) are better than those of Yb:YAG at room temperature. It has a negative dn/dT at liquid nitrogen temperatures, which helps to compensate for other thermal lensing effects such as bulges and mechanical stresses, and to achieve good beam quality at high pulse energies and average powers [140].

On the other hand, the emission cross section of Yb:YLF at 80 K is only about 0.7×10^{-20} cm^2 for the E//a axis, which is about three times lower than Yb:YAG at 300 K and 14 times lower compared to cryogenic Yb:YAG [130]. However, the longer fluorescence lifetime, $\tau = 1990$ µs [141], partially compensates for the lower gain and leads to a $\sigma_{em}\tau$ product of 1.4×10^{-23} cm^2.s compared to 2×10^{-23} cm^2.s and 9.4×10^{-23} cm^2.s of room temperature and cryogenic Yb:YAG, respectively [130]. As a result of the small emission cross-section, the saturation fluence (14 J/cm^2) for Yb:YLF is rather high, which complicates the optimization of energy extraction from amplifiers. For example, with a stretched pulse width of 1 ns, the cavity optics have an estimated laser-induced damage threshold (LIDT) of about 6.3 J/cm^2, and for long-term damage-free operation, the amplifier usually needs to operate at a safer value of ~3 J/cm^2 or below. Operating the amplifier at a fluence value much lower than the saturation fluence reduces the extraction

efficiency of the circulating amplified pulse and increases the fluctuations of the output energy in the presence of undesired disturbances [123,130].

In summary, cryogenically cooled Yb:YLF has the potential to realize sub-ps laser sources with high pulse energy and high average power due to its high saturation fluence, longer upper-state lifetime, and lower quantum defect compared to Yb:YAG, when seeded with a suitable input signal [135]. Consequently, a seed laser with a central wavelength of 1016 nm and a broad spectral bandwidth (about 10 nm), as well as a longer stretched pulse duration (> 1 ns) is required to enable efficient and damage-free energy extraction in the Yb:YLF (E//a, 80 K) amplifiers.

A previously implemented cryogenic Yb:YLF CPA laser system, including a Yb-doped all-fiber front-end laser as a seeder, allowed to achieve 100 W at 1 kHz [140]. The seeder consists of a Yb-doped fiber oscillator with normal dispersion (ANDi) mode-locking [142,143] followed by a nonlinear parabolic pulse amplifier and a Gaussian spectral filter (see Fig. 5.2 also References [140] and [143]). It delivers 20 nJ pulses with 2.5 nm FWHM centered at 1018 nm. In this system, the pulse is stretched to 1 ns by two chirped fiber Bragg gratings (CFBG) with a large stretching factor (the first CFBG has a chirp rate of 306 ps/nm and the second one 100 ps/nm) because of its small spectral bandwidth.

In this chapter, the design and construction of an alternative seeder source for the system are explained to investigate the feasibility of generating a spectral bandwidth of 10 nm centered at 1016 nm. This seed pulse, with the same dispersion parameter of 400 ps/nm, can have a duration of about 4 ns and allows for high fluences and more efficient extraction. In addition, the 10 nm bandwidth of this seeder allows the use of the full Yb:YLF gain and can result in a compressed output pulse duration of about 300 fs. The Yb:YLF laser system will be used as a pump source for THz generation, OPCPA pumping, and experiments on pulse compression in multi-pass cells. By using a Yb:YLF slab, the limit of absorbed pump power can be extended to 1 kW average power, so that at least a 3 times increase in output energy and average power can be obtained in future studies [140].

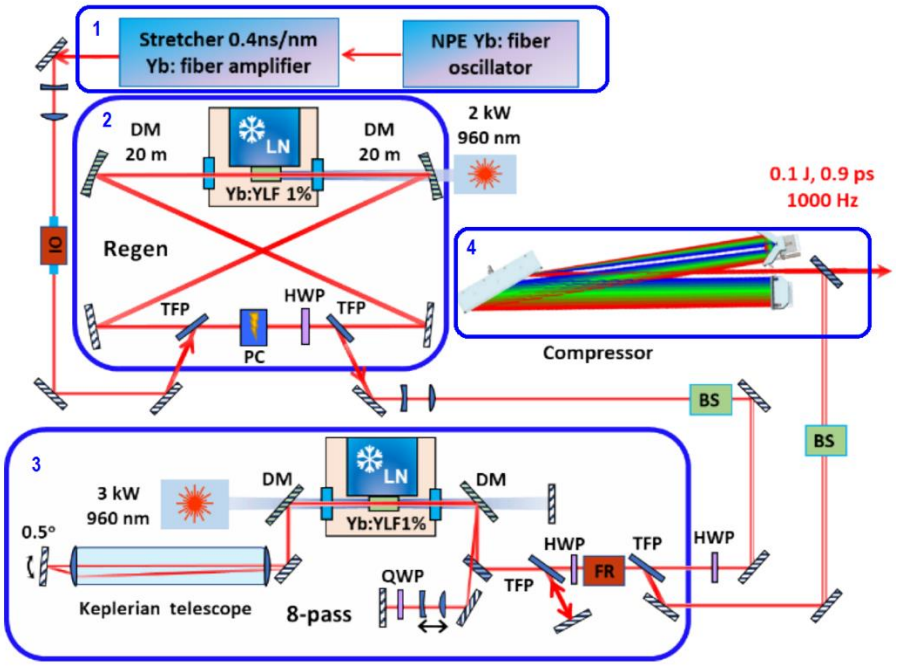

Fig. 5.2 The cryogenically cooled Yb:YLF laser system [140].

5.2 A front-end fiber laser seed source at 1016 nm for cryogenically cooled Yb:YLF laser

The schematic diagram of the laser is shown in Fig. 5.3. It consists of a 40 MHz NLI fiber oscillator with a semiconductor saturable absorber mirror (SESAM), a preamplifier to boost the signal average power for the succeeding nonlinear spectral broadening amplifier which consists of a 3.5 m long Yb-doped gain fiber with a low ion concentration, a bandpass filter (50 nm bandwidth at a center wavelength of 1000 nm) to filter the spectrum at 1016 nm, and finally a core-pumped amplifier with a double-clad Yb-doped phosphosilicate fiber. The system provides about 10 nJ pulses at a repetition rate of 40 MHz centered at 1016 nm with a bandwidth of about 10-12 nm. In the following sections, the different parts of this system are explained and the experimental results are discussed in detail.

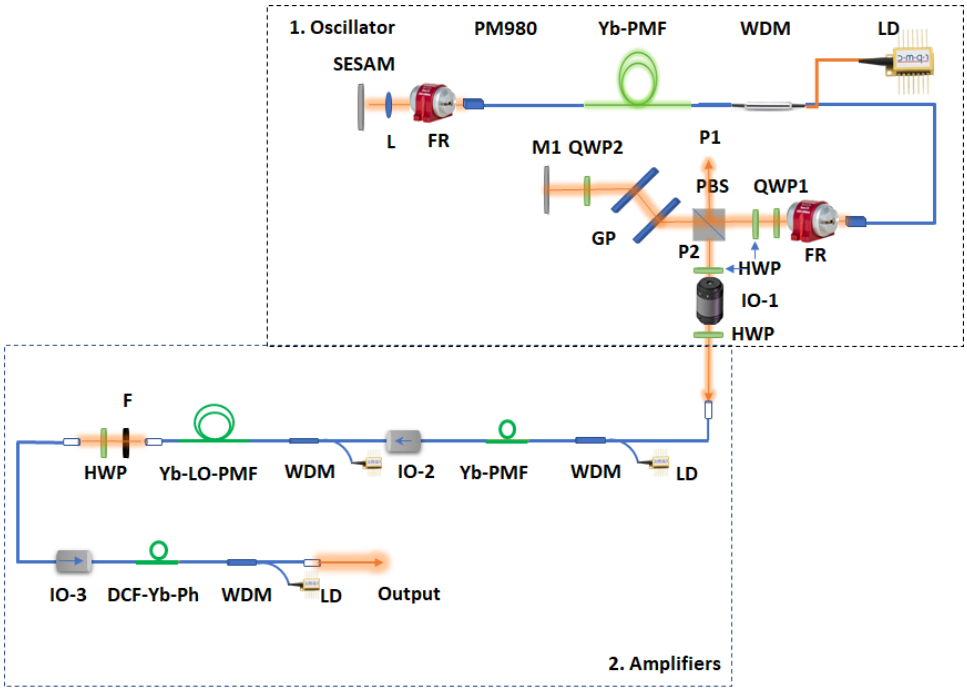

Fig. 5.3 A schematic layout of the 1016 nm laser system as a seeder for cryogenically cooled Yb:YLF amplifier. GP, diffraction grating pair; SESAM, semiconductor saturable absorber mirror; WDM, wavelength division multiplexer; Yb-PMF, Yb-doped polarization maintaining fiber; LO, low doped; DCF-Yb-Ph, double-clad Yb doped in phosphosilicate fiber; M, mirror; QWP, quarter-wave plate; HWP, half-wave plate; F, bandpass filter; PBS, polarization beam splitter; LD, laser diode; IO, isolator.

5.3 NLI mode-locked fiber oscillator with a SESAM

The nonlinear interferometry mode-locked fiber oscillator without SESAM was presented in Chapter 3. We mentioned the pros and also the cons of this oscillator. It is constructed of PM fibers, which are robust to temperature variations and mechanical disturbances. Therefore, it has a low relative intensity noise (RIN) level [81]. However, self-starting mode locking initiates at high pump powers (typically more than 700 mW) in the multi-pulse operation regime. Since there is no isolator inside the cavity, the sensitivity of the mode-locking in single pulse operation to ambient noise is enhanced due to back reflections in the resonator. Once mode locking is lost in this system, it is no longer able to self-start at these low pump levels.

Mode locking in an NPE-based oscillator, on the other hand, starts at low pump powers in single-pulse mode (<70 mW) and is quite stable over the long-term operation, but the intensity noise is higher because of the single-mode non-PM fibers in this scheme, so the output pulse amplitudes are sensitive to environmental fluctuations. Therefore, NPE mode-locked lasers must be operated in a highly controlled environment.

One solution for fabricating a laser that has both advantages of the above configurations, i.e., self-start mode-locking at low pumping levels in the single pulse regime in addition to low intensity noise levels, is an NLI oscillator with an internal SESAM. Essentially, a saturable absorber in the laser cavity results in lower power losses for the peak intensity of a circulating ultrashort pulse and higher losses for low-intensity light incident on the absorber. This mechanism promotes the pulse peak and can therefore contribute to the formation and stabilization of a relatively short pulse. An NLI-based mode-locked oscillator operating in the soliton regime (small net negative dispersion) benefits from this effect of the SESAM, reducing the threshold for self-start mode-locking to low pump power levels at single-pulse operation. The generation of a relatively short pulse with a SESAM produces higher nonlinearity at low pump powers (low intracavity energies) and thus supports soliton generation and stable mode-locking at these powers.

We employ an available SESAM with a 15% absorbance at 1040 nm to investigate the self-start mode-locking threshold and stability of the NLI-oscillator. The specifications and the reflectance of the SESAM are presented in Table 5.1 and Fig. 5.5, respectively. A picture of the NLI plus SESAM mode-locked oscillator is also shown in Fig. 5.6.

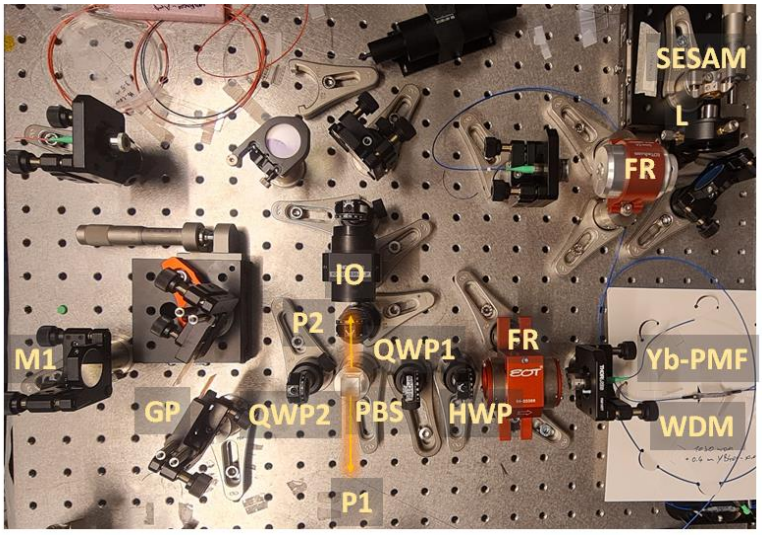

Fig. 5.4 The NLI plus SESAM oscillator

Table 5.1 Specifications of the SESAM

SAM-1040-15-500FS	
LASER WAVELENGTH	λ = 1040 nm
HIGH REFLECTION BAND	λ = 980 ... 1070 nm
ABSORBANCE	A_0 = 15 %
MODULATION DEPTH	ΔR = 8 %
NON-SATURABLE LOSS	A_{ns} = 7 %
SATURATION FLUENCE	Φ_{sat} = 50 µJ/cm^2
RELAXATION TIME CONSTANT	τ ~ 500 fs
DAMAGE THRESHOLD	Φ = 1.8 mJ/cm^2
CHIP AREA	4.0 mm x 4.0 mm

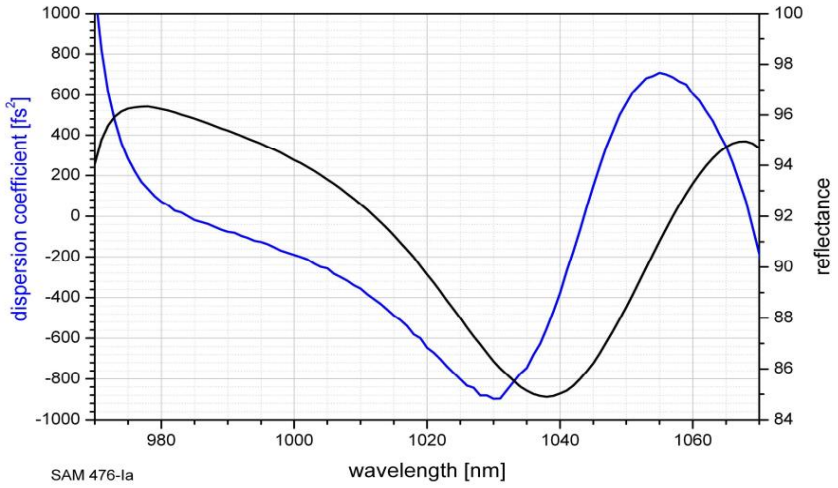

Fig. 5.5 Dispersion coefficient and the reflectance of the SESAM (SAM-1040-15-500fs).

This oscillator is self-mode-locked at a pump current of 226 mA (approx. 100 mW) in the single pulse mode. This is investigated with increasing pump power to observe the multi-pulse behavior, which can be seen in the fringe formation in the output spectrum and also in the behavior of the pulse train and amplitude in the oscilloscope. In fact, with a gradual reduction of the pump level, the transition from multi-pulse operation to single-pulse operation can be observed from the output spectrum and the amplitude level of the pulse train. With reduction of the pumping level in the multi-pulse mode, the pulse amplitude also decreases, but at a certain pumping level (227 mA), an increasing jump in the signal level can be observed at the oscilloscope, meaning that the sub-pulses disappear and their energy transfers to the single pulse. Further pump power reduction decreases the signal level until the laser transit to the CW operation at 80 mW of pump level (160 mA). The NLI-plus-SESAM oscillator provides a self-start mode-locked oscillator in the single pulse regime with an output power of 4 mW for the transmission port (P2) and 2.5 mW for

the reflection port (P1). The output spectrum of port P2 and the pulse train at a repetition rate of 40 MHz are shown in Fig. 5.6.

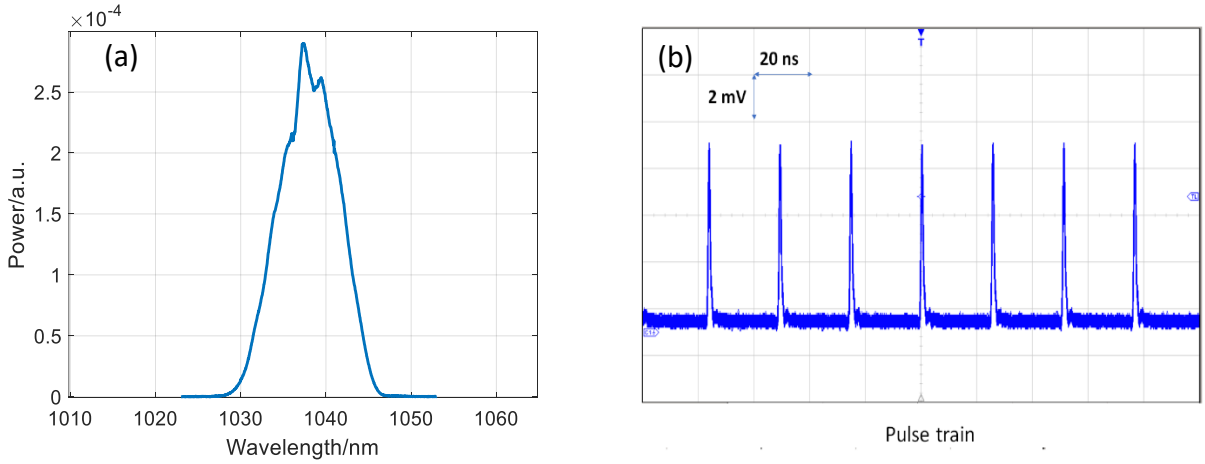

Fig. 5.6 (a) The power spectrum of the transmission port of the NLI+SESAM oscillator, (b) The pulse train.

5.4 Nonlinear spectral broadening

The output signal of the oscillator is coupled into the first preamplifier, which consists of a PM-Yb doped aluminosilicate fiber (Coractive; Yb-401-PM), after propagating through a free-space isolator (Fig. 5.3). This preamplifier enhances the signal amplitude and gives us the opportunity to optimize the input pulse energy for the following nonlinear preamplifier, which is built with 3.5 m of a low-doped Yb gain to spectrally broaden the input signal. We first simulate the nonlinear amplification in this fiber. Fig. 5.7 shows the spectra of the seed and the nonlinearly broadened signals (signal average power= 20 mW, pump power= 1 W). The spectral power is lower for the wavelengths below the oscillator central wavelength (1038 nm) due to the higher absorption of the gain fiber at lower wavelengths. Using a 50 nm band-pass filter centered at 1000 nm results in a signal with a bandwidth of 13 nm centered at 1016 nm (Fig. 5.8).

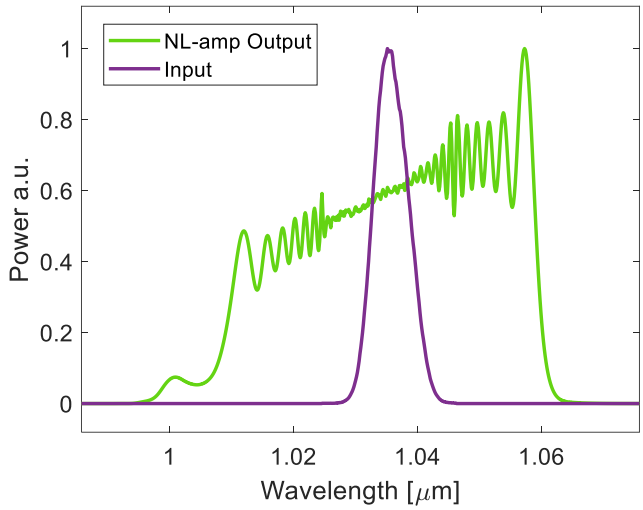

Fig. 5.7 The simulated nonlinearly amplified pulse spectrum; NL-amp, nonlinear amplifier.

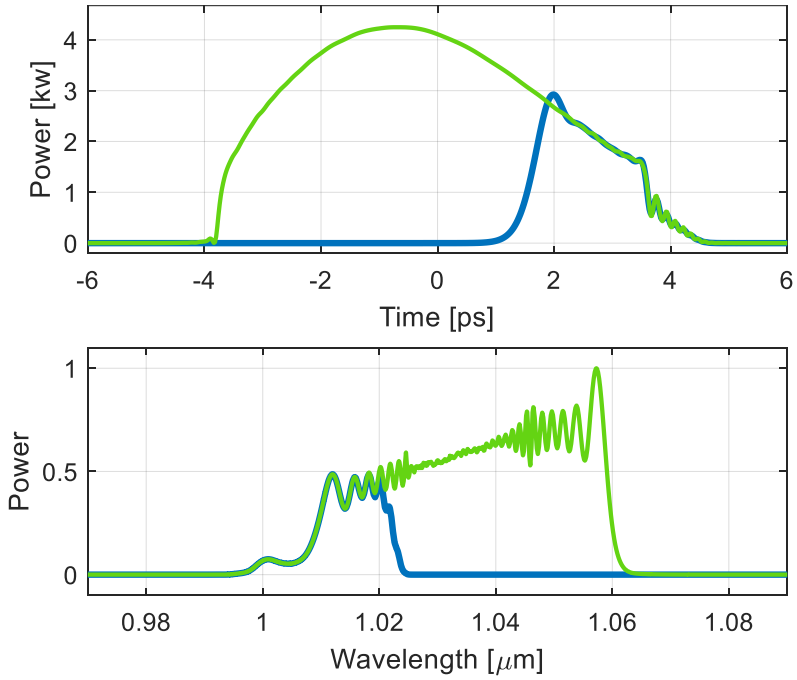

Fig. 5.8 The simulated nonlinearly broadened signal in time and frequency domain before (green) and after filtering (blue).

We studied the nonlinear amplification experimentally with a seed average power of 20 mW and a pump power of about 1 W. We achieved a bandwidth of 12 nm centered at 1015 nm, as shown in Fig. 5.9. The average signal power before and after filtering was measured to be 384 mW and

38 mW, respectively. The average power of the output signal is large enough to fully saturate the next amplifier, which is a highly doped Yb-in-phosphosilicate gain fiber explained in the next section.

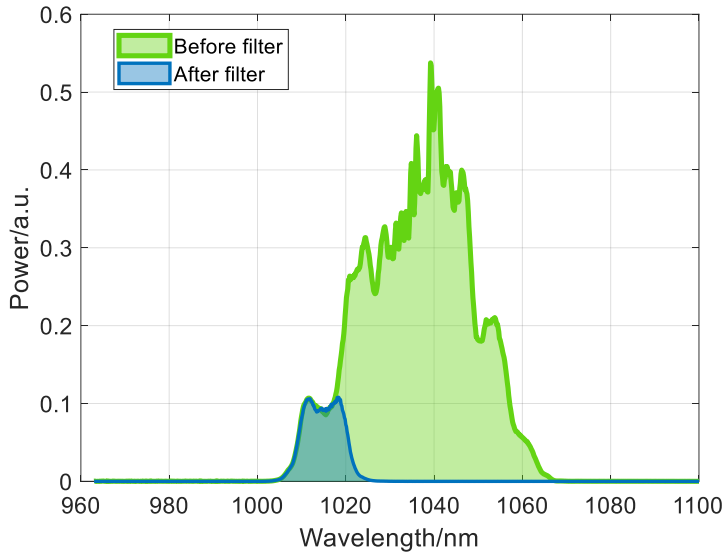

Fig. 5.9 The experimental result for the spectrally broadened (green) and the filtered signals (blue) after the nonlinear amplifier.

5.5 Core-pumped double-clad Yb-doped in phosphosilicate amplifier

The main difficulty in amplifying the signal centered at 1015 nm with the conventional Yb-doped fibers (with aluminosilicate hosting glass) is the tendency to shift the power of the central wavelength to the longer wavelengths. The key reason for this shift is the pattern of the emission and absorption cross-sections for these fibers. However, with proper gain length and pump and signal power, one can minimize this effect, but it is still quite large for a signal centered at 1015 nm, which is discussed in this section. The emission and absorption cross sections of both gain fibers (i.e. Yb in aluminosilicate and phosphosilicate) are represented in Fig. 5.10. The emission peak in the wavelength range from 1000 to 1050 nm is around 1026 nm for aluminosilicate and 1007 nm for phosphosilicate fibers. In addition, the aluminosilicate fiber has a steeper gain profile than the phosphosilicate fiber, resulting in a greater gain narrowing effect during amplification. In both fibers, the absorption at lower wavelengths in this range is higher than at longer wavelengths.

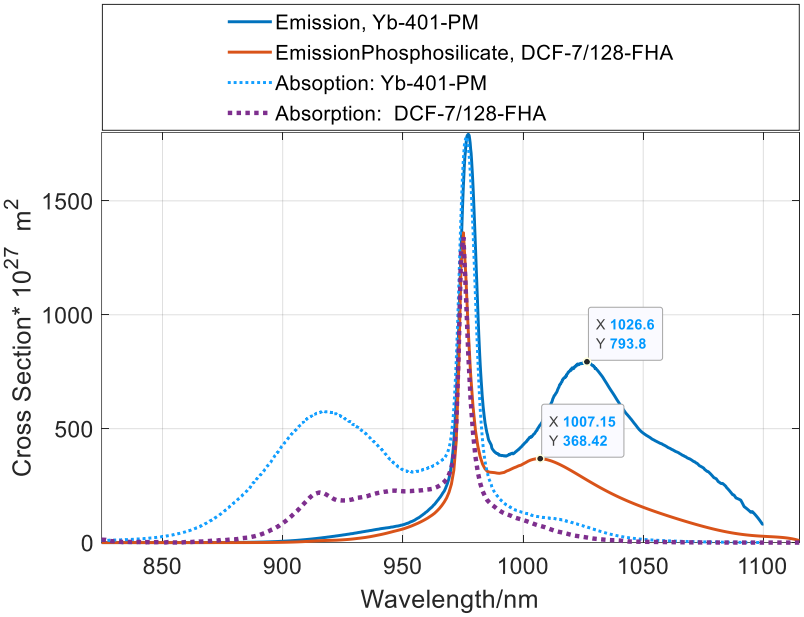

Fig. 5.10 Emission and absorption cross-sections of the Yb-doped fiber in aluminosilicate (Yb-401-PM) and phosphosilicate fibers (DCF-7/128-FHA) manufactured by CorActive.

One can simulate the amplification in both fibers with a suitable length and pump power, to saturate the amplifiers and compare the influence of different emission and absorption patterns of fibers on the output spectrum. The Yb-doped-phosphosilicate gain fiber (DCF-7/128-FHA; see Table 5.2) is a double-clad fiber and has a Yb^{3+} ion concentration of $48 \times 10^{25} ion/m^3$ which is almost 10 times higher than that of the single-clad Yb-401-PM aluminosilicate fiber ($4.65 \times 10^{25} ion/m^3$), both manufactured by CorActive. We simulate pulse amplification in an 80 mm core-pumped DCF-7/128-FHA and a 300 mm single-clad Yb-401-PM amplifying fiber. The pump power is 1 W in both cases and the input signal is 38 mW. The input signal is the experimental result after the filtering shown in the last section. The normalized spectral output power for both cases is calculated which is shown in Fig 5.11. The Yb-401-PM gain profile clearly shifts the center of the power spectrum to the longer wavelengths and makes the bandwidth narrower. In contrast, the phosphosilicate DCF-7/128-FHA has barely any effect on the spectrum. The simulated output power at 1 W pump power is about 700 mW for both cases.

Table 5.2 The specification of the Yb doped in phosphosilicate fiber; (DCF-YB-7/128-FHA - Coractive).

DCF-YB-7/128-FHA

Yb-doped fiber for pulsed lasers

Specifications

Optical

Cladding Absorption @ 915 nm (dB/m)	1.3 ± 0.2
Cladding Absorption @ 975 nm – Nominal (dB/m)	7.8
Numerical Aperture – Core	0.19 ± 0.02
Numerical Aperture – Cladding	> 0.45

Geometrical & Mechanical

Core Diameter (µm)	7 ± 1
Cladding Diameter (µm)	128 ± 3
Core/Cladding Concentricity Error (µm)	< 1
Cladding Geometry	Octogonal
Coating Diameter (µm)	260 ± 20
Proof Test (kpsi)	≥ 100

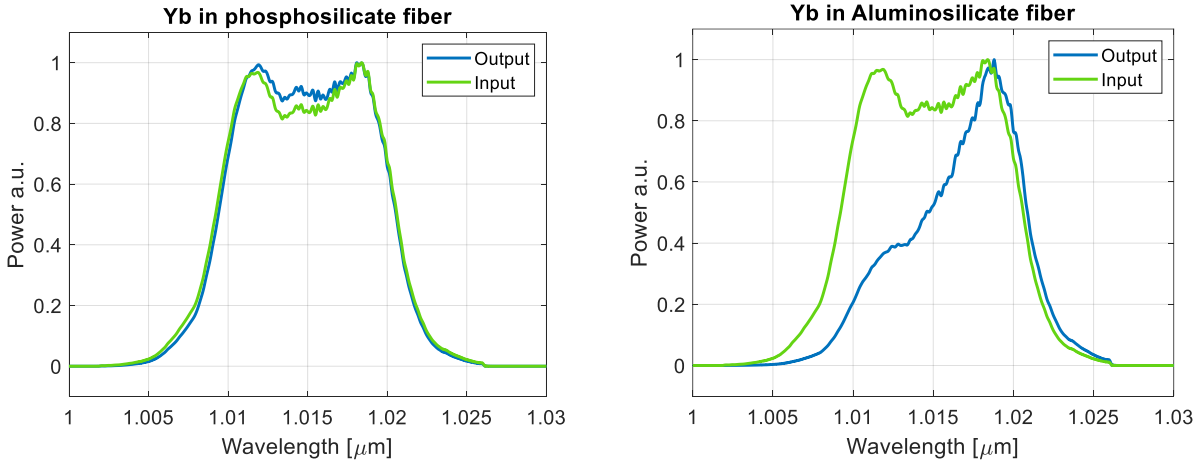

Fig. 5.11 The simulated output spectrum in saturated amplifiers; (a) 8cm of Yb-doped-phosphosilicate gain fiber, (b) 30 cm of Yb-doped-aluminosilicate gain fiber

We construct a preamplifier with a 90 mm phosphosilicate gain fiber (DCF-7/128-FHA) pumped into the core. This fiber is a non-PM fiber and has low splice loss when matched to standard single-mode non-PM fibers such as HI 1060. It has higher saturation energy than Yb-401-PM, which allows more efficient power extraction from the preamplifier. The manufacturer also

demonstrates a photodarkening-free performance for this fiber in [144], allowing long-term operation without degradation at high pump powers.

The power spectrum and the average power of the amplified pulses are depicted in Fig. 5.12. The spectrum is centered at 1016 nm and has a bandwidth of 12 nm. A small spectral broadening occurs in the fiber due to the SPM. It can be eliminated with a properly stretched pulse, which is explained in the next section. In summary, the Yb-doped phosphosilicate amplifying fiber is a suitable solution for the amplification of a relatively broad spectrum (here ~ 12 nm) centered at 1016 nm. This system (shown in Fig. 5.13) achieves pulses with a pulse energy of about 10 nJ at a repetition rate of 40 MHz and a bandwidth of 12 nm at 1016 nm, making it an ideal seed laser for cryogenically cooled Yb:YLF amplifiers. To our knowledge, it produces the widest bandwidth to date at 1016 nm. It is a prototype for a more general design presented in the next section to investigate the feasibility of amplification at this wavelength region without significant power shift to the longer wavelengths. This is a possible source for a high energy, high average power Yb:YLF laser amplifier, which has the potential to produce pulse durations of less than 400 fs.

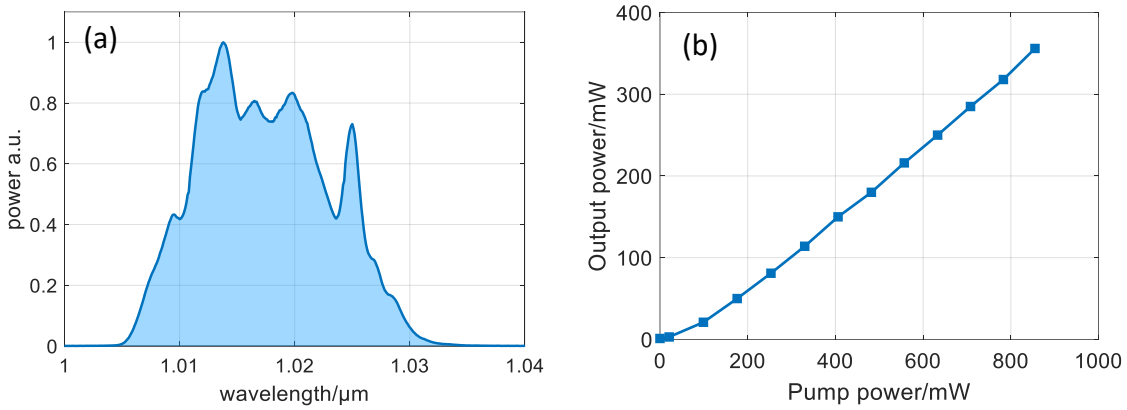

Fig. 5.12 (a) The experimental power spectrum after amplification with a 9 cm of phosphosilicate Yb-doped fiber, (b) The output power.

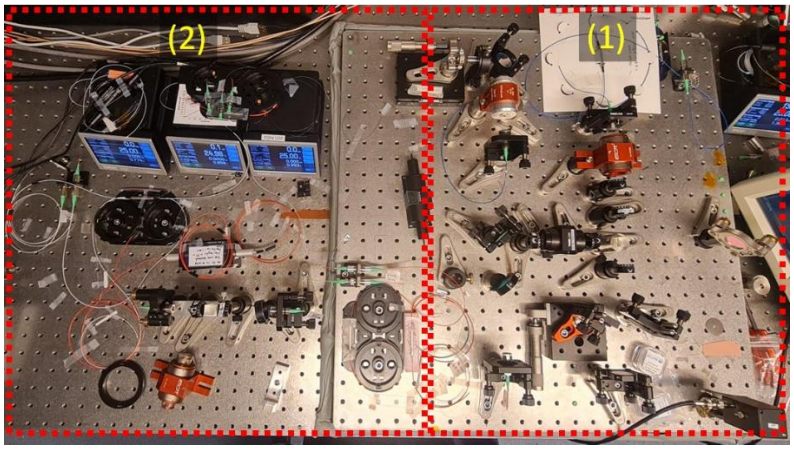

Fig. 5.13 An image of the experimental setup: (1) The oscillator, (2) Amplifiers.

5.6 A design for 1 μJ, 10 nm bandwidth seeder at 1016nm for Yb:YLF

The possibility of creating a seeder centered at 1016 nm with a bandwidth greater than 10 nm was discussed in the last section. Experimental results show that the specially designed amplifiers using Yb-doped phosphosilicate fibers are promising when used as preamplifiers without significant gain narrowing at 1016 nm and power transfer to longer wavelengths. We achieved about 10 nJ, 40 MHz pulses with more than 10 nm bandwidth centered at 1016 nm. For a seed signal with higher pulse energy, we would need to stretch it to mitigate the nonlinearities. Here, we design a CPA system with a suitable stretcher to lengthen the pulses to about 3 ns, allowing more energy extraction in the Yb:YLF amplifier. A schematic representation of the design is shown in Fig. 5.14. In this design, we use the experimental output signal after filtering the nonlinearly broadened spectra at 1015 nm (see Fig. 5.10) as the source signal for the stretcher and amplifiers.

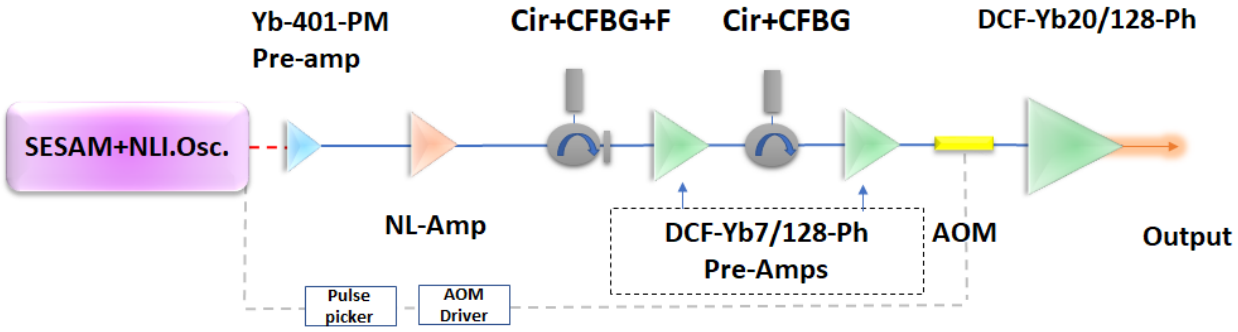

Fig. 5.14 A schematic of the CPA system to generate around 1 μJ, 3 ns pulses centered at 1016nm. Cir, circulator; CFBG, chirped fiber Bragg grating; F, filter; DCF, double-clad fiber; Ph, phosphosilicate; AOM, acousto-optic modulator; SESAM, semiconductor saturable absorber; NLI.Osc., nonlinear interferometer mode-locked oscillator; Yb, ytterbium; PM, polarization maintaining; NL-Amp, nonlinear amplifier.

The stretcher must extend the pulse to a duration of at least 3 ns and be perfectly matched to the dispersion parameters of an available Treacy compressor following Yb:YLF amplifier displayed in Fig. 5.2 (Grating groove density of 1760 l/mm with a Littrow angle of 63.39˚ at 1016 nm). Starting from the spectrally filtered signal shown in Fig. 5.9 (blue), one can simulate the stretched signal after reflection from two tunable CFBGs and amplification in two core-pumped Yb phosphosilicate fibers (CoreActive; DCF-Yb7/128-Ph). The preamplifiers are required to compensate for losses in the circulator, CFBGs, and filter. Besides, they are necessary to overcome the loss in the AOM and boost up the signal average power after the reduction of the repetition

rate from 40 to 10 MHz to saturate the final amplifier. The main amplifier is made with a cladding-pumped double-clad 20/128 µm Yb phosphosilicate gain fiber (CoreActive; DCF-Yb20/128-Ph) with a 25 W multi-mode laser diode.

The seed signal centered at 1015 nm with 12 nm bandwidth requires a total dispersion parameter of 250 ps/nm to be stretched to about 3 ns. Considering this parameter, as well as the dispersion parameters of the fiber components in the system, and the available dispersion for the compressor (angle of incidence: 60˚, normal spacing of the grating: 698 mm), the corresponding third-order dispersion (TOD) of the CFBGs can be calculated for a perfectly compressed output signal. The stretched pulse is simulated as shown in Fig 5.15. In this calculation, the second-order dispersion is 69.1916 ps2 and the TOD is -1.3492 ps3 for each CFBG. The reflection bandwidth for each CFBG is 18 nm, centered at 1016 nm, and two of them are used to obtain a total chirp parameter of -252.52 ps/nm.

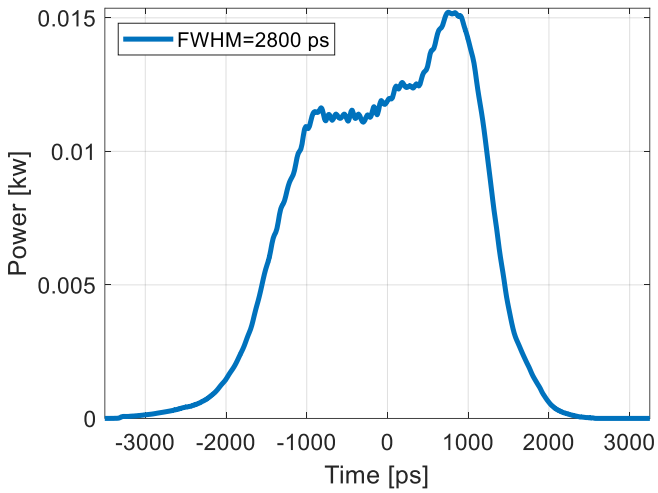

Fig. 5.15 The simulated stretched-pulse after reflection from two CFBGs and amplification through core-pumped preamplifiers shown in Fig. 5.14.

The stretched signal is amplified with a second core-doped DCF-Yb7/128-Ph (80 mm) preamplifier, and then the pulse repetition rate is reduced from 40 MHz to 10 MHz using the AOM as a pulse picker. Finally, the signal is amplified with a 400-mm, cladding-pumped DCF-Yb20/128-Ph. The simulated output power in the time and frequency domain is depicted in Fig. 5.16. The spectral bandwidth is about 10.5 nm and the pulse duration is 2750 ps. The calculated average output power is 7 W at 25 W forward pump power, which corresponds to a pulse energy of 700 nJ at a repetition rate of 10 MHz.

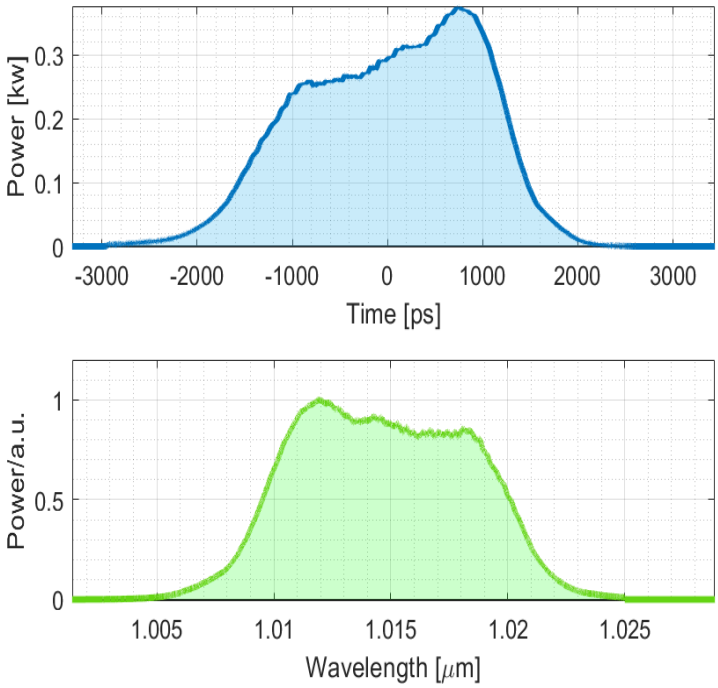

Fig. 5.16 The simulated output of the front-end fiber laser shown in Fig. 5.14.

The simulated seed signal shown in Fig. 5.16 is used to calculate the evolution of the signal output power passing through a Yb:YLF regenerative amplifier and a subsequent Yb:YLF multi-pass amplifier [134]. A typical simulated output power spectrum of a Yb:YLF system (simulated in our team) is depicted in Fig. 5.17 (a). This allows us to investigate the possibility of a perfect compression of the pulse with the parameters provided for the compressor (AOI of 60 degrees, groove density of 1760 l/mm, grid normal spacing of 698 mm). Fig. 5.17 (b) shows the calculated transform-limited pulse (369 fs, shown in purple) in the time domain corresponding to the power distribution in the frequency domain shown in Fig. 5.17(a), and the possible compressed pulse (green) with the dispersion parameters mentioned for the stretcher, the laser components and the compressor.

As conclusion, the experimental results for preamplification of a relatively broad signal at 1016 nm, as well as the simulated results for a cryogenic Yb:YLF laser system including higher amplification factors (Fig. 5.14) encourage us that phosphosilicate fibers doped with Yb^{3+} ions are a promising candidate for seeders operating at 1016 nm without significant gain narrowing or power transfer to longer wavelengths.

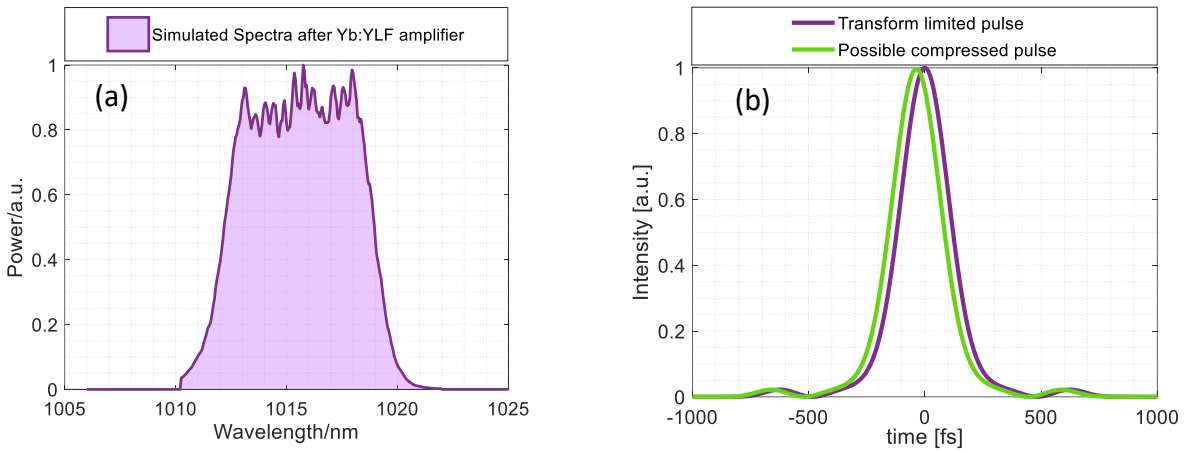

Fig. 5.17 The simulated output signal from the Yb:YLF laser amplifier in frequency (a) and time (b) domain. The green curve is the possible compressed pulse.

6. Conclusion and outlook

In this dissertation, we demonstrate the design and experimental prototypes of two ultrashort fiber laser front-end systems in the wavelength range of 1 µm for, (i) high harmonic generation and (ii) source signal generation for the cryogenically cooled Yb:YLF amplifier. These sources are built and studied by constructing two different fiber oscillators (i.e., NPE and NLI+SESAM mode-locked oscillators), applying the CPA technique, linear and nonlinear signal amplifying in different types of gain fibers, spectral amplitude, and phase shaping, nonlinear spectrum broadening for reasons such as spectrum selection in a specific wavelength region or post-compression units.

Chapters 1 through 4 describe the design and construction of a 68 W, 44 fs, 1 MHz laser source at 1030 nm that produces a peak power of 1.5 GW suitable for HHG and tr:ARPES applications. An NPE mode-locked oscillator is constructed to deliver an average power of nearly 10 mW at 1030 nm with a bandwidth of 20 nm and a pulse repetition rate of 24 MHz. It is self-mode locked at low pump powers in the single-pulse regime. The mode-locking mechanism in this oscillator enables long-term stability with reasonable average output power at low repetition rates, resulting in a simpler design for the amplifiers in combination with the pulse picker to amplify ultrashort pulses with a required repetition rate of 1 MHz. A Finisar wave-shaper is used to form a near-parabolic spectral power distribution for the signal that leads to minimizing the pedestals in the linear pulse compression (utilizing a Treacy-type compressor) after the amplifier chain. Finally, pulses as short as 44 fs with a pulse energy of about 68 µJ are achieved after nonlinear pulse compression in a hybrid multi-pass dual-plates Herriott-type cell.

This system must be properly sealed in further steps to control the influence of ambient noise on the output signal. As mentioned in Chapters 3 and 5, since the NPE oscillator is composed of non-PM single-mode fibers, the output pulse amplitude and spectral shape are sensitive to environmental changes such as temperature variations and mechanical noise. As a result, the oscillator exhibits higher relative intensity noise (RIN) than the NLI-mode oscillator, which is composed entirely of PM fibers. Therefore, shielding and appropriate packaging of the oscillator helps to eliminate this problem.

With the various features of the wave shaper such as filtering with arbitrary spectral shapes, dispersion compensation, generation of specific phase variations and temporal pulse shapes (e.g. rectangular, etc.), or specific pulse sequences, interesting experiments can be implemented. For instance, a tunable laser source can be realized utilizing the spectral phase shaping of Finisar in conjunction with a dispersion-balanced multi-plate MPC (consisting of dispersive curved mirrors instead of the nondispersive ones used in this work), as reported by Prannay Balla and others in [145] . A temporal saw-tooth pulse can be generated by employing proper spectral phase shaping. When it is sent through a dispersion-balanced nonlinear multi-pass cell, its frequency is shifted as $\Delta\omega = -\Phi_{NL}\frac{dI(t)}{dt}$ (where $I(t)$ is the time-dependent laser intensity and Φ_{NL} is the accumulated

nonlinear phase), and can be filtered with a dichroic filter, as demonstrated in Fig. 6.1. A wavelength shift from 1030 nm to 1000 nm and to 1060 nm is reported with this technique [145].

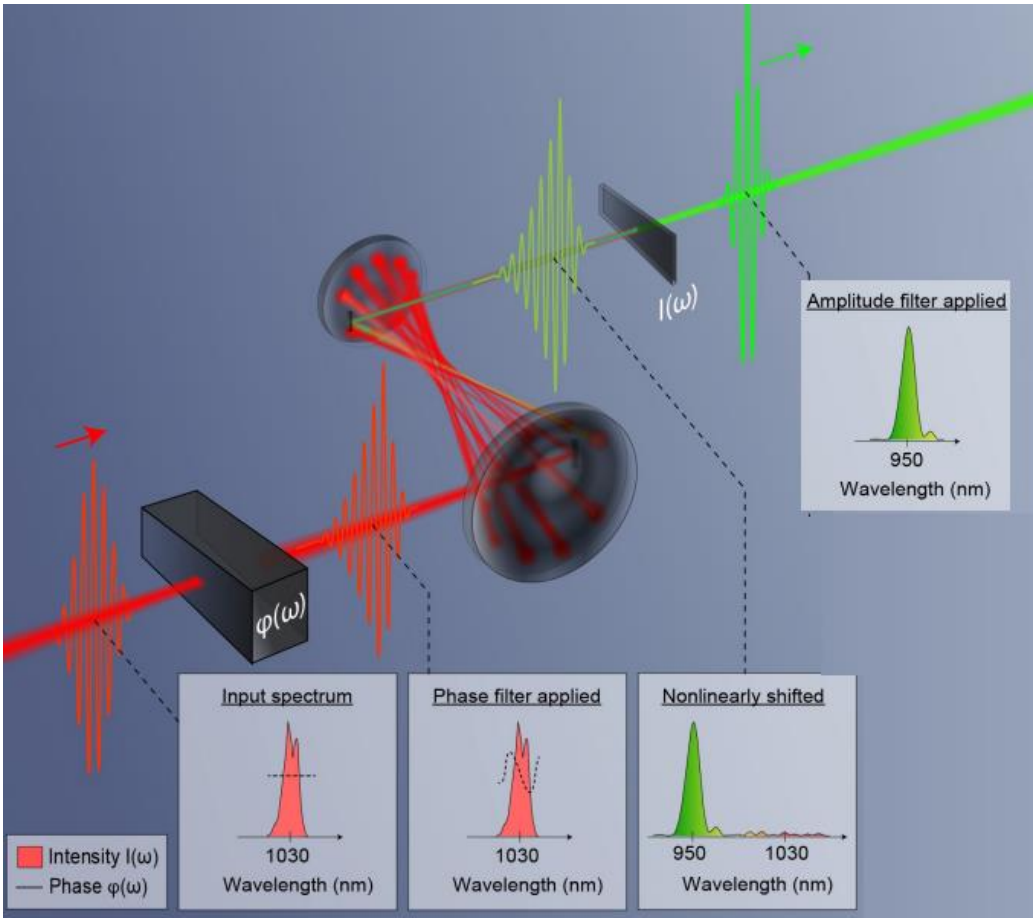

Fig. 6.1 The principle of frequency shifting using spectral phase shaping and a dispersion-balanced MPC [145].

In Chapter 5, we report a laser source at 1016 nm with a bandwidth greater than 10 nm as a seed source for Yb:YLF amplifiers at liquid nitrogen temperature. To our knowledge, this is the largest bandwidth achieved from an ultrafast Yb-doped fiber laser in this wavelength range. For the first time, the mode-locking mechanism of an NLI+SESAM mode-locked oscillator is investigated to be applied as a stable and low noise source for the system. A SESAM improves the mode-locking stability of an NLI oscillator in single pulse mode. It can initiate the mode-locking mechanism at lower energy levels in the resonator and decrease the self-start mode-locking threshold down into the single-pulse operation instead of the multi-pulse regime. Thanks to the PM fibers in this configuration, the amplitude of the output pulses is less sensitive to ambient noise. We generate a bandwidth of about 12 nm centered at 1016 nm with nonlinear amplification in the preamplifier

and a suitable filter. The bandwidth can be further improved by using a SESAM centered at 1030 nm instead of the 1040 nm that was used in the oscillator.

This work demonstrates that the use of Yb-doped phosphosilicate fibers allows amplifying the signal at 1016 nm without significant red shift of the central wavelength, as is the case with standard Yb-doped aluminosilicate fibers due to their gain profile. In this prototype, we achieve nearly 10 nJ pulses at 40 MHz with a center wavelength of 1016 nm and an FWHM of 12 nm. This signal exhibits a slight spectral broadening due to the SPM that can be alleviated in the further steps via the CFBGs as the stretchers. We calculate the appropriate stretching factor to prolong the pulse to the duration of about 3 ns desired for Yb:YLF amplifiers. The main goal for further developments in this system is to improve this prototype for more energy extraction via the CPA technique, core-pumped Yb-doped phosphosilicate (Yb-Ph) preamplifiers, repetition rate reduction, and cladding pump LMA Yb-Ph amplifiers to achieve up to 1 μJ pulses stretched to 3ns with more than 10 nm bandwidth at 1016 nm, which makes it as an ideal seed source for Yb:YLF amplifier.

7. Bibliography

1. E. Snitzer, "Proposed Fiber Cavities for Optical Masers," Journal of Applied Physics **32**(1), 36–39 (1961).
2. C. J. Koester and E. Snitzer, "Amplification in a Fiber Laser," Appl. Opt., AO **3**(10), 1182–1186 (1964).
3. A. E. Willner, R. L. Byer, C. J. Chang-Hasnain, S. R. Forrest, H. Kressel, H. Kogelnik, G. J. Tearney, C. H. Townes, and M. N. Zervas, "Optics and Photonics: Key Enabling Technologies," Proceedings of the IEEE **100**(Special Centennial Issue), 1604–1643 (2012).
4. M. Zervas, "High power ytterbium-doped fiber lasers - Fundamentals and applications," International Journal of Modern Physics B **28**, (2014).
5. P. Mulser and D. Bauer, *High Power Laser-Matter Interaction*, Springer Tracts in Modern Physics (Springer, 2010), **238**.
6. A.-L. Viotti, M. Seidel, E. Escoto, S. Rajhans, W. P. Leemans, I. Hartl, and C. M. Heyl, "Multi-pass cells for post-compression of ultrashort laser pulses," Optica, OPTICA **9**(2), 197–216 (2022).
7. J. Lopez, M. Faucon, R. Devillard, Y. Zaouter, C. Hönninger, E. Mottay, and R. Kling, "Parameters of Influence in Surface Ablation and Texturing of Metals Using High-power Ultrafast Laser," Journal of Laser Micro / Nanoengineering **10**, (2015).
8. F. Albert, M. E. Couprie, A. Debus, M. C. Downer, J. Faure, A. Flacco, L. A. Gizzi, T. Grismayer, A. Huebl, C. Joshi, M. Labat, W. P. Leemans, A. R. Maier, S. P. D. Mangles, P. Mason, F. Mathieu, P. Muggli, M. Nishiuchi, J. Osterhoff, P. P. Rajeev, U. Schramm, J. Schreiber, A. G. R. Thomas, J.-L. Vay, M. Vranic, and K. Zeil, "2020 roadmap on plasma accelerators," New J. Phys. **23**(3), 031101 (2021).
9. I. Orfanos, I. Makos, I. Liontos, E. Skantzakis, B. Förg, D. Charalambidis, and P. Tzallas, "Attosecond pulse metrology," APL Photonics **4**(8), 080901 (2019).
10. S. Hädrich, J. Rothhardt, M. Krebs, S. Demmler, A. Klenke, A. Tünnermann, and J. Limpert, "Single-pass high harmonic generation at high repetition rate and photon flux," J. Phys. B: At. Mol. Opt. Phys. **49**(17), 172002 (2016).
11. J. S. Feehan, J. H. V. Price, T. J. Butcher, W. S. Brocklesby, J. G. Frey, and D. J. Richardson, "Efficient high-harmonic generation from a stable and compact ultrafast Yb-fiber laser producing 100 μJ, 350 fs pulses based on bendable photonic crystal fiber," Appl. Phys. B **123**(1), 43 (2017).
12. D. J. Richardson, J. Nilsson, and W. A. Clarkson, "High power fiber lasers: current status and future perspectives [Invited]," J. Opt. Soc. Am. B, JOSAB **27**(11), B63–B92 (2010).
13. C. L. Arnold, S. Mikaelsson, J. Vogelsang, C. Guo, I. Sytcevich, A.-L. Viotti, F. Langer, Y.-C. Cheng, S. Nandi, A. Olofsson, R. Weissenbilder, J. Mauritsson, A. L'Huillier, and M. Gisselbrecht, "A high-repetition rate attosecond pulse source for time-resolved coincidence spectroscopy and nanoscale imaging," in *Conference on Lasers and Electro-Optics (2021), Paper FTu2O.2* (Optica Publishing Group, 2021), p. FTu2O.2.
14. D. Strickland and G. Mourou, "Compression of amplified chirped optical pulses," Optics Communications **56**(3), 219–221 (1985).

15. P. Maine, D. Strickland, P. Bado, M. Pessot, and G. Mourou, "Generation of ultrahigh peak power pulses by chirped pulse amplification," IEEE Journal of Quantum Electronics **24**(2), 398–403 (1988).
16. A. Sullivan, H. Hamster, H. C. Kapteyn, S. Gordon, W. White, H. Nathel, R. J. Blair, and R. W. Falcone, "Multiterawatt, 100-fs laser," Opt. Lett., OL **16**(18), 1406–1408 (1991).
17. S. Backus, J. Peatross, C. P. Huang, M. M. Murnane, and H. C. Kapteyn, "Ti:sapphire amplifier producing millijoule-level, 21-fs pulses at 1 kHz," Opt. Lett., OL **20**(19), 2000–2002 (1995).
18. H. Wang, S. Backus, Z. Chang, R. Wagner, K. Kim, X. Wang, D. Umstadter, T. Lei, M. Murnane, and H. Kapteyn, "Generation of 10-W average-power, 40-TW peak-power, 24-fs pulses from a Ti:sapphire amplifier system," J. Opt. Soc. Am. B, JOSAB **16**(10), 1790–1794 (1999).
19. J. Limpert, F. Roeser, T. Schreiber, and A. Tunnermann, "High-power ultrafast fiber laser systems," Selected Topics in Quantum Electronics, IEEE Journal of **12**, 233–244 (2006).
20. B. R. Galloway, D. Popmintchev, E. Pisanty, D. D. Hickstein, M. M. Murnane, H. C. Kapteyn, and T. Popmintchev, "Lorentz drift compensation in high harmonic generation in the soft and hard x-ray regions of the spectrum," Optics express **24**(19), 21818–21832 (2016).
21. M. Wu, S. Ghimire, D. A. Reis, K. J. Schafer, and M. B. Gaarde, "High-harmonic generation from Bloch electrons in solids," Phys. Rev. A **91**(4), 043839 (2015).
22. S. Ghimire, A. D. DiChiara, E. Sistrunk, P. Agostini, L. F. DiMauro, and D. A. Reis, "Observation of high-order harmonic generation in a bulk crystal," Nature Phys **7**(2), 138–141 (2011).
23. G. H. C. New and J. F. Ward, "Optical Third-Harmonic Generation in Gases," Phys. Rev. Lett. **19**(10), 556–559 (1967).
24. M. Hennes, B. Rösner, V. Chardonnet, G. S. Chiuzbaian, R. Delaunay, F. Döring, V. A. Guzenko, M. Hehn, R. Jarrier, A. Kleibert, M. Lebugle, J. Lüning, G. Malinowski, A. Merhe, D. Naumenko, I. P. Nikolov, I. Lopez-Quintas, E. Pedersoli, T. Savchenko, B. Watts, M. Zangrando, C. David, F. Capotondi, B. Vodungbo, and E. Jal, "Time-Resolved XUV Absorption Spectroscopy and Magnetic Circular Dichroism at the Ni M2,3-Edges," Applied Sciences **11**(1), 325 (2021).
25. M. Heber, N. Wind, D. Kutnyakhov, F. Pressacco, T. Arion, F. Roth, W. Eberhardt, and K. Rossnagel, "Multispectral time-resolved energy–momentum microscopy using high-harmonic extreme ultraviolet radiation," Review of Scientific Instruments **93**(8), 083905 (2022).
26. A. Rouzée, A. G. Harvey, F. Kelkensberg, D. Brambila, W. K. Siu, G. Gademann, O. Smirnova, and M. J. J. Vrakking, "Imaging the electronic structure of valence orbitals in the XUV ionization of aligned molecules," J. Phys. B: At. Mol. Opt. Phys. **47**(12), 124017 (2014).
27. I. I. of A. Research, "High-Resolution Extreme Ultraviolet Microscopy. Imaging of Artificial and Biological Specimen with Laser-Driven Ultrafast XUV Sources," Anticancer Research **35**(3), 1830–1831 (2015).
28. C. M. Heyl, C. L. Arnold, A. Couairon, and A. L'Huillier, "Introduction to macroscopic power scaling principles for high-order harmonic generation," J. Phys. B: At. Mol. Opt. Phys. **50**(1), 013001 (2016).
29. H. Coudert-Alteirac, H. Dacasa, F. Campi, E. Kueny, B. Farkas, F. Brunner, S. Maclot, B. Manschwetus, H. Wikmark, J. Lahl, L. Rading, J. Peschel, B. Major, K. Varjú, G. Dovillaire, P. Zeitoun, P. Johnsson, A. L'Huillier, and P. Rudawski, "Micro-Focusing of Broadband High-Order Harmonic Radiation by a Double Toroidal Mirror," Applied Sciences **7**(11), 1159 (2017).
30. S. Kühn, M. Dumergue, S. Kahaly, S. Mondal, M. Füle, T. Csizmadia, B. Farkas, B. Major, Z. Várallyay, E. Cormier, M. Kalashnikov, F. Calegari, M. Devetta, F. Frassetto, E. Månsson, L.

Poletto, S. Stagira, C. Vozzi, M. Nisoli, P. Rudawski, S. Maclot, F. Campi, H. Wikmark, C. L. Arnold, C. M. Heyl, P. Johnsson, A. L'Huillier, R. Lopez-Martens, S. Haessler, M. Bocoum, F. Boehle, A. Vernier, G. Iaquaniello, E. Skantzakis, N. Papadakis, C. Kalpouzos, P. Tzallas, F. Lépine, D. Charalambidis, K. Varjú, K. Osvay, and G. Sansone, "The ELI-ALPS facility: the next generation of attosecond sources," J. Phys. B: At. Mol. Opt. Phys. **50**(13), 132002 (2017).

31. C. Kleine, M. Ekimova, G. Goldsztejn, S. Raabe, C. Strüber, J. Ludwig, S. Yarlagadda, S. Eisebitt, M. J. J. Vrakking, T. Elsaesser, E. T. J. Nibbering, and A. Rouzée, "Soft X-ray Absorption Spectroscopy of Aqueous Solutions Using a Table-Top Femtosecond Soft X-ray Source," J. Phys. Chem. Lett. **10**(1), 52–58 (2019).
32. B. Shan, A. Cavalieri, and Z. Chang, "Tunable high harmonic generation with an optical parametric amplifier," Appl Phys B **74**(1), s23–s26 (2002).
33. J. Boullet, Y. Zaouter, J. Limpert, S. Petit, Y. Mairesse, B. Fabre, J. Higuet, E. Mével, E. Constant, and E. Cormier, "High-order harmonic generation at a megahertz-level repetition rate directly driven by an ytterbium-doped-fiber chirped-pulse amplification system," Opt. Lett., OL **34**(9), 1489–1491 (2009).
34. S. Hädrich, A. Klenke, J. Rothhardt, M. Krebs, A. Hoffmann, O. Pronin, V. Pervak, J. Limpert, and A. Tünnermann, "High photon flux table-top coherent extreme-ultraviolet source," Nature Photon **8**(10), 779–783 (2014).
35. R. Weissenbilder, S. Carlström, L. Rego, C. Guo, C. M. Heyl, P. Smorenburg, E. Constant, C. L. Arnold, and A. L'Huillier, "How to optimize high-order harmonic generation in gases," Nat Rev Phys **4**(11), 713–722 (2022).
36. B. Sheehy, J. D. D. Martin, L. F. DiMauro, P. Agostini, K. J. Schafer, M. B. Gaarde, and K. C. Kulander, "High Harmonic Generation at Long Wavelengths," Phys. Rev. Lett. **83**(25), 5270–5273 (1999).
37. T. Popmintchev, M.-C. Chen, D. Popmintchev, P. Arpin, S. Brown, S. Ališauskas, G. Andriukaitis, T. Balčiunas, O. D. Mücke, A. Pugzlys, A. Baltuška, B. Shim, S. E. Schrauth, A. Gaeta, C. Hernández-García, L. Plaja, A. Becker, A. Jaron-Becker, M. M. Murnane, and H. C. Kapteyn, "Bright Coherent Ultrahigh Harmonics in the keV X-ray Regime from Mid-Infrared Femtosecond Lasers," Science **336**(6086), 1287–1291 (2012).
38. H. Zhang, T. Pincelli, C. Jozwiak, T. Kondo, R. Ernstorfer, T. Sato, and S. Zhou, "Angle-resolved photoemission spectroscopy," Nat Rev Methods Primers **2**(1), 1–22 (2022).
39. M. Puppin, Y. Deng, C. W. Nicholson, J. Feldl, N. B. M. Schröter, H. Vita, P. S. Kirchmann, C. Monney, L. Rettig, M. Wolf, and R. Ernstorfer, "Time- and angle-resolved photoemission spectroscopy of solids in the extreme ultraviolet at 500 kHz repetition rate," Review of Scientific Instruments **90**(2), 023104 (2019).
40. P. F. Moulton, "Tunable solid-state lasers," Proceedings of the IEEE **80**(3), 348–364 (1992).
41. A. Giesen, H. Hügel, A. Voss, K. Wittig, U. Brauch, and H. Opower, "Scalable concept for diode-pumped high-power solid-state lasers," Appl. Phys. B **58**(5), 365–372 (1994).
42. A. Buettner, U. Buenting, D. Wandt, J. Neumann, and D. Kracht, "Ultrafast double-slab regenerative amplifier with combined gain spectra and intracavity dispersion compensation," Opt. Express, OE **18**(21), 21973–21980 (2010).
43. R. Jung, J. Tümmler, and I. Will, "Regenerative thin-disk amplifier for 300 mJ pulse energy," Optics Express **24**(2), 883 (2016).

44. S. Poole, D. Payne, R. Mears, M. Fermann, and R. Laming, "Fabrication and characterization of low-loss optical fibers containing rare-earth ions," Journal of Lightwave Technology **4**(7), 870–876 (1986).
45. Y. H. Lim, G. Tan, and S.-L. Chua, "Effective Single-mode Fibers with Large Mode Areas Through Intermodal-coupling," Procedia Engineering **140**, 49–56 (2016).
46. L. Goldberg, J. P. Koplow, and D. A. V. Kliner, "Highly efficient 4-W Yb-doped fiber amplifier pumped by a broad-stripe laser diode," Opt. Lett., OL **24**(10), 673–675 (1999).
47. R. Paschotta, J. Nilsson, A. C. Tropper, and D. C. Hanna, "Ytterbium-doped fiber amplifiers," IEEE Journal of Quantum Electronics **33**(7), 1049–1056 (1997).
48. E. Snitzer, H. Po, F. Hakimi, R. Tumminelli, and B. C. McCollum, "DOUBLE CLAD, OFFSET CORE Nd FIBER LASER," in *Optical Fiber Sensors (1988), Paper PD5* (Optica Publishing Group, 1988), p. PD5.
49. B. Yang, P. Wang, H. Zhang, X. Xi, C. Shi, X. Wang, and X. Xu, "6 kW single mode monolithic fiber laser enabled by effective mitigation of the transverse mode instability," Opt. Express, OE **29**(17), 26366–26374 (2021).
50. R. Selvas, I. Torres-Gomez, A. Martinez-Rios, J. A. Alvarez-Chavez, D. A. May-Arrioja, P. LiKamWa, A. Mehta, and E. G. Johnson, "Wavelength tuning of fiber lasers using multimode interference effects," Opt. Express, OE **13**(23), 9439–9445 (2005).
51. K. K. Chen, J. H. V. Price, S. Alam, J. R. Hayes, D. Lin, A. Malinowski, and D. J. Richardson, "Polarisation maintaining 100W Yb-fiber MOPA producing μJ pulses tunable in duration from 1 to 21 ps," Opt. Express, OE **18**(14), 14385–14394 (2010).
52. N. Yu, M. Cavillon, C. Kucera, T. Hawkins, J. Ballato, and P. Dragic, "Low Quantum Defect Fiber Lasers via Yb-Doped Multicomponent Fluorosilicate Optical Fiber," in *Conference on Lasers and Electro-Optics (2018), Paper STu3K.6* (Optica Publishing Group, 2018), p. STu3K.6.
53. C. Kong, C. Pilger, H. Hachmeister, X. Wei, T. H. Cheung, C. S. W. Lai, T. Huser, K. K. Tsia, and K. K. Y. Wong, "Compact fs ytterbium fiber laser at 1010 nm for biomedical applications," Biomed. Opt. Express, BOE **8**(11), 4921–4932 (2017).
54. G. Eckhardt, D. P. Bortfeld, and M. Geller, "STIMULATED EMISSION OF STOKES AND ANTI-STOKES RAMAN LINES FROM DIAMOND, CALCITE, AND α-SULFUR SINGLE CRYSTALS," Appl. Phys. Lett. **3**(8), 137–138 (1963).
55. R. G. Smith, "Optical Power Handling Capacity of Low Loss Optical Fibers as Determined by Stimulated Raman and Brillouin Scattering," Appl. Opt., AO **11**(11), 2489–2494 (1972).
56. G. P. Agrawal, "Nonlinear Fiber Optics," in *Nonlinear Science at the Dawn of the 21st Century*, P. L. Christiansen, M. P. Sørensen, and A. C. Scott, eds., Lecture Notes in Physics (Springer, 2000), pp. 195–211.
57. R. R. Alfano, *The Supercontinuum Laser Source / Edited by Robert R. Alfano.*, 1st ed. 1989. (Springer-Verlag, 1989).
58. D. Gloge, "Weakly Guiding Fibers," Appl. Opt., AO **10**(10), 2252–2258 (1971).
59. J. P. Koplow, D. A. V. Kliner, and L. Goldberg, "Single-mode operation of a coiled multimode fiber amplifier," Opt. Lett., OL **25**(7), 442–444 (2000).
60. P. Russell, "Photonic Crystal Fibers," Science **299**(5605), 358 (2003).
61. J. Limpert, "Large-pitch fibers: Pushing very large mode areas to highest powers," in *2012 International Conference on Fiber Optics and Photonics (PHOTONICS)* (2012), pp. 1–2.

62. W. J. Wadsworth, R. M. Percival, G. Bouwmans, J. C. Knight, and P. S. J. Russell, "High power air-clad photonic crystal fibre laser," Opt. Express, OE **11**(1), 48–53 (2003).
63. J. Limpert, T. Schreiber, S. Nolte, H. Zellmer, A. Tünnermann, R. Iliew, F. Lederer, J. Broeng, G. Vienne, A. Petersson, and C. Jakobsen, "High-power air-clad large-mode-area photonic crystal fiber laser," Opt. Express, OE **11**(7), 818–823 (2003).
64. J. Limpert, A. Liem, M. Reich, T. Schreiber, S. Nolte, H. Zellmer, A. Tünnermann, J. Broeng, A. Petersson, and C. Jakobsen, "Low-nonlinearity single-transverse-mode ytterbium-doped photonic crystal fiber amplifier," Opt. Express, OE **12**(7), 1313–1319 (2004).
65. J. Limpert, N. Deguil-Robin, I. Manek-Hönninger, F. Salin, F. Röser, A. Liem, T. Schreiber, S. Nolte, H. Zellmer, A. Tünnermann, J. Broeng, A. Petersson, and C. Jakobsen, "High-power rod-type photonic crystal fiber laser," Opt. Express, OE **13**(4), 1055–1058 (2005).
66. J. Limpert, F. Stutzki, F. Jansen, H.-J. Otto, T. Eidam, C. Jauregui, and A. Tünnermann, "Yb-doped large-pitch fibres: effective single-mode operation based on higher-order mode delocalisation," Light Sci Appl **1**(4), e8–e8 (2012).
67. J. Limpert, T. Schreiber, A. Liem, S. Nolte, H. Zellmer, T. Peschel, V. Guyenot, and A. Tünnermann, "Thermo-optical properties of air-clad photonic crystal fiber lasers in high power operation," Opt. Express, OE **11**(22), 2982–2990 (2003).
68. K. Tamura and M. Nakazawa, "Pulse compression by nonlinear pulse evolution with reduced optical wave breaking in erbium-doped fiber amplifiers," Opt. Lett., OL **21**(1), 68–70 (1996).
69. D. Anderson, M. Desaix, M. Karlsson, M. Lisak, and M. L. Quiroga-Teixeiro, "Wave-breaking-free pulses in nonlinear-optical fibers," J. Opt. Soc. Am. B, JOSAB **10**(7), 1185–1190 (1993).
70. V. I. Kruglov, A. C. Peacock, J. D. Harvey, and J. M. Dudley, "Self-similar propagation of parabolic pulses in normal-dispersion fiber amplifiers," J. Opt. Soc. Am. B, JOSAB **19**(3), 461–469 (2002).
71. C. Runge, "Ueber die numerische Auflösung von Differentialgleichungen," Math. Ann. **46**(2), 167–178 (1895).
72. J. C. Butcher, "Coefficients for the study of Runge-Kutta integration processes," Journal of the Australian Mathematical Society **3**(2), 185–201 (1963).
73. A. M. Heidt, "Efficient Adaptive Step Size Method for the Simulation of Supercontinuum Generation in Optical Fibers," J. Lightwave Technol., JLT **27**(18), 3984–3991 (2009).
74. J. Hult, "A Fourth-Order Runge–Kutta in the Interaction Picture Method for Simulating Supercontinuum Generation in Optical Fibers," Journal of Lightwave Technology **25**(12), 3770–3775 (2007).
75. R. Lindberg, P. Zeil, M. Malmström, F. Laurell, and V. Pasiskevicius, "Accurate modeling of high-repetition rate ultrashort pulse amplification in optical fibers," Sci Rep **6**(1), 34742 (2016).
76. M. E. Fermann, V. I. Kruglov, B. C. Thomsen, J. M. Dudley, and J. D. Harvey, "Self-Similar Propagation and Amplification of Parabolic Pulses in Optical Fibers," Phys. Rev. Lett. **84**(26), 6010–6013 (2000).
77. A. Chong, H. Liu, B. Nie, B. G. Bale, S. Wabnitz, W. H. Renninger, M. Dantus, and F. W. Wise, "Pulse generation without gain-bandwidth limitation in a laser with self-similar evolution," Opt. Express, OE **20**(13), 14213–14220 (2012).

78. D. N. Schimpf, J. Limpert, and A. Tünnermann, "Controlling the influence of SPM in fiber-based chirped-pulse amplification systems by using an actively shaped parabolic spectrum," Opt. Express, OE **15**(25), 16945–16953 (2007).
79. M. Seidel, P. Balla, C. Li, G. Arisholm, L. Winkelmann, I. Hartl, and C. Heyl, "Factor 30 Pulse Compression by Hybrid Multipass Multiplate Spectral Broadening," Ultrafast Science **2022**, 1–10 (2022).
80. N. Singh, E. Ippen, and F. X. Kärtner, "Towards CW modelocked laser on chip – a large mode area and NLI for stretched pulse mode locking," Opt. Express, OE **28**(15), 22562–22579 (2020).
81. M. Edelmann, M. M. Sedigheh, Y. Hua, E. C. Vargas, M. Pergament, and F. X. Kärtner, "Large-mode-area soliton fiber oscillator mode-locked using NPE in an all-PM self-stabilized interferometer," Appl. Opt., AO **62**(7), 1672–1676 (2023).
82. M. E. Fermann, L.-M. Yang, M. L. Stock, and M. J. Andrejco, "Environmentally stable Kerr-type mode-locked erbium fiber laser producing 360-fs pulses," Opt. Lett., OL **19**(1), 43–45 (1994).
83. WaveShaper 1000SP, "Pulse Shaping using the WaveShaper 1000 / SP 1," in (2015).
84. R. W. Boyd, *Nonlinear Optics* (Elsevier, 2003).
85. M. Gross and M. Groß, "Laser Pulse Train Management with an Acousto-optic Modulator," (2012).
86. T. A. Birks and Y. W. Li, "The shape of fiber tapers," Journal of Lightwave Technology **10**(4), 432–438 (1992).
87. C. E. Chryssou, "Theoretical analysis of tapering fused silica optical fibers using a carbon dioxide laser," OE **38**(10), 1645–1649 (1999).
88. J. Schulte, T. Sartorius, J. Weitenberg, A. Vernaleken, and P. Russbueldt, "Nonlinear pulse compression in a multi-pass cell," Opt. Lett., OL **41**(19), 4511–4514 (2016).
89. C. Jocher, T. Eidam, S. Hädrich, J. Limpert, and A. Tünnermann, "Sub 25 fs pulses from solid-core nonlinear compression stage at 250 W of average power," Opt. Lett., OL **37**(21), 4407–4409 (2012).
90. F. Emaury, C. J. Saraceno, B. Debord, D. Ghosh, A. Diebold, F. Gèrôme, T. Südmeyer, F. Benabid, and U. Keller, "Efficient spectral broadening in the 100-W average power regime using gas-filled kagome HC-PCF and pulse compression," Opt. Lett., OL **39**(24), 6843–6846 (2014).
91. S. Hädrich, M. Kienel, M. Müller, A. Klenke, J. Rothhardt, R. Klas, T. Gottschall, T. Eidam, A. Drozdy, P. Jójárt, Z. Várallyay, E. Cormier, K. Osvay, A. Tünnermann, and J. Limpert, "Energetic sub-2-cycle laser with 216 W average power," Opt. Lett., OL **41**(18), 4332–4335 (2016).
92. J. Rothhardt, S. Hädrich, H. Carstens, N. Herrick, S. Demmler, J. Limpert, and A. Tünnermann, "1 MHz repetition rate hollow fiber pulse compression to sub-100-fs duration at 100 W average power," Opt. Lett., OL **36**(23), 4605–4607 (2011).
93. S. Hädrich, M. Kienel, M. Müller, A. Klenke, J. Rothhardt, R. Klas, T. Gottschall, T. Eidam, A. Drozdy, P. Jojart, Z. Várallyay, E. Cormier, K. Osvay, A. Tünnermann, and J. Limpert, "200 W Average Power Energetic Few-cycle Fiber Laser," in *High-Brightness Sources and Light-Driven Interactions (2016), Paper JT3A.1* (Optica Publishing Group, 2016), p. JT3A.1.
94. F. Benabid, J. C. Knight, G. Antonopoulos, and P. S. J. Russell, "Stimulated Raman Scattering in Hydrogen-Filled Hollow-Core Photonic Crystal Fiber," Science **298**(5592), 399–402 (2002).

95. J. C. Travers, W. Chang, J. Nold, N. Y. Joly, and P. S. J. Russell, "Ultrafast nonlinear optics in gas-filled hollow-core photonic crystal fibers [Invited]," J. Opt. Soc. Am. B, JOSAB **28**(12), A11–A26 (2011).
96. T. Balciunas, C. Fourcade-Dutin, G. Fan, T. Witting, A. A. Voronin, A. M. Zheltikov, F. Gerome, G. G. Paulus, A. Baltuska, and F. Benabid, "A strong-field driver in the single-cycle regime based on self-compression in a kagome fibre," Nat Commun **6**(1), 6117 (2015).
97. F. Emaury, C. F. Dutin, C. J. Saraceno, M. Trant, O. H. Heckl, Y. Y. Wang, C. Schriber, F. Gerome, T. Südmeyer, F. Benabid, and U. Keller, "Beam delivery and pulse compression to sub-50 fs of a modelocked thin-disk laser in a gas-filled Kagome-type HC-PCF fiber," Opt. Express, OE **21**(4), 4986–4994 (2013).
98. K. F. Mak, J. C. Travers, N. Y. Joly, A. Abdolvand, and P. S. J. Russell, "Two techniques for temporal pulse compression in gas-filled hollow-core kagomé photonic crystal fiber," Opt. Lett., OL **38**(18), 3592–3595 (2013).
99. K. F. Mak, M. Seidel, O. Pronin, M. H. Frosz, A. Abdolvand, V. Pervak, A. Apolonski, F. Krausz, J. C. Travers, and P. S. J. Russell, "Compressing µJ-level pulses from 250 fs to sub-10 fs at 38-MHz repetition rate using two gas-filled hollow-core photonic crystal fiber stages," Opt. Lett., OL **40**(7), 1238–1241 (2015).
100. C. Rolland and P. B. Corkum, "Compression of high-power optical pulses," J. Opt. Soc. Am. B, JOSAB **5**(3), 641–647 (1988).
101. M. Seidel, G. Arisholm, J. Brons, V. Pervak, and O. Pronin, "All solid-state spectral broadening: an average and peak power scalable method for compression of ultrashort pulses," Opt Express **24**(9), 9412–9428 (2016).
102. anne-laure Calendron, J. Meier, E. Kueny, S. Velten, L. Bocklage, R. Röhlsberger, and F. Kärtner, "Bulk, cascaded pulse compression scheme and its application to spin emitter characterization," Applied Optics **60**, (2021).
103. A. VERNALEKEN, P. RUSSBÜLDT, T. Sartorius, J. SCHULTE, and J. Weitenberg, "Verfahren und anordnung zur spektralen verbreiterung von laserpulsen für die nichtlineare pulskompression," European Union patent EP3143669A1 (March 22, 2017).
104. J. Rothhardt, S. Hädrich, A. Klenke, S. Demmler, A. Hoffmann, T. Gotschall, T. Eidam, M. Krebs, J. Limpert, and A. Tünnermann, "53 W average power few-cycle fiber laser system generating soft x rays up to the water window," Opt. Lett., OL **39**(17), 5224–5227 (2014).
105. M. Hanna, F. Guichard, N. Daher, Q. Bournet, X. Délen, and P. Georges, "Nonlinear Optics in Multipass Cells," Laser & Photonics Reviews **15**(12), 2100220 (2021).
106. C.-H. Lu, Y.-J. Tsou, H.-Y. Chen, B.-H. Chen, Y.-C. Cheng, S.-D. Yang, M.-C. Chen, C.-C. Hsu, and A. H. Kung, "Generation of intense supercontinuum in condensed media," Optica, OPTICA **1**(6), 400–406 (2014).
107. D. Herriott, H. Kogelnik, and R. Kompfner, "Off-Axis Paths in Spherical Mirror Interferometers," Appl. Opt., AO **3**(4), 523–526 (1964).
108. A. M. Kowalevicz, A. Sennaroglu, A. T. Zare, and J. G. Fujimoto, "Design principles of q-preserving multipass-cavity femtosecond lasers," J. Opt. Soc. Am. B, JOSAB **23**(4), 760–770 (2006).
109. P. Russbueldt, T. Mans, J. Weitenberg, H. D. Hoffmann, and R. Poprawe, "Compact diode-pumped 1.1 kW Yb:YAG Innoslab femtosecond amplifier," Opt. Lett., OL **35**(24), 4169–4171 (2010).

110. M. Kaumanns, V. Pervak, D. Kormin, V. Leshchenko, A. Kessel, M. Ueffing, Y. Chen, and T. Nubbemeyer, "Multipass spectral broadening of 18 mJ pulses compressible from 1.3 ps to 41 fs," Opt. Lett., OL **43**(23), 5877–5880 (2018).
111. A.-L. Viotti, M. Seidel, E. Escoto, S. Rajhans, W. P. Leemans, I. Hartl, and C. M. Heyl, "Multi-pass cells for post-compression of ultrashort laser pulses," Optica, OPTICA **9**(2), 197–216 (2022).
112. S. C. Pinault and M. J. Potasek, "Frequency broadening by self-phase modulation in optical fibers," J. Opt. Soc. Am. B, JOSAB **2**(8), 1318–1319 (1985).
113. G. Agrawal, "Chapter 4 - Self-Phase Modulation," in *Nonlinear Fiber Optics (Fifth Edition)*, G. Agrawal, ed., Optics and Photonics (Academic Press, 2013), pp. 87–128.
114. D. R. Herriott and H. J. Schulte, "Folded Optical Delay Lines," Appl. Opt., AO **4**(8), 883–889 (1965).
115. A. E. Siegman, *Lasers* (University Science Books, 1986).
116. M. Hanna, N. Daher, F. Guichard, X. Délen, and P. Georges, "Hybrid pulse propagation model and quasi-phase-matched four-wave mixing in multipass cells," J. Opt. Soc. Am. B, JOSAB **37**(10), 2982–2988 (2020).
117. S. Witte and K. S. E. Eikema, "Ultrafast Optical Parametric Chirped-Pulse Amplification," IEEE Journal of Selected Topics in Quantum Electronics **18**(1), 296–307 (2012).
118. F. Krausz and M. Ivanov, "Attosecond physics," Rev. Mod. Phys. **81**(1), 163–234 (2009).
119. P. Rudawski, C. M. Heyl, F. Brizuela, J. Schwenke, A. Persson, E. Mansten, R. Rakowski, L. Rading, F. Campi, B. Kim, P. Johnsson, and A. L'Huillier, "A high-flux high-order harmonic source," Review of Scientific Instruments **84**(7), 073103 (2013).
120. F. X. Kärtner, F. Ahr, A.-L. Calendron, H. Çankaya, S. Carbajo, G. Chang, G. Cirmi, K. Dörner, U. Dorda, A. Fallahi, A. Hartin, M. Hemmer, R. Hobbs, Y. Hua, W. R. Huang, R. Letrun, N. Matlis, V. Mazalova, O. D. Mücke, E. Nanni, W. Putnam, K. Ravi, F. Reichert, I. Sarrou, X. Wu, A. Yahaghi, H. Ye, L. Zapata, D. Zhang, C. Zhou, R. J. D. Miller, K. K. Berggren, H. Graafsma, A. Meents, R. W. Assmann, H. N. Chapman, and P. Fromme, "AXSIS: Exploring the frontiers in attosecond X-ray science, imaging and spectroscopy," Nuclear Instruments and Methods in Physics Research Section A: Accelerators, Spectrometers, Detectors and Associated Equipment **829**, 24–29 (2016).
121. G. Polónyi, B. Monoszlai, G. Gäumann, E. J. Rohwer, G. Andriukaitis, T. Balciunas, A. Pugzlys, A. Baltuska, T. Feurer, J. Hebling, and J. A. Fülöp, "High-energy terahertz pulses from semiconductors pumped beyond the three-photon absorption edge," Opt. Express, OE **24**(21), 23872–23882 (2016).
122. M. Müller, C. Aleshire, A. Klenke, E. Haddad, F. Légaré, A. Tünnermann, and J. Limpert, "10.4 kW coherently combined ultrafast fiber laser," Opt. Lett., OL **45**(11), 3083–3086 (2020).
123. H. Cankaya, U. Demirbas, Y. Hua, M. Hemmer, L. E. Zapata, M. Pergament, and F. X. Kaertner, "190-mJ cryogenically-cooled Yb:YLF amplifier system at 1019.7 nm," OSA Continuum, OSAC **2**(12), 3547–3553 (2019).
124. K.-H. Hong, C.-J. Lai, A. Siddiqui, and F. X. Kärtner, "130-W picosecond green laser based on a frequency-doubled hybrid cryogenic Yb:YAG amplifier," Opt. Express, OE **17**(19), 16911–16919 (2009).

125. L. E. Zapata, F. Reichert, M. Hemmer, and F. X. Kärtner, "250 W average power, 100 kHz repetition rate cryogenic Yb:YAG amplifier for OPCPA pumping," Opt. Lett., OL **41**(3), 492–495 (2016).
126. A. Giesen and J. Speiser, "Fifteen Years of Work on Thin-Disk Lasers: Results and Scaling Laws," IEEE Journal of Selected Topics in Quantum Electronics **13**(3), 598–609 (2007).
127. J. Brons, V. Pervak, D. Bauer, D. Sutter, O. Pronin, and F. Krausz, "Powerful 100-fs-scale Kerr-lens mode-locked thin-disk oscillator," Opt. Lett., OL **41**(15), 3567–3570 (2016).
128. T. Nubbemeyer, M. Kaumanns, M. Ueffing, M. Gorjan, A. Alismail, H. Fattahi, J. Brons, O. Pronin, H. G. Barros, Z. Major, T. Metzger, D. Sutter, and F. Krausz, "1 kW, 200 mJ picosecond thin-disk laser system," Opt. Lett., OL **42**(7), 1381–1384 (2017).
129. X. Délen, Y. Zaouter, I. Martial, N. Aubry, J. Didierjean, C. Hönninger, E. Mottay, F. Balembois, and P. Georges, "Yb:YAG single crystal fiber power amplifier for femtosecond sources," Opt. Lett., OL **38**(2), 109–111 (2013).
130. U. Demirbas, H. Cankaya, Y. Hua, J. Thesinga, M. Pergament, and F. X. Kärtner, "20-mJ, sub-ps pulses at up to 70 W average power from a cryogenic Yb:YLF regenerative amplifier," Opt. Express, OE **28**(2), 2466–2479 (2020).
131. D. C. Brown, "The promise of cryogenic solid-state lasers," IEEE Journal of Selected Topics in Quantum Electronics **11**(3), 587–599 (2005).
132. T. Y. Fan, D. J. Ripin, R. L. Aggarwal, J. R. Ochoa, B. Chann, M. Tilleman, and J. Spitzberg, "Cryogenic $Yb^{3+\$}$-Doped Solid-State Lasers," IEEE Journal of Selected Topics in Quantum Electronics **13**(3), 448–459 (2007).
133. R. L. Aggarwal, D. J. Ripin, J. R. Ochoa, and T. Y. Fan, "Measurement of thermo-optic properties of Y3Al5O12, Lu3Al5O12, YAlO3, LiYF4, LiLuF4, BaY2F8, KGd(WO4)2, and KY(WO4)2 laser crystals in the 80–300K temperature range," Journal of Applied Physics **98**(10), 103514 (2005).
134. L. E. Zapata, H. Lin, A.-L. Calendron, H. Cankaya, M. Hemmer, F. Reichert, W. R. Huang, E. Granados, K.-H. Hong, and F. X. Kärtner, "Cryogenic Yb:YAG composite-thin-disk for high energy and average power amplifiers," Opt. Lett., OL **40**(11), 2610–2613 (2015).
135. U. Demirbas, H. Cankaya, J. Thesinga, F. X. Kärtner, and M. Pergament, "Efficient, diode-pumped, high-power (>300W) cryogenic Yb:YLF laser with broad-tunability (995-1020.5 nm): investigation of E//a-axis for lasing," Opt. Express, OE **27**(25), 36562–36579 (2019).
136. J. Kawanaka, K. Yamakawa, H. Nishioka, and K. Ueda, "Improved high-field laser characteristics of a diode-pumped Yb:$LiYF_4$ crystal at low temperature," Opt. Express, OE **10**(10), 455–460 (2002).
137. D. E. Miller, J. R. Ochoa, and T. Y. Fan, "Cryogenically cooled, 149 W, Q-switched, Yb:$LiYF_4$ laser," Opt. Lett., OL **38**(20), 4260–4261 (2013).
138. A. Bensalah, Y. Guyot, M. Ito, A. Brenier, H. Sato, T. Fukuda, and G. Boulon, "Growth of Yb3+-doped YLiF4 laser crystal by the Czochralski method. Attempt of Yb3+ energy level assignment and estimation of the laser potentiality," Optical Materials **26**(4), 375–383 (2004).
139. A. Sugiyama, M. Katsurayama, Y. Anzai, and T. Tsuboi, "Spectroscopic properties of Yb doped YLF grown by a vertical Bridgman method," Journal of Alloys and Compounds **408**–**412**, 780–783 (2006).

140. M. Pergament, M. Kellert, U. Demirbas, J. Thesinga, S. Reuter, Y. Hua, M. Kilinc, and F. X. Kärtner, "100mJ, 100W Cryogenically Cooled Yb:YLF Laser," in *Conference on Lasers and Electro-Optics* (Optica Publishing Group, 2022), p. STu4N.5.
141. D. C. Brown, S. Tornegård, and J. Kolis, "Cryogenic nanosecond and picosecond high average and peak power (HAPP) pump lasers for ultrafast applications," High Power Laser Science and Engineering **4**, e15 (2016).
142. A. Chong, W. H. Renninger, and F. W. Wise, "All-normal-dispersion femtosecond fiber laser with pulse energy above 20nJ," Opt. Lett., OL **32**(16), 2408–2410 (2007).
143. Y. Hua, W. Liu, M. Hemmer, L. E. Zapata, G. Zhou, D. N. Schimpf, T. Eidam, J. Limpert, A. Tünnermann, F. X. Kärtner, and G. Chang, "87-W 1018-nm Yb-fiber ultrafast seeding source for cryogenic Yb: yttrium lithium fluoride amplifier," Opt. Lett. **43**(8), 1686 (2018).
144. B. Morasse, É. Gagnon, J. Arsenault-Roy, and J.-P. de Sandro, "High Peak Power Single-mode Amplification Using Highly Doped Double Cladding Ytterbium Phosphosilicate Fiber," in *Workshop on Specialty Optical Fibers and Their Applications* (OSA, 2013), p. F2.19.
145. P. Balla, H. Tünnermann, S. Salman, M. Fan, S. Alisauskas, I. Hartl, and C. Heyl, "Ultrafast serrodyne optical frequency translator," Nature Photonics **17**, 1–6 (2022).